THE MID-LATITUDE IONOSPHERE UNDER QUIET GEOMAGNETIC CONDITIONS: PROPAGATION ANALYSIS OF SUPERDARN RADAR OBSERVATIONS FOR LARGE IONOSPHERIC PERTURBATIONS

Sébastien de Larquier

Dissertation submitted to the faculty of Virginia Tech
in partial fulfilment of the requirements for the degree of

DOCTOR OF PHILOSOPHY

in

ELECTRICAL ENGINEERING

J. Michael Ruohoniemi, Co-Chair
Joseph B.H. Baker, Co-Chair
Gregory D. Earle
Wayne A. Scales
Timothy Pratt
Werner A. Kohler

November 22, 2013
Blacksburg, VA

keywords: Ionosphere, SuperDARN, Plasma Instability, HF Propagation

Abstract

The Earth's ionosphere is a dynamic environment strongly coupled to the neutral atmosphere, magnetosphere and solar activity. In the context of this research, we restrict our interest to the mid-latitude (a.k.a., sub-auroral) ionosphere during quiet geomagnetic conditions. The Super Dual Auroral Radar Network (SuperDARN) is composed of more than 30 low-power High Frequency (HF, from 8-18 MHz) Doppler radars covering the sub-auroral, auroral and polar ionosphere in both hemispheres. SuperDARN radars rely on the dispersive properties of the ionosphere at HF to monitor dynamic features of the ionosphere. Though originally designed to follow auroral expansion during active periods, mid-latitude SuperDARN radars have observed ground and ionospheric scatter revealing several interesting features of the mid-latitude ionosphere during periods of moderate to low geomagnetic activity. The past 7 years' expansion of SuperDARN to mid-latitudes, combined with the recent extended solar minimum, provides large-scale continuous views of the sub-auroral ionosphere for the first time. We have leveraged these circumstances to study prominent and recurring features of the mid-latitude ionosphere under quiet geomagnetic conditions.

First, we seek to establish a better model of HF propagation effects on SuperDARN observations. To do so, we developed a ray-tracing model coupled with the International Reference Ionosphere (IRI). This model is tested against another well established ray-tracing model, then optimized to be compared to SuperDARN observations (Chapter 2).

The first prominent ionospheric feature studied is an anomaly in the standard ionospheric model of photo-ionization and recombination. This type of event provides an ideal candidate for testing the ray-tracing model and analyzing propagation effects in SuperDARN observations. The anomaly was first observed in ground backscatter occurring around sunset for the Blackstone, VA SuperDARN radar. We established that it is related to an unexpected enhancement in electron densities that leads to increased refraction of the HF signals. Using the ray-tracing, IRI model, and measurements from the Millstone Hill Incoherent Scatter Radar (ISR), we showed that this enhancement is part of a global phenomenon in the Northern Hemisphere, and is possibly related to the Southern Hemisphere's Weddell Sea Anomaly. We also tested a potential mechanism involving thermospheric winds and geomagnetic field configuration which showed promising results and will require further modeling to confirm (Chapter 3).

The second ionospheric feature was a type of decameter-scale irregularity associated with very low drift velocities. Previous work had established that these irregularities occur throughout the year, during nighttime, and equatorward of both the auroral regions and the plasmapause boundary. An initial analysis from *Greenwald et al.* [2006] suggested that the Temperature Gradient Instability (TGI) was responsible for the growth of such irregularities. We first used our ray-tracing model to distinguish between HF propagation effects and irregularity occurrence in SuperDARN observations. This revealed the irregularities to be widespread within the mid-

latitude ionosphere and located in the bottom-side F-region (Chapter 4). A second study using measurements from the Millstone Hill ISR revealed that TGI driven growth was possible but only in the top-side F-region ionosphere. We found that initial growth may occur primarily at larger wavelengths, with subsequent cascade to decameter-scale with coupling throughout the F-region (Chapter 5).

In summary, the research conducted during this PhD program has established a robust method to analyze quiet-time SuperDARN observations. It also furthered our physical understanding of some prominent features of the mid-latitude ionosphere. It leaves behind a flexible ray-tracing model, multiple online tools to browse SuperDARN data, and a thorough and growing Space Science API providing access to multiple datasets, models and visualization tools.

Acknowledgments

My transition to Virginia Tech for my PhD was the result of incredible luck. After barely completing the application process, I received an email from Mike who had somehow seen my application. He remembered my name from the previous CEDAR meeting where I had won first place at the student poster competition. He proceeded to encourage me to finish my application and invited me for a visit at Virginia Tech. I clearly recall a lunch at Boudreaux's and an evening bbq at Mike's, all accompanied by proper refreshments! I remember feeling so welcomed by Mike, Jo and Lasse that my decision to move to VT was made on the same day (though I had to wait a few days until defending my M.Sc. to share it). This was clearly one of my better decisions, as the past three and a half years have been full of great experiences, academic or otherwise!

I have learned so much during these three and a half years that it is difficult to keep track of all of it. Obviously, coming in with almost no space physics knowledge, I picked up quite a lot on the topic (and still am, until the very hour before the last word of this dissertation). I still scratch my head when thinking of the coupling between each element of the system that I studied so closely. But while this knowledge is certainly the most complex and literally wonderful acquisition of my PhD, I was thrown into another very valuable set of new skills. Because SuperDARN serves as a data provider, and because Mike and Jo always encouraged me and all the other students to pursue our technological dreams, I have learned what it means to serve a community, along with a wide range of coding skills. I know how very fortunate I am to have worked with two of the very few academics who see value in such pursuit, and I will continue to advocate for more efforts in this direction, even as I leave the field for a career in data science.

Finally, I am very grateful to Dr. Wayne Scales, Dr. Greg Earle, Dr. Werner Kohler and Dr. Tim Pratt for their patience and advice in reviewing this dissertation and its defense.

Every word and every idea inside or behind this dissertation exists only thanks to the unbounded and awesome influence of the following people: Mike, Jo, Phil, AJ, Bharat, Evan, Nathaniel, Lasse, Kevin, Pasha and of course my family.

Sebastien de Larquier,
Blacksburg, VA
Fall 2013

This research was supported by the National Science Foundation under grant AGS-0946900 to Virginia Tech.

Table of Contents

List of Figures

List of Tables

List of Symbols and Acronyms

SYMBOLS

$\mathbf{B}$	Magnetic field vector
h, h_v	Altitude and virtual altitude (km)
μ	Refractive index
$\mathbf{k}$	Wave vector
α	Complement to the aspect angle, i.e. the angle between the signal $\mathbf{k}$ and the geomagnetic field $\mathbf{B}$ ($^\circ$)
N_e, T_e	Electron density (m^{-3}) and temperature (K)
NmF_2, hmF_2	F-region peak electron density (m^{-3}) and peak altitude (km)

ACRONYMS

AACGM	Altitude Adjusted Corrected Geomagnetic Coordinates
GDI	Gradient Drift Instability
HF	High Frequency
HWM	Horizontal Wind Model
IGRF	International Geomagnetic Reference Field
IRI	International Reference Ionosphere
ISR	Incoherent Scatter Radar
SAIS	Sub-Auroral Ionospheric Scatter
SEA	Summer Evening Anomaly
SuperDARN	Super Dual Auroral Radar Network
TGI	Temperature Gradient Instability
WSA	Weddell Sea Anomaly

Chapter 1

Introduction

1.1 Motivations and context

1.1.1 The mid-latitude ionosphere

1.1.1.1 Structure and formation

The Earth's atmosphere is typically divided into vertical regions based on its temperature profile [e.g., *Kelley*, 2009]. Its topmost layer is marked by a significant increase in temperature with altitude due to the influence of solar radiation. This same factor causes neutral gas in the upper atmosphere to be weakly ionized to the degree of a cold plasma, thus forming the ionosphere, which extends from 80 to about 1000 km. Since different types of solar radiations penetrate to different altitudes, the ionosphere is structured in layers (from low to high: D, E, and F) of different plasma densities, peaking in the F-region, between 250 and 350 km. This structure is illustrated in Figure 1.1 for a typical day.

The Earth's near-dipolar geomagnetic field also contributes to focusing external and internal forcing of the ionosphere to different latitudes, thus structuring the ionosphere into low-latitude (equatorial), mid-latitude (sub-auroral), and high-latitude (auroral) regions. While the equatorial region is defined by its proximity to the geomagnetic equator and the high-latitude regions by energetic particle precipitation, the mid-latitude sector is usually considered a buffer between the two aforementioned regions.

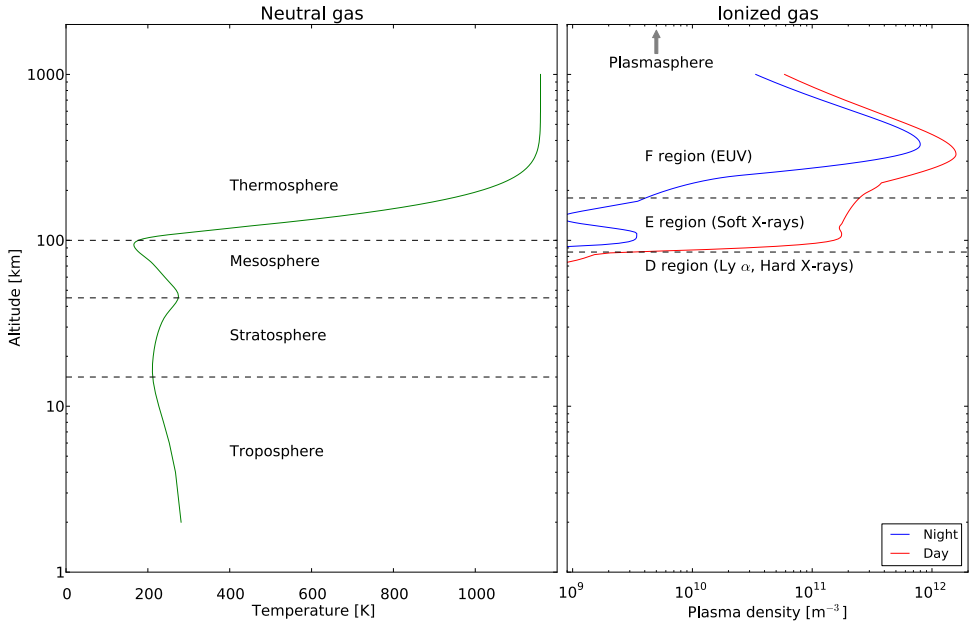

Figure 1.1. Neutral atmosphere and ionosphere vertical profiles. **(left)** Typical neutral temperature variations with altitude generated from the MSIS model. **(right)** Typical day-time (red) and night-time (blue) Typical plasma density variations with altitude generated from the IRI model, and penetration altitude of various types of solar radiation. In both panels, different altitude regions are identified by their common name.

1.1.1.2 Variability

The boundaries between these regions vary with the changing structure of the geomagnetic field, which is primarily controlled by its interaction with the Sun's Interplanetary Magnetic Field (IMF) as carried Earthward by the plasma of the solar wind. The intensity of the interaction between the IMF and Earth's geomagnetic field is typically called geomagnetic activity and measured is through a variety of indices based on geomagnetic field perturbations (e.g., K, A, Dst).

In the context of this research, we restrict our interest to the mid-latitude (a.k.a., sub-auroral) ionosphere during quiet geomagnetic conditions. This subset of ionospheric conditions is mainly controlled by plasma/neutral interactions (e.g., winds, waves) [e.g., *Fukao and Kelley*, 1991], electric field effects [e.g., *Kelley*, 2009, chap. 5] and solar radiation.

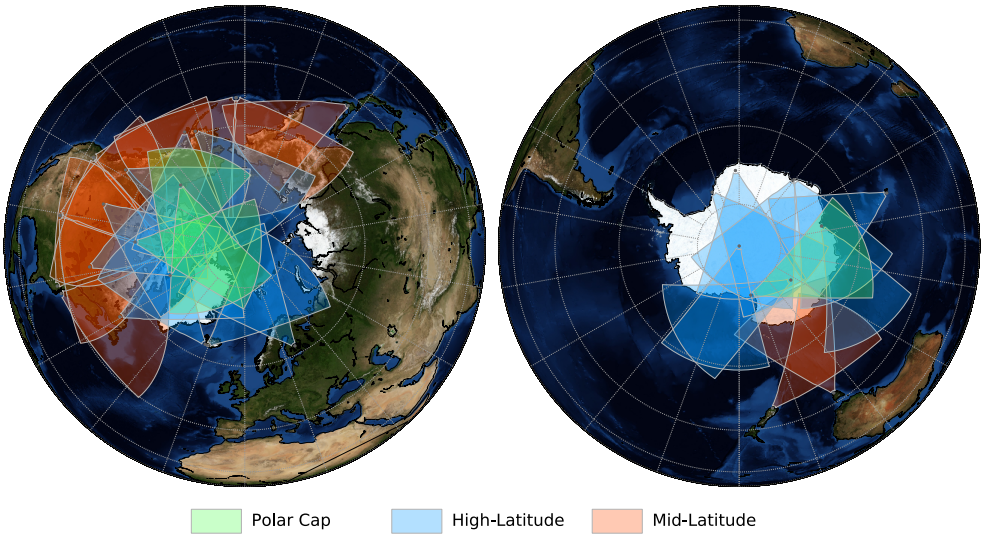

Figure 1.2. SuperDARN field-of-views in both hemispheres as of September 2013. In the context of this dissertation, we wil focus on sub-auroral (red) radars in the Northern hemisphere.

1.1.2 Monitoring the ionosphere with SuperDARN radars

1.1.2.1 An introduction to SuperDARN

Multiple ground and space based instruments are available to monitor the ionosphere, whether in-situ or through remote sensing, based on a wide range of passive and active optical or electromagnetic systems [e.g., *Schunk and Nagy*, 2009, chap. 14].

The Super Dual Auroral Radar Network (SuperDARN) is composed, as of September 2013, of more than 30 low-power High Frequency (HF, from 8-18 MHz) Doppler radars covering sub-auroral, auroral and polar ionosphere in both hemispheres [e.g., *Chisham et al.*, 2007]. SuperDARN radars offer the significant advantage of operating continuously over large regions of the ionosphere, a rare characteristic of ionospheric monitoring systems. Figure 1.2 shows the spatial coverage of SuperDARN in both hemisphere.

SuperDARN radars rely on the dispersive properties of the ionosphere at HF to monitor dynamic features of the ionosphere [e.g., *Greenwald et al.*, 1985]. As an electromagnetic wave propagates through the ionosphere, changes in electron density result in refraction of the wave. The refractive index is expressed by the

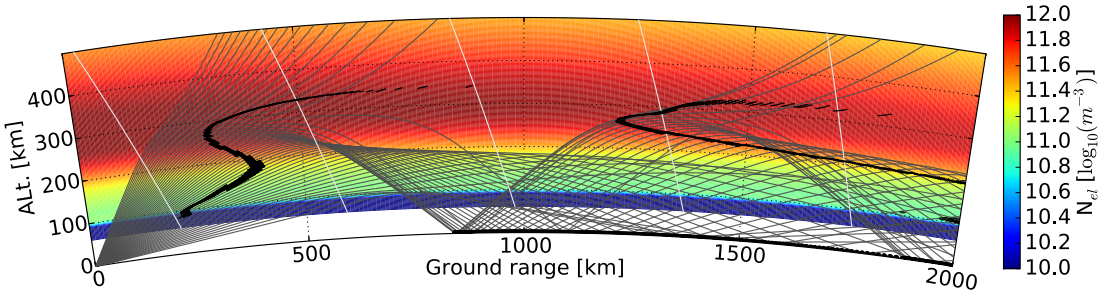

Figure 1.3. Typical day-time HF propagation and SuperDARN backscatter categories. The black shading above ground level indicates regions of good aspect conditions, i.e. where the rays are within 1° of orthogonality with the background geomagnetic field. These high altitude regions indicate where SuperDARN could observe ionospheric scatter. The black shading at ground level marks where rays reach the ground. These ground reaching rays indicate where SuperDARN could observe ground backscatter. Ionospheric electron densities from the International Reference Ionosphere (IRI) are plotted in the background, as well as geomagnetic field lines (white curves).

Appleton formula [e.g., *Davies*, 1990], and in the case of the F region ionosphere at HF, is mainly controlled by electron density. Refraction of HF signals in the ionosphere is used by SuperDARN to observe two types of backscatter:

- Ground scatter: HF signals are refracted to the point of turning back towards the ground, where based on terrain (geometry, composition), part of the signal is reflected back to the radar [e.g., *Ponomarenko et al.*, 2010]. Perturbations in ground scatter signature are usually caused by waves (e.g., atmospheric gravity waves, tides), changes in electron density, or vertical motions of the ionosphere due to neutral winds or electric fields [e.g., *Bristow et al.*, 1996].

- Ionospheric scatter: HF signals experience coherent backscatter from decameter-scale field-aligned density irregularities when the angle between the propagation direction and the geomagnetic field – the aspect angle – is close to 90°. Irregularities of diverse scale sizes develop in the ionosphere due to plasma instabilities [e.g., *Tsunoda*, 1988]. The occurrence of ionospheric scatter varies strongly with geomagnetic activity [e.g. *Chisham et al.*, 2007].

.

Figure 1.3 illustrated both type of backscatter. Ionospheric scatter is identified with black shading in the ionosphere along the signal's path. Ground scatter is simply marked where the signa reaches the ground. One can see how refraction

of HF signals both enables SuperDARN observations, and complicate their interpretation. Changes in refraction clearly results in the ground scatter appearing closer or further away from the radar. However, because the radar measures time-of-flight to the target along the signal's path, finding the location of the scatter requires the elevation of the returned signal, and a good understanding of HF propagation. Similarly, as refraction changes, orthogonality with the geomagnetic field is achieved at different altitudes and distances from the radar, both parameters being functions of time-of-flight, refraction, and the occurrence of field-aligned irregularities. Estimating refraction is a difficult endeavor at best, even more so at high-latitudes during disturbed geomagnetic conditions. Fortunately, since 2005, SuperDARN started to expand to mid-latitudes (red radars in Figure 1.2).

1.1.2.2 The mid-latitude SuperDARN radars

Though originally designed to follow auroral expansion during active periods [e.g., *Baker et al.*, 2007], mid-latitude SuperDARN radars have observed ground and ionospheric scatter revealing several interesting and unexpected features of the mid-latitude ionosphere during periods of moderate to low geomagnetic activity [e.g., *Greenwald et al.*, 2006; *Clausen et al.*, 2012]. The past 7 years' expansion of SuperDARN to mid-latitude, combined with the recent extended solar minimum provides access to a large-scale continuous view of the sub-auroral ionosphere for the first time. Helped by a reliable characterization of HF propagation and its influence on SuperDARN observations, we can develop an understanding of some of the most prominent recurring features of the sub-auroral ionosphere during quiet geomagnetic conditions.

1.2 Research Objectives

Section 1.1 has hinted at the great variety of observable sub-auroral ionospheric phenomena. It has also shown that HF propagation introduces significant ambiguities in SuperDARN observations. Consequently, a proper understanding of HF propagation in the mid-latitude ionosphere would be a major asset to the study

of ionospheric phenomena using SuperDARN observations. This can be achieved by developing a proper model of HF propagation in a realistic ionosphere. However, Section 1.1.1 described the variety of dynamic factors driving ionospheric conditions, making a realistic representation of the ionosphere a complex endeavor which many models have addressed for decades with various degrees of success [e.g., *Huba et al.*, 2000; *Schunk et al.*, 2004; *Zhang and Holt*, 2007; *Bilitza et al.*, 2011a]. The recent expansion of SuperDARN to sub-auroral latitudes, combined with a focus on quiet geomagnetic conditions, provides a unique set of both data and ionospheric conditions which enables a simplified and more reliable model of HF propagation effects in SuperDARN observations. In order to establish the reliability and accuracy of such a model, it needs to be tested against prominent and recurring features of the ionosphere.

Thus, the purpose of this research is to identify and characterize prominent recurring features of the sub-auroral ionosphere under quiet geomagnetic conditions. For this purpose, a new ray-tracing model of HF propagation in the quiet-time sub-auroral ionosphere has been developed, validated, and optimized for comparison with SuperDARN observations. This model is used in the comprehensive analysis of two sub-auroral ionospheric features.

First, we investigate a Summer Evening Anomaly (SEA) in ground backscatter first observed with the Blackstone SuperDARN radar [*Ravindran-Varrier*, 2010]. We conduct a detailed analysis of the backscatter occurrence and morphology, as well as the related ionospheric feature which we show to be an unexpected increase in electron densities, possibly driven by thermospheric neutral winds modulated by the geomagnetic field configuration.

Next, following observations by *Greenwald et al.* [2006] and a thorough statistical occurrence survey by *Ribeiro et al.* [2012], we investigate the characteristics of nighttime low-velocity Sub Auroral Ionospheric Scatter (SAIS). Specifically, we find that the ionospheric irregularities responsible for SAIS are widespread throughout the mid-latitude ionosphere, and located in the bottom-side F-region. We also show that the Temperature Gradient Instability (TGI) is likely responsible for

the observed irregularities, which grow at kilometer scale-length in the top-side F-region and cascade to decameter-scale in the bottom-side F-region.

The two ionospheric phenomena studied in the course of this research directly relate to one of the four overarching science goals identified by the 2013-2022 Decadal Survey [*National Academy of Sciences*, 2013]:"Goal 2 - Determine the dynamics and coupling of Earth's magnetosphere, ionosphere, and atmosphere and their response to solar and terrestrial input". Most significantly, outcomes of this research have the following wider implications:

- Reveal previously unsuspected features of the sub-auroral ionosphere
- Improve our understanding of sub-auroral ionospheric irregularities, their location within the sub-auroral ionosphere and their relation to the plasma environment
- Enhance ionospheric diagnostics from SuperDARN observations

1.3 Organization of the Dissertation

Chapter 1 has begun our discussion with a review of relevant literature on the mid-latitude ionosphere under quiet-geomagnetic conditions and SuperDARN radars. Chapter 2 will proceed with a detailed description of the ray-tracing model developed and used to analyze SuperDARN observations. In particular, choices made for the background ionosphere and backscatter identification will be discussed in this chapter. Next, Chapter 3 will illustrate an application of HF propagation modeling to explain an anomaly in SuperDARN ground backscatter observations occurring around sunset during the summer, a.k.a. the Summer Evening Anomaly (SEA). Chapter 4 will extend the same analysis to the more complex case of ionospheric backscatter, with focus on low-velocity Sub-Auroral Ionospheric Scatter (SAIS). Results from this chapter will then be leveraged in Chapter 5 to estimate the role of the Temperature Gradient Instability in the growth of irregularities associated with low-velocity SAIS. Chapter 6 will outline conclusions and propose future developments relevant to the present work.

Chapter 2

Ray-tracing Model

A significant part of the research conducted during this PhD relies on understanding HF propagation in a realistic mid-latitude ionosphere. Originally, a ray-tracing package developed by *Jones and Stephenson* [1975] was used. However, several difficulties arose due to both the programming language (Fortran77), and the age of this package. Consequently, a new model was designed and specifically optimized to be used in combination with SuperDARN data.

Coleman [1998] presented a 2-dimensional (2-D) ray-tracing formulation which was showed to provide results very similar to full 3-D models and was successfully compared to ionosonde data. I tested the implementation of this 2-D formulation against the *Jones and Stephenson* [1975] 3-D formulation and observed very small differences, well below SuperDARN's best sensitivity.

This Chapter details the derivation of this 2-D formulation (Section 2.1) as well as its numerical implementation (Section 2.2). I also provide some important details about the computation of the refractive index used in the ray-tracing model (Section 2.3). Finally, some statistics about the computational performance of the model are presented (Section 2.5). For details about the algorithm design, please refer to Appendix A.

2.1 Ray-tracing equations

The travel time T of an Electro-Magnetic (EM) wave packet between two points A and B can be expressed as:

$$T = \int_A^B \frac{ds}{v(s)} \tag{2.1}$$

where ds is an infinitesimal element of the ray path s, and $v(s)$ is the phase velocity of the wave packet along the ray path.

We also define the phase path S as:

$$S = cT = \int_A^B \mu(s) ds \tag{2.2}$$

where c is the speed of light and $\mu(s)$ is the refractive index along the ray path.

To account for the Earth's sphericity ds is expressed in polar coordinates. Equation 2.2 yields:

$$S = \int_A^B \mu(r,\theta) \left[\left(\frac{dr}{d\theta} \right)^2 + r^2 \right]^{1/2} d\theta \tag{2.3}$$

In order to find the ray path, S needs to be minimized. Equation 2.3 is of the form:

$$S = \int_A^B L\left(\theta, r, \frac{dr}{d\theta}\right) d\theta \tag{2.4}$$

which is stationary (i.e., minimum in the context of ray-tracing) when r satisfies the Euler-Lagrange equation:

$$\frac{\partial L}{\partial r} - \frac{d}{d\theta}\left(\frac{\partial L}{\partial \frac{dr}{d\theta}} \right) = 0 \tag{2.5}$$

From equations 2.3 we obtain the partial derivatives of $L\left(\theta, r, \frac{dr}{d\theta}\right)$:

$$\frac{\partial L}{\partial r} = \frac{\partial \mu}{\partial r}\sqrt{\left(\frac{dr}{d\theta}\right)^2 + r^2} + \frac{\mu r}{\sqrt{\left(\frac{dr}{d\theta}\right)^2 + r^2}} \tag{2.6a}$$

$$\frac{\partial L}{\partial \frac{dr}{d\theta}} = \frac{\mu \frac{dr}{d\theta}}{\sqrt{\left(\frac{dr}{d\theta}\right)^2 + r^2}} \tag{2.6b}$$

For clarity of notation, we define Q as:

$$Q = \frac{\mu \frac{dr}{d\theta}}{\sqrt{\left(\frac{dr}{d\theta}\right)^2 + r^2}} \tag{2.7}$$

which yields:

$$\frac{dr}{d\theta} = \frac{rQ}{\sqrt{\mu^2 - Q^2}} \tag{2.8}$$

From equations 2.5, 2.6 and 2.8 we have:

$$\frac{dQ}{d\theta} = \frac{r}{2\left(\mu^2 - Q^2\right)}\frac{\partial \mu^2}{\partial r} + \sqrt{(}\,\mu^2 - Q^2) \tag{2.9}$$

We introduce the group path P' such that:

$$dP' = \frac{ds}{\mu} = \frac{dr}{Q} \tag{2.10}$$

This allows us to express the two differential equations 2.8 and 2.9 in terms of the group path P':

$$\frac{dQ}{dP'} = \frac{1}{2}\frac{\partial \mu^2}{\partial r} + \frac{\mu^2 - Q^2}{r} \tag{2.11a}$$

$$\frac{dr}{dP'} = Q \tag{2.11b}$$

$$\frac{d\theta}{dP'} = \frac{\sqrt{\mu^2 - Q^2}}{r} \tag{2.11c}$$

The above equations 2.11 can be solved at each ray step to obtain the next position in (r, θ) space. This process is repeated as many times as necessary, until

r is above a certain altitude (penetrating rays), $r = R_E$ where R_E is the Earth radius (rays reaching the ground), or the number of steps in a given ray exceeds a specified threshold (ducted rays). These considerations are important in the numerical integration of equations 2.11, which is discussed in the next Section.

2.2 Numerical scheme

The ray-tracing program integrates the ray-tracing equation (2.11) using an adaptive step-size Runge-Kutta method as described in Numerical Recipes in C: the Art of Scientific Computing [*Press et al.*, 2002, Chap. 16.2]. For clarity, we reproduce here the algorithm used.

The main integration is performed with a fifth order Runge-Kutta formula:

$$f_{n,0} = f_n \tag{2.12a}$$

$$f_{n,1} = f_n + b_{21} f'_{n,1} h \tag{2.12b}$$

$$f_{n,2} = f_n + \left(b_{31} f'_{n,1} + b_{32} f'_{n,2}\right) h \tag{2.12c}$$

$$f_{n,3} = f_n + \left(b_{41} f'_{n,1} + b_{42} f'_{n,2} + b_{43} f'_{n,3}\right) h \tag{2.12d}$$

$$f_{n,4} = f_n + \left(b_{51} f'_{n,1} + b_{52} f'_{n,2} + b_{53} f'_{n,3} + b_{54} f'_{n,4}\right) h \tag{2.12e}$$

$$f_{n,5} = f_n + \left(b_{61} f'_{n,1} + b_{62} f'_{n,2} + b_{63} f'_{n,3} + b_{64} f'_{n,4} + b_{65} f'_{n,5}\right) h \tag{2.12f}$$

$$f_{n+1} = f_n + \left(c_1 f'_{n,1} + c_2 f'_{n,2} + c_3 f'_{n,3} + c_4 f'_{n,4} + c_5 f'_{n,5} + c_6 f'_{n,6}\right) h \tag{2.12g}$$

The error is estimated using the following embedded fourth order formula:

$$\Delta_f = f_{n+1} - f^*_{n+1} = \left(c^*_1 f'_{n,1} + c^*_2 f'_{n,2} + c^*_3 f'_{n,3} + c^*_4 f'_{n,4} + c^*_5 f'_{n,5} + c^*_6 f'_{n,6}\right) h \tag{2.13}$$

In the above equations, a_i, b_{ij} and c_i and c^*_i are the Cash-Karp constants given in table 2.1, $h = dP'$ is the integration step, f represents Q, r and θ, and f' is

obtained from equation 2.11:

$$r'_{n,i} = Q_{n,i-1} \tag{2.14a}$$

$$\theta'_{n,i} = \frac{\sqrt{\mu^2 - Q^2_{n,i-1}}}{r_{n,i-1}} \tag{2.14b}$$

$$Q'_{n,i} = \frac{1}{2}\frac{\partial \mu^2}{\partial r} + \frac{\mu^2 - Q^2_{n,i-1}}{r_{n,i-1}} \tag{2.14c}$$

i	a_i	b_{ij}					c_i	c^*_i
1							$\frac{37}{378}$	$\frac{2825}{27648}$
2	$\frac{1}{5}$	$\frac{1}{5}$					0	0
3	$\frac{3}{10}$	$\frac{3}{40}$	$\frac{9}{40}$				$\frac{250}{621}$	$\frac{18575}{48384}$
4	$\frac{3}{5}$	$\frac{3}{10}$	$\frac{-9}{10}$	$\frac{6}{5}$			$\frac{125}{594}$	$\frac{13525}{55296}$
5	1	$\frac{-11}{54}$	$\frac{5}{2}$	$\frac{-70}{27}$	$\frac{35}{27}$		0	$\frac{277}{14336}$
6	$\frac{7}{8}$	$\frac{1631}{55296}$	$\frac{175}{512}$	$\frac{575}{13824}$	$\frac{44275}{110592}$	$\frac{253}{4096}$	$\frac{512}{1771}$	$\frac{1}{4}$
$j =$		1	2	3	4	5		

Table 2.1. Cash-Karp Parameters for Embedded Runga-Kutta Method [*Press et al.*, 2002].

We control for numerical stability using Δ_Q only, by scaling it with respect to:

$$\Delta_{Q,0} = \epsilon \mu^2 \left(r_{n+1} - r_n\right) h \tag{2.15}$$

where $\epsilon = 10^{-3}$ is the error threshold which was estimated by comparing results from our numerical scheme to results from a well accepted ray-tracing code developed by *Jones and Stephenson* [1975]. For the integration to be considered stable, we require:

$$\frac{\Delta_Q}{\Delta_{Q,0}} < 1 \tag{2.16}$$

Finally, depending on the outcome of the stability condition equation 2.16, h is either increased or reduced and constrained between 1 m and 10 km.

$$h_{n+1} = \begin{cases} h_n S \left| \frac{\Delta_Q}{\Delta_{Q,0}} \right|^{0.2} & \text{if } \frac{\Delta_Q}{\Delta_{Q,0}} \geq 1 \\ h_n S \left| \frac{\Delta_Q}{\Delta_{Q,0}} \right|^{0.25} & \text{if } \frac{\Delta_Q}{\Delta_{Q,0}} < 1 \end{cases} \tag{2.17}$$

where $S = 0.9$ is a safety factor to further insure stability.

The implementation of the numerical scheme described in this section is illustrated in Appendix A. One last important aspect of the ray-tracing model is the computation of the refractive index used in the above scheme, which is described in the following section.

2.3 Refractive index

The most fundamental parameter in the equations derived in Section 2.1 is the refractive index μ. If set to $\mu = 1$, then equation 2.8 becomes $S = cT = \|AB\|$, and rays propagate in a straight line. It is the value of μ at a given ray step which determines the position of the next step, as well as, to some extent, the length of said step.

The refractive index is a proxy expressing the degree to which electrons, ions, magnetic fields and particle collisions affect an electromagnetic wave at a given frequency [*Davies*, 1990]. The formula for the refractive index is usually associated with Sir Edward Appleton, and in its simplest form (ignoring magnetic field and collision effects) is expressed as:

$$\mu^2 = 1 - \frac{N_e e^2}{\epsilon_0 m \omega^2} = 1 - 80.5 \frac{N_e}{f^2} \tag{2.18}$$

where N_e is the electron density in m^{-3} and f is the EM wave frequency in Hz, and ϵ_0 is the permittivity of free space in $F\ m^{-1}$, e the electron charge in J, m the electron mass in kg and ω the angular wave frequency in $rad\ s^{-1}$.

This simplified expression of the Appleton formula needs some justifications. First, in the E and F regions, the effect of electron collisions is negligible since the wave frequency is much larger than the electron collision frequency. Second, SuperDARN frequencies are on the order of ∼10 MHz, or ∼60 rad/s, which is

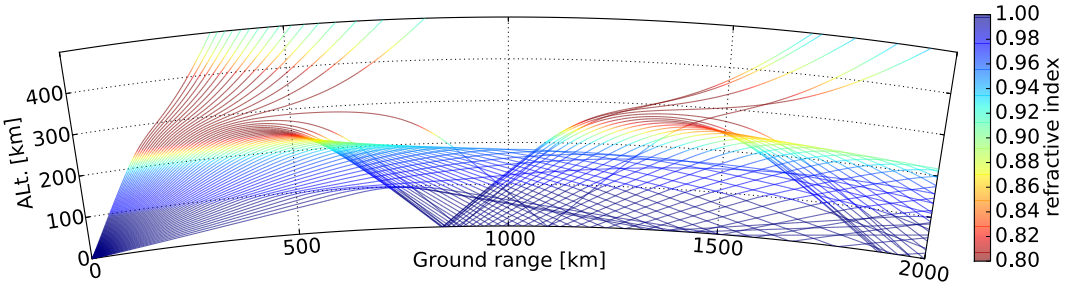

Figure 2.1. Ray-tracing results for a single time, single azimuth and single frequency, with elevation ranging from 5° to 60° in 1° increments. The refractive index computed from IRI and the simplified Appleton formula along each ray paths is shown with the color scale.

more than an order of magnitude larger than typical electron cyclotron frequencies in the E and F regions. This alone could justify ignoring magnetic field effects of SuperDARN signal propagation. The implication of these assumptions, other than computational simplicity, is that ordinary and extraordinary waves follow the same path. While this last point may be an oversimplification, SuperDARN radars consist of linearly polarized antennas which cannot measure polarization.

While these aspects are important to understanding how the model is specifically tailored for SuperDARN radars, it may not yet be clear how the refractive index is computed in the model. From equation 2.18, for a given SuperDARN operating frequency, note that the electron density is the only unknown parameter. Fortunately, electron densities are commonly measured in the ionosphere using a variety of instruments such as ionosondes, Incoherent Scatter Radars (ISRs), spacecraft and rocket mounted Langmuir probes and more [e.g., *Schunk and Nagy*, 2009, ch. 14]. While we could look for co-located measurements for every model run, this process would likely fail more often than not. Once again, a long history of ionospheric research provides the tool we need in the shape of empirical models. These models, most well known of which is the International Reference Ionosphere (IRI), assimilate data from a variety of instruments, over long periods of time and conditions (daily, seasonal, solar, geomagnetic).

The default model used with this ray-tracing implementation is IRI. This model has been shown to be satisfactory at reproducing E and F region electron density

profiles in the sub-auroral ionosphere [*Oyeyemi and McKinnell*, 2008]. For each model run, a 2-D ionospheric profile is generated extending for 2500 km along the propagation azimuth and for 500 km upward. Then, as the ray propagates, the electron density is linearly interpolated at each step and used to compute the refractive index using equation 2.18. The IRI model could easily be substituted for any other model or regularly spaced 2-D arrays of electron density values. Figure 2.1 shows the refractive index along each ray path as computed by the ray-tracing model coupled with IRI, clearly identifying the F-region (200 to 400 km) as the main source of refraction.

2.4 Backscatter identification

In order to compare the ray-tracing results to SuperDARN observations, the slant range distribution of ionospheric and ground backscatter needs to be modeled. Figure 2.2 illustrates the two common types of backscatter observed by SuperDARN radars, namely ionospheric and ground scatter.

- *Ground Scatter*

Each ray reaching the ground after reflection in the ionosphere is identified as ground scatter, and the number of rays falling into each 45 km slant-range bin is counted. The count is then weighted by $1/r^3$, where r is the slant-range of a given bin (i.e., the length of a grey ray to the scatter point). The $1/r^3$ weight accounts for geometric power decay in the case where the ground acts as a backscatter target. In this case, the target's size increases linearly with range, thus compensating in part for the $1/r^4$ geometric power decay. Terrain geometry and reflective properties are ignored in this model. Note that the most distinct characteristic of ground scatter in SuperDARN obsertions is the skip focusing distance, *i.e.*, the closest region where rays reach the ground after reflection in the ionosphere. This is observed in Figure 2.1 as the concentration of rays reaching the ground near 800 km ground range. Comparing the modeled skip focusing distance with the one observed by SuperDARN radars can reveal information about the true height and density of

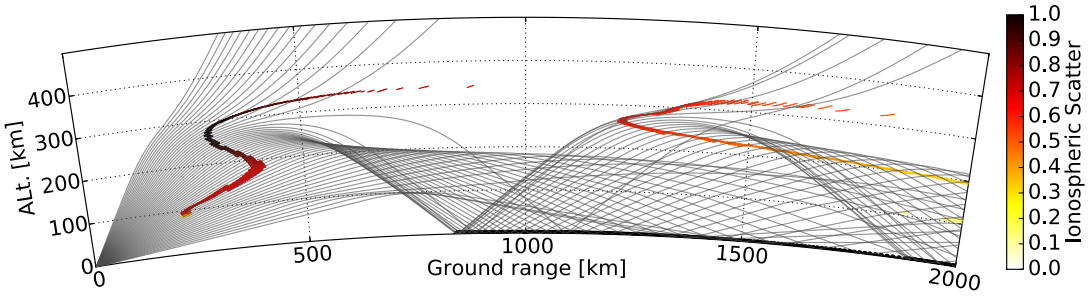

Figure 2.2. Ray-tracing results for a single time, single azimuth and single frequency, with elevation ranging from 5° to 60° in 1° increments. The relative ionospheric scatter distribution is indicated with the color shading, and ground scatter is marked as a thick black line at ground level. Rays are plotted as gray curves.

the F-region.

- *Ionospheric Scatter*

Ionospheric scatter predictions are based on the relative orientation of the background magnetic field with each ray. For field-aligned ionospheric irregularities, maximum backscatter power is obtained when the radar wave vector $\mathbf{k}$ is nearly orthogonal to the geomagnetic field $\mathbf{B}$. The angle between $\mathbf{k}$ and $\mathbf{B}$ is the complement of the aspect-angle α and is calculated at each ray-path step: if α is within 1° of orthogonality, the current step is marked as potential ionospheric scatter, and the respective slant-range r and electron density N_e are stored. Each marked ray step is then weighted by N_e^2/r^3. This weight accounts for geometric power decay and spatial variation of irregularity intensity, which is assumed to be proportional to the squared background plasma density (see [*Ponomarenko et al.*, 2009]). The scaling of irregularity intensity as N_e^2 holds when the relative amplitude of density fluctuations is constant throughout the ionosphere. The resulting backscatter power for each 45 km slant-range bin is then calculated as a sum of the weighted powers for respective steps. This approach to modeling ionospheric scatter effectively assumes a uniform irregularity distribution. If IRI provides a realistic ionosphere then the true irregularity distribution is the main source of differences between the modeled and observed distributions of ionospheric scatter.

The distributions presented in Figure 2.2 are repeated for a given period of time and across a number of beams in order to build both range-time and field-of-view plots, which can then be directly compared to SuperDARN observations.

2.5 Parallel implementation

One final step of the ray-tracing implementation has to do more with programming considerations than model design, but is worth understanding nonetheless. Due to the 2-D formulation, this ray-tracing model already achieves a very good speed-accuracy compromise. However, due to the large amount of SuperDARN data it can potentially be compared to, it can never be fast enough. For this reason, a parallel implementation of the model was designed using the Message Passing Interface (MPI) [*Pacheco*, 1996; *Gropp et al.*, 1999].

The ray-tracing is "*embarrassingly parallel*" since each ray, at each time, along each azimuth can be calculated independently. However, each ray path calculation requires knowledge of the full ionosphere, and rays propagating along the same azimuth at the same instance of time can use the same ionosphere. Consequently, in spite of the embarrassingly parallel nature of the problem, care has to be taken to optimize memory usage and disk access. The strategy used here is to first distribute the time and/or azimuth iterations to different threads, while keeping the rays at a given time and azimuth on a single process. Then, the ionospheric profile needs only be computed and stored once for a given time and azimuth.

Tests have been performed on the new Virginia Tech SuperDARN servers to evaluate the performance of the parallel code. Results are presented in Figure 2.3 and show a nearly linear increase of the computational speed. Ideally, for an embarrassingly parallel problem, computational speed should be exactly proportional to the number of processes. However, each ray path step is stored dynamically in files, which are accessed atomically using MPI buit-in I/O functions. Given the large average number of ray paths and steps per ray paths, disk access becomes saturated and acts as a bottleneck in the model execution. However, a full day with a 30 minute time resolution for a radar with 24 beams and an elevation range

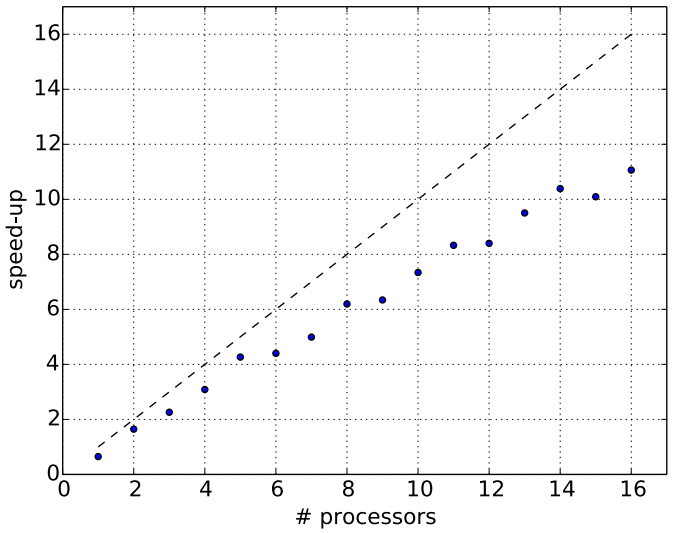

Figure 2.3. Factor of increase in computational speed versus number of processors (blue markers). The ideal case (dashed line) represents the expected speed-up if all computational time was spent on calculating ray paths. The deviation from ideal behavior is due to disk input/output limits.

between 5° and 60° with a 0.1° increment completes in ∼80 s with 12 processors. This computation time is more than reasonable and enables statistical analysis of HF propagation compared to SuperDARN observations.

This final step in the ray-tracing model implementation allows us to offer access to it via a web interface hosted on our servers (http://vt.superdarn.org/ray-tracing). I hope this openness can benefit the SuperDARN community and allow for easy and fast reproduction of published results. The model is also distributed as part of our new Space Science Toolkit (see Appendix C).

Chapter 3

The Summer Evening Anomaly

Based on de Larquier, S., J. M. Ruohoniemi, J. B. H. Baker, N. Ravindran Varrier, and M. Lester (2011), First observations of the midlatitude evening anomaly using Super Dual Auroral Radar Network (SuperDARN) radars, J. Geophys. Res., 116, A10321, doi:10.1029/2011JA016787.

In this chapter, we focus on a well defined recurring anomaly in SuperDARN ground backscatter. This provides an ideal application of the propagation analysis described in Chapter 2. Due to its characteristics, the anomaly studied in this chapter is named Summer Evening Anomaly (SEA). In the course of this research, the SEA has been successfully studied as follows:

- Statistical analysis of daily ground scatter distributions are compared to ray-tracing results, showing very good correlation, and suggesting that the anomaly is related to a well defined recurring ionospheric structure.
- The ray tracing show that the HF signature of the SEA is related to a rise of the F-region accompanied with an enhancement in F-region electron densities: this result is confirmed by observations from the Millstone Hill Incoherent Scatter Radar (ISR).
- We relate this ground scatter feature to satellite observation suggesting the SEA is a global phenomenon.

- We investigate the role of neutral winds modulated by the geomagnetic field structure in the formation and global structure of the SEA.

Results on the Summer Evening Anomaly have also led to the identification of the Weddell Sea Anomaly in observations from the Falkland Island radar in the Southern Hemisphere [*Milan et al.*, 2013].

3.1 Introduction

Under geomagnetically quiet conditions, the daytime mid-latitude ionosphere is mainly influenced by solar radiation, tides, gravity waves and thermospheric neutral winds. Typically, electron densities in the ionosphere build up at sunrise through photoionization, maximize around solar noon, and decrease through sunset as photoionization becomes weaker than recombination. Seasonal and geographical variations apply to this simple model of the ionosphere, but any deviation of the daytime electron density variation from the sun exposure variation is usually considered an anomaly [e.g., *Schunk and Nagy*, 2009, ch. 11].

Previous work by *Evans* [1965] presented Incoherent Scatter Radar (ISR) observations of an enhancement in ionospheric electron densities occurring in the summer time around 20 LT over Millstone Hill, MA. *Evans* [1965] showed that soon after solar noon, the F layer density peak starts moving up as recombination happens faster at lower altitudes and electron densities are reduced, but around 16 LT the density peak stops recessing and electron densities reach higher values than at solar noon. *Evans* [1965] attributed this enhancement to the thermal contraction of the topside ionosphere. *Eccles and Burge* [1973] further investigated the summer evening enhancement in electron density described by *Evans* [1965]. Modeling results from [*Eccles and Burge*, 1973] suggested that the thermal contraction of the topside ionosphere has very little effect on the evening enhancement observed in the F-region, but equatorward thermospheric winds seem to be important. Due to the southward inclination of the magnetic field lines, equatorward directed meridional neutral winds can contribute to pushing the lower layers of the ionosphere up the field lines to higher altitude where recombination is slower,

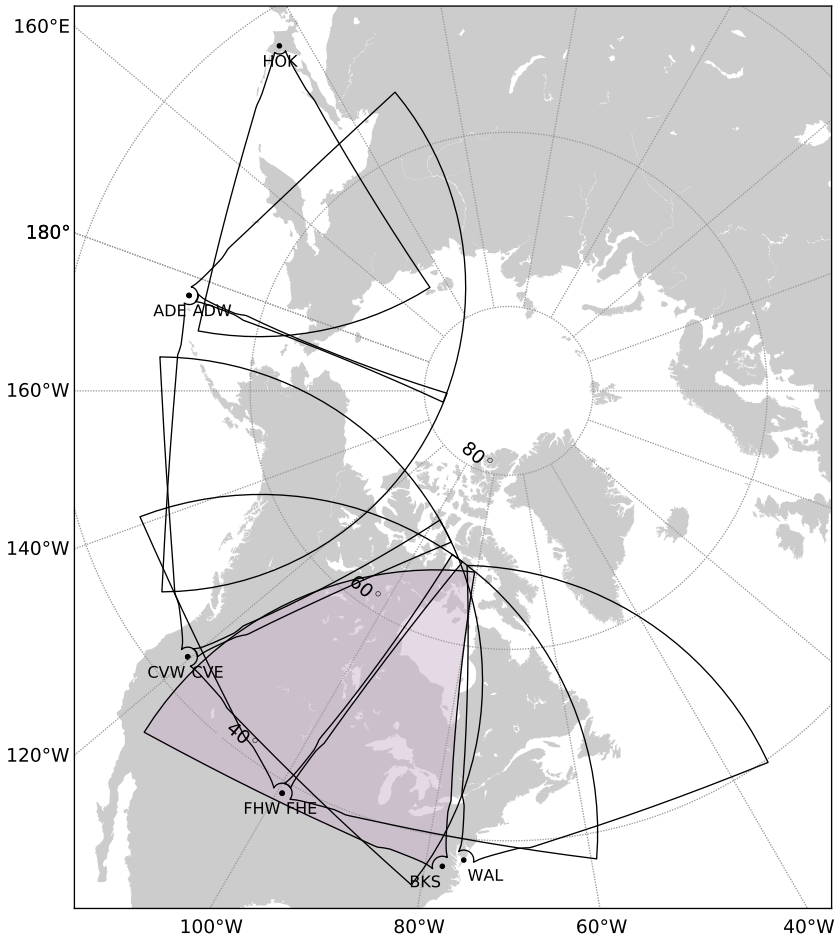

Figure 3.1. SuperDARN mid-latitude radars showing Hokkaido (HOK), Adak East and West (ADE and ADW), Christmas Valley East and West (CVE and CVW), Fort Hays East and West (FHE and FHW), Blackstone (BKS) and Wallops (WAL). Blackstone radar is represented by the shaded field-of-view. One more pair of radars is projected to be built in the Azores in 2013.

which may account for longer lived and higher electron densities in the evening F region. *Lei et al.* [2005], using all available data from the Millstone Hill ISR, also noticed that the evening enhancement was strongly dependent on solar activity: the evening enhancement for solar maximum appears much weaker than for solar minimum.

The recent development of mid-latitude Super Dual Auroral Radar Network (SuperDARN) radars shown in Figure 3.1 has revealed a similar anomaly in the High-Frequency (HF) propagation pattern. The SuperDARN HF radars have been successfully used to study a wide range of problems in high-latitude ionospheric

electrodynamics [*Chisham et al.*, 2007]. Most studies are based on HF signals backscattering from ionospheric irregularities that develop along geomagnetic field lines [e.g., *Ruohoniemi and Baker*, 1998]. The strong refraction of HF signals (8–18 MHz) in the ionosphere allows the backscattering conditions to be satisfied over an extended range interval, sometimes exceeding 3000 km. Figure 3.2 illustrates typical daytime (Figure 3.2a) and nighttime (Figure 3.2b) propagation paths for HF signals in the quiet mid-latitude ionosphere: it can be seen that during nighttime, the rays tend to propagate through a larger extent of the ionosphere and are consequently more likely to encounter ionospheric irregularities or to be attenuated before ground backscatter reaches the radar. The recent and still ongoing development of mid-latitude radars over North America and Japan has extended the coverage of SuperDARN (see Figure 3.1). Mid-latitude ionospheric conditions being generally less active, during the daytime the predominant mode of backscatter involves reflection from the ground after the HF signals are re-directed downward by refraction. This feature of HF propagation is used in over-the-horizon HF communication and radar surveillance [e.g., *Hughes et al.*, 2002]. Terrain geometry and composition usually result in part of the energy being scattered back to the radar, where it is identified as ground scatter due to very low velocities and spectral width [e.g., *Blanchard et al.*, 2009]. According to HF propagation theory, the reflected rays are focused in the vicinity of the skip zone boundary defined as the closest distance to the source where rays can reach the ground [e.g., *Budden*, 1966, p. 183-184]. See Figure 3.2a for an illustration of the skip focusing. The position and intensity of the ground scatter skip focusing can be used to retrieve information on the structure and evolution of the ionosphere [e.g., *Hughes et al.*, 2002]. Figure 3.3 shows an example of the position of F-region skip focusing (red band of scatter) in the Blackstone radar field of view.

While SuperDARN ground scatter has previously been used to study ionospheric dynamics such as traveling ionospheric disturbances or ULF waves [e.g., *Samson et al.*, 1989; *Bristow et al.*, 1996; *Ponomarenko et al.*, 2005], its potential for monitoring long term seasonal variations of the ionosphere remains largely unexploited

[*Milan et al.*, 1997b; *Norman and Dyson*, 2006]. Recent work by *Ponomarenko et al.* [2010] has demonstrated that seasonal and diurnal changes in the polar-cap ionosphere modulates the occurrence rate and spatial coverage of ground scatter. A proper understanding of the occurrence and evolution of ground scatter at mid-latitudes is required to retrieve accurate information on the state of the ionosphere, and can be used to test the accuracy of empirical models.

The expected evolution of daytime ground scatter on a geomagnetically quiet day ($Kp \leq 2$ and $|Dst| \leq 5$ nT) can be described as follows (See Figure 3.4a for illustration). When the sun rises, photoionization begins, rapidly increasing the electron densities in the ionosphere [e.g., *Kelley*, 2009, chap. 5], thus increasing the refractive index, resulting in an increasing number of HF rays being bent to the ground. The HF radar detects ground scatter which moves nearer in range as ionospheric plasma densities build up and the F-region peak density altitude is lowered. This process peaks around solar noon when the electron density is at its maximum. When the sun sets, photoionization nearly stops and recombination of electrons and ions dominates, reducing the plasma density and resulting in a decreasing number of rays being bent to the ground. The ground scatter moves outward in range and eventually vanishes as ionospheric plasma densities fall below the levels required to provide the refraction needed to generate ground scatter. The expected diurnal variation in the range-time format (Figure 3.4a) is U-shaped and nearly symmetrical about a range minimum near solar noon.

In this study we report that during geomagnetically quiet summer days, the daily ground scatter distribution observed at mid-latitude SuperDARN radars does not follow the expected diurnal pattern. As can be seen in Figure 3.4b, an enhancement in ground scatter occurs in the evening around sunset. The ground scatter activity then in fact exceeds the activity observed around solar noon. One of the results of the prolonged ground scatter after sunset is to provide an extended ability to monitor ionospheric dynamics via ground scatter in the evening sector.

Data from the Blackstone HF radar in Virginia (37.10°N, 282.05°E) collected over the first two years of operation provides the basis of the present work. Super-

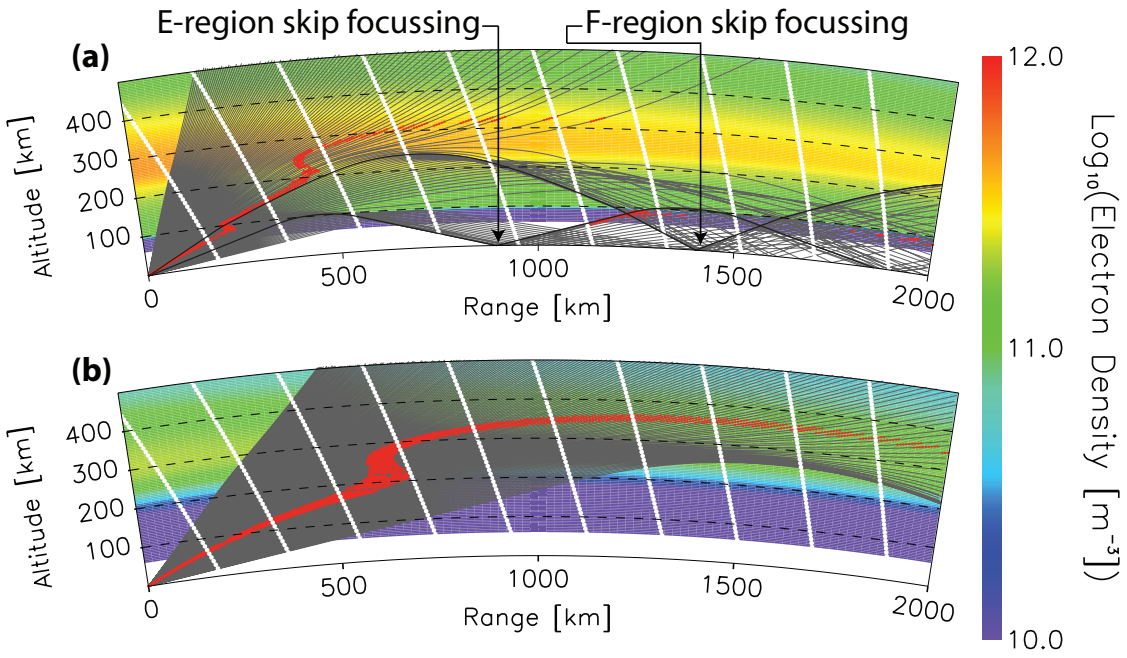

Figure 3.2. Typical (a) daytime and (b) nighttime HF ray propagation paths in the ionosphere obtained using ray-tracing coupled with an ionospheric specification provided by the IRI. E and F regions skip focusing are emphasized. The red highlighted areas represent regions of good magnetic aspect condition for reflection by field aligned ionospheric irregularities.

DARN observations in conjunction with ray-tracing model results are compared to previously published data from the Millstone Hill ISR (42.6°N, 288.5°E) [*Evans*, 1965; *Eccles and Burge*, 1973], and to CHAMP satellite observations reported by *Liu et al.* [2010].

This body of work was motivated by the identification of a peculiar and recurring feature in mid-latitude SuperDARN observations: an unexpected enhancement in ground backscatter around sunset. The relation between this feature and the previously reported Summer Evening Anomaly (SEA) will be demonstrated here. Based on this relation, we then provide the first comparison with global empirical models such as the International Reference Ionosphere (IRI) and the Horizontal Wind Model (HWM).

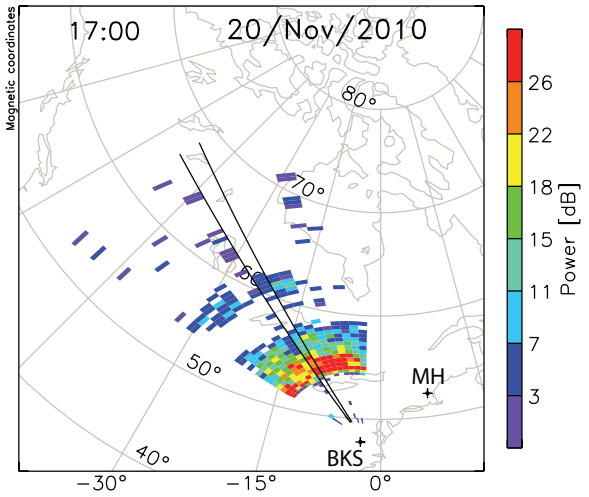

Figure 3.3. Single 16 beam scan from the Blackstone (BKS) radar illustrating the beam considered for all subsequent range-time analysis of SuperDARN data presented in this chapter. Also represented is the position of the Millstone Hill ISR (MH).

3.2 Data sets and analysis methods

The Blackstone radar (37.10°N, 282.05°E, shaded in Figure 3.1) has been operating since February 2008. Its field of view provides good coverage of the mid-latitude sector over central North America. The ongoing extension of the SuperDARN mid-latitude chain under the NSF Mid-Sized Infrastructures (MSI) program will provide wider coverage in the future. As daily distribution of ground scatter does not present a strong azimuthal dependence, data from beam 7 of the Blackstone radar (center beam) will be used in the following analysis (Figure 3.3). This section provides a general description of standard SuperDARN data presentation format; the figures introduced here will be described in greater details in the next section. Observations from the Blackstone SuperDARN radar are presented on a range-time plot: data from the center beam of Blackstone are collected with a time resolution of 1 min (see Figure 3.3 for a representation of Blackstone's beams), and the returned signal is binned into 45 km long range-gates (beginning at 180 km range), resulting in the representation presented in Figure 3.4. The daytime ground scatter is identified by low velocities and small spectral width and usually manifests as a quasi-continuous block in the range-time domain lasting from sunrise

to sunset, as can be seen on Figure 3.4a.

The location of the Millstone Hill ISR with respect to the Blackstone radar shown in Figure 3.3 allows for effective comparison of Blackstone data with Millstone Hill observations, thus providing a different perspective of ionospheric parameters such as electron density. The Madrigal database was used to provide ISR data from the Millstone Hill observatory as can be seen in Figure 3.5.

To provide a broader seasonal view of ground scatter daily distribution, we conduct a statistical study for specific months of a given year. We compute the mean ground scatter power for a given month in each range gate of beam 7 over time intervals of 30 min for each day of the given month. The power distribution for each day is then summed over the month and normalized by the maximum summed power. This method yields the statistical daily ground scatter distribution and relative intensity. The ground scatter flag provided in SuperDARN data files (based on low velocities and small spectral widths) is used to identify ground scatter echoes as a first order approximation: improved algorithms have recently been developed for ground scatter identification [*Ribeiro et al.*, 2011], which could potentially refine results from this statistical survey. Echoes with signal-to-noise-ratio lower than 6 dB are ignored, only data collected on operating frequencies between 10 and 12 MHz are considered, and days with more than 5 hours of missing data are excluded. Months are selected to represent specific seasonal characteristics of the mid-latitude ionosphere. Results from this statistical analysis are presented in Figure 3.6.

To properly interpret ground scatter signatures in terms of ionospheric behavior, HF propagation in the ionosphere can be modeled using ray tracing [e.g., *Hall et al.*, 1999]. We use the ray tracing code developed by *Jones and Stephenson* [1975] coupled with the latest International Reference Ionosphere (IRI) model [*Bilitza*, 2001]. F10.7 values for 2010 provided online by NOAA/NGDC are added to the IRI coefficients files, and the built-in IGRF model was completed with IGRF-11 coefficients to have a fully updated model. IDL wrappers have been developed to allow for easy comparison between SuperDARN data and ray tracing results:

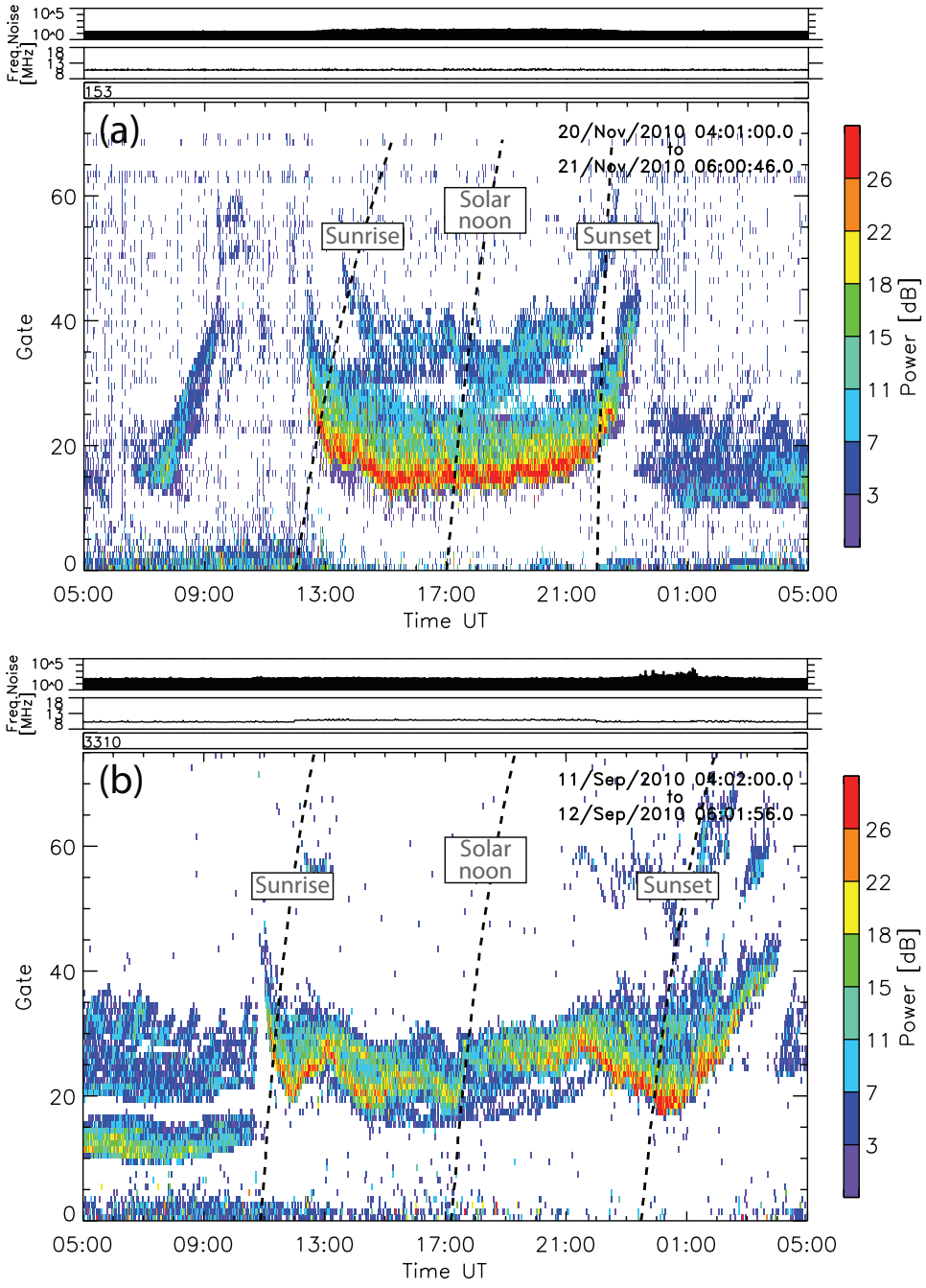

Figure 3.4. SuperDARN observations from Blackstone radar site for (a) a typical magnetically quiet winter day and (b) a typical magnetically quiet fall day. In (a) the ground scatter occurs between sunrise and sunset, when in (b) ground scatter signatures extend 4 hours after sunset. Outside of these limits, the returned signal is from sub-auroral ionospheric irregularities in these particular cases. Sunrise, solar noon and sunset time are computed in each range-cell of beam 7 of the Blackstone radar field-of-view.

in the wrapper, a radar, operating frequency and beam number can be selected, then the IRI is executed to generate background electron densities over an altitude range of 500 km and an ground range of 2500 km along the selected radar beam, and finally the ray tracing code is executed using the IRI density profile as a background ionosphere. Results from two single runs of the coupled raytracing-IRI model are presented in Figure 3.2. These single runs are repeated with the desired time resolution during a given time interval and collected to be presented on a range-time plot as described for the radar analysis. The ground scatter power distribution is re-constructed by counting the number of rays reaching the ground per 45 km range gates. Note that absorption and variations in ground properties are ignored in this modeling of ground scatter. Ray-tracing results designed to compare with radar statistical analysis are presented in Figure 3.7 and overlaid on Figure 3.6 (light shaded areas).

3.3 Results

3.3.1 Case studies

It has already been shown in Figure 3.4 that the ground scatter distribution during a typical geomagnetically quiet summer day (Figure 3.4b) may present significant differences from the winter distribution (Figure 3.4a). The first noticeable but not surprising difference is the time extent of the ground scatter being longer in summer (11 to 04 UT) than in winter (12 to 23 UT): this is simply due to longer sun exposure during the summer, resulting in longer lasting high electron densities (sunrise, sunset and solar noon times are obtained from NOAA/ESRL and defined by the solar zenith angle on the ground). The second and more subtle difference is the emergence of a two-band structure in the ground scatter (especially visible in the afternoon in Figure 3.4b): this is due to the presence of the ionospheric D-region and lower E-region during the spring, summer and early fall months, which creates a second, closer skip distance. A third difference is the stronger daytime returned power in the winter: this is explained by both the absence of a

lower E-region that would otherwise absorb and deflect part of the power reaching the F-region (which is responsible for the bulk of the ground scatter) and the winter anomaly which results in higher F-region densities in winter [*Rishbeth and Garriott*, 1969, p. 179-181]. The difference of greatest interest to this study is the enhancement in ground scatter that is observed to commence before sunset. The decay of the E-region before sunset will contribute to an enhancement in returned power from F-region related ground scatter, but would not account for the scatter moving closer in range as seen in Figure 3.4b: absorption and deflection from the lower E-region would have a stronger effect on rays with low elevation angles (see Figure 3.2) which do not contribute to the F-region skip focusing distance.

We have mentioned that previous observations from the Millstone Hill ISR revealed enhanced electron densities in the summer time evening mid-latitude ionosphere. The location of the Millstone Hill ISR with respect to the Blackstone radar shown in Figure 3.3 suggests that a relation may exist between the enhancement in ground scatter observed at Blackstone and the electron density enhancement observed at Millstone Hill. To verify this relation, a geomagnetically quiet day has been found in the Madrigal database when the Millstone Hill ISR was running long enough during a summer evening to provide both daytime and nighttime electron densities. Data from this day, August 13, 2010, are presented in Figure 3.5 with both SuperDARN (Figure 3.5a) and Millstone Hill (Figure 3.5b) observations. In Figure 3.5a, the evening enhancement in ground scatter clearly appears around sunset. Electron densities from Millstone Hill show both E and F regions during daytime, accounting for the strong attenuation of daytime signal in SuperDARN data, as well as the dissipation of the E-region before sunset. The electron densities in the two hours after sunset are notably higher than electron densities in the F region at solar noon. This electron density enhancement presents a very good correlation with the ground scatter enhancement in SuperDARN data, confirming a relation between the two. Increased electron densities also lead to a shorter skip focusing distance as was evidenced by the ground scatter signature moving from gate 25 (1305 km) to gate 20 (1080 km) in Figure 3.5a.

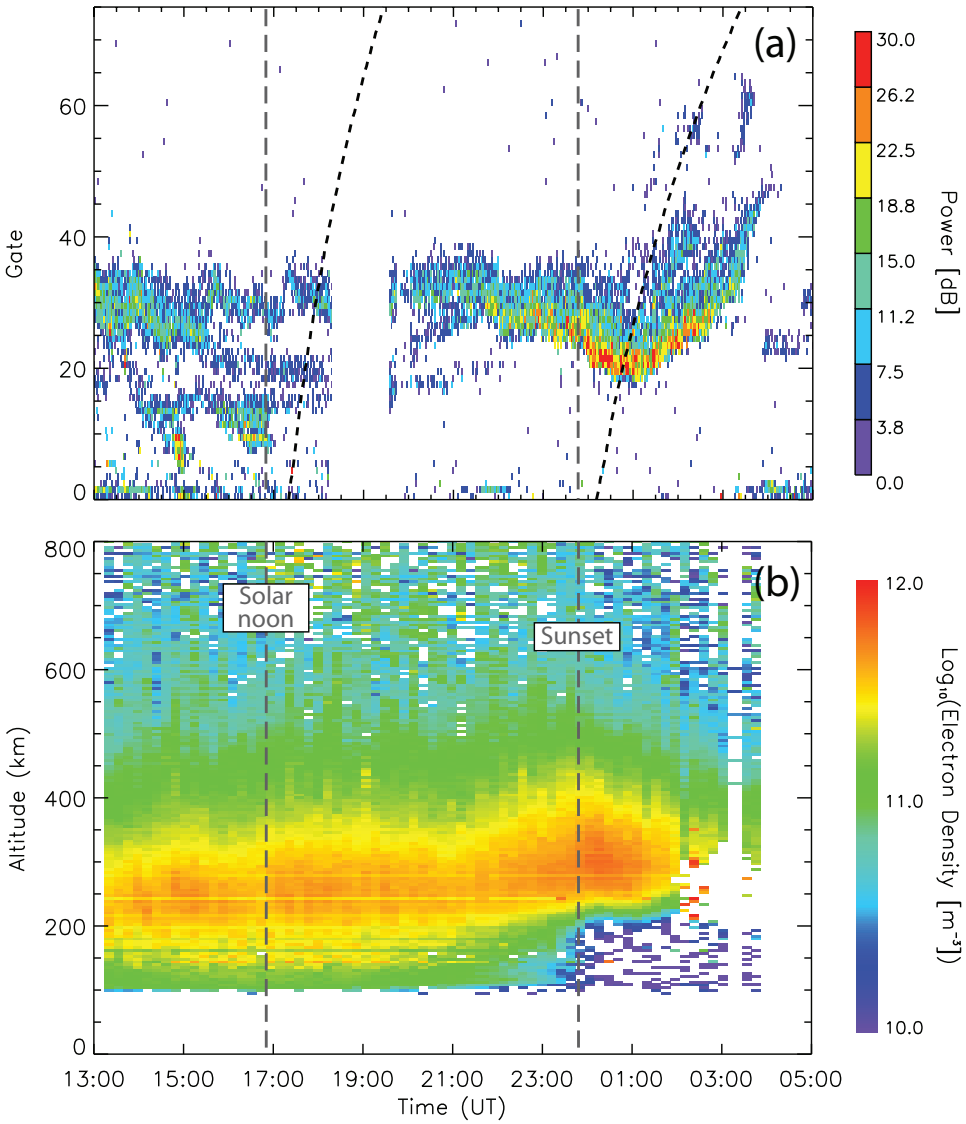

Figure 3.5. (a) SuperDARN observations from Blackstone beam 7 and (b) the Millstone Hill ISR on August 13^{th} 2010. The vertical dashed lines represent solar noon and sunset at the Millstone Hill radar site. The skewed dashed curves represent solar noon and sunset in the Blackstone radar field-of-view.

3.3.2 Statistical results

We now conduct a statistical survey of ground scatter power distribution during given months of 2010. We chose specific months that represent significant changes in the ground scatter pattern. Results are presented in Figure 3.6 and can be described as follows. In January, the daily ground scatter distribution presents the expected pattern centered on solar noon. No E-region ground scatter trace is ob-

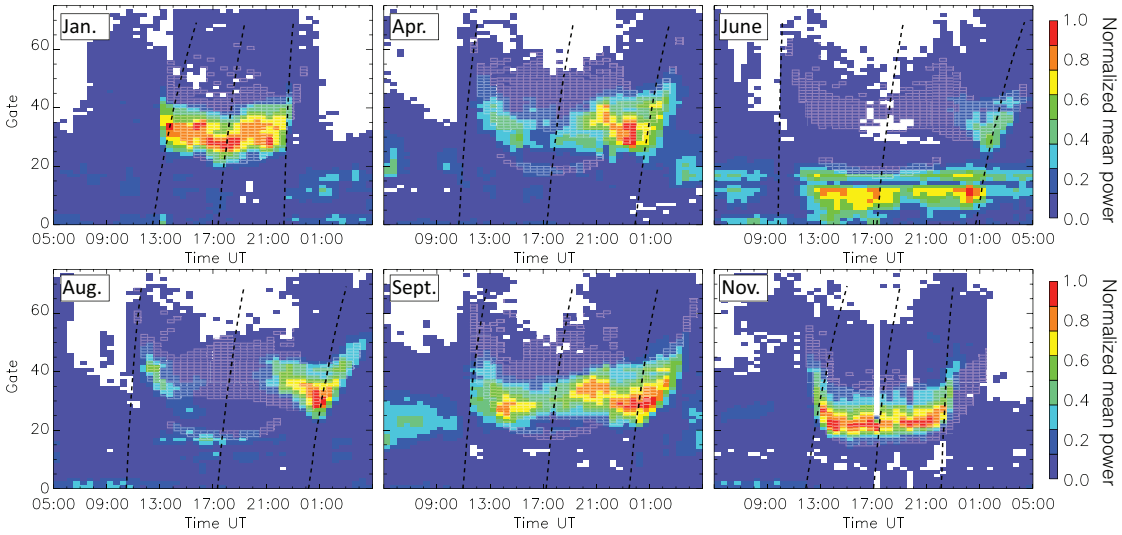

Figure 3.6. Daily variation of ground scatter observed by the Blackstone SuperDARN radar from statistical analysis of selected months of 2010. The light shaded areas correspond to modeled distribution of the ground scatter.

served. Through the evening sector, the power distribution is somewhat irregular but is dominated by the expected retreat to larger ranges. In April, the daytime ground scatter power distribution is strongly attenuated, and the strongest power is observed around sunset. April shows the first occurrence of the mid-latitude evening ground scatter enhancement. June daytime ground scatter is largely located at close ranges (before gate 20), which is typical of E-region activity. The F-region related ground scatter can only be observed around sunset, when F-region electron densities are enhanced and the E-region starts decaying. August exhibits a much reduced E-region activity compared to June, but the daytime power distribution of F-region related ground scatter is still largely absent: only around sunset can a strong ground scatter signature be observed. September presents a similar but not identical distribution as April. The daytime ground scatter is strongly attenuated but still presents a build-up around sunrise, and what seems like a retreat after solar noon followed by a new build-up before sunset, maximizing around sunset and finally retreating within 2-3 hours after sunset. Finally, November returns us to the expected symmetrical variation about solar noon. Though not shown in the results of Figure 3.6, some cases of a weak evening enhancement in ground

scatter are observed in October.

The strong daytime attenuations observed from April through September are due to E-region effects on propagation. First, the stronger electron densities in the daytime E-region introduce a two-way absorption of the F-region related ground scatter signal. Second, these enhanced electron densities also contribute to the refraction of the HF rays and a separate E-region related ground scatter signature may appear, thus preventing part of the signal from ever reaching the F-region. This effect is enhanced in June due to the occurrence of sporadic-E during most of the day. The E-region typically decays rapidly around sunset as recombination at these altitudes is much faster than in the F-region. Consequently, it should be noted that the dissipation of the E-region alone will result in an increased returned power from F-region related ground scatter: this increase, however, is not strong enough to account for the observed enhancement, as will be verified in the next section. As previously stated, the dissipation of the E-region also cannot account for a range reduction in the ground scatter skip distance around sunset as is observed from April to September.

The structure observed in September showing an initial recession of the ground scatter after solar noon suggests that the electron densities start decreasing and the F-region peak starts moving upward as would be expected and as illustrated in Figure 3.5b. The subsequent enhancement in ground scatter accompanied by shorter ranges suggest both that the electron densities are increasing and the F-region peak stops moving upward. The question remains as to whether the increase in electron densities should be attributed to a source of ionization other than solar radiation, to transport of ionized plasma from another sector of the ionosphere, or to a change in chemistry.

3.3.3 Modeling results

In order to compare ray tracing results to SuperDARN observations presented in Figure 3.6, an operating frequency of 11 MHz for Blackstone's beam 7 is selected and the code is executed for the 15^{th} of each selected month, with a 30 minute

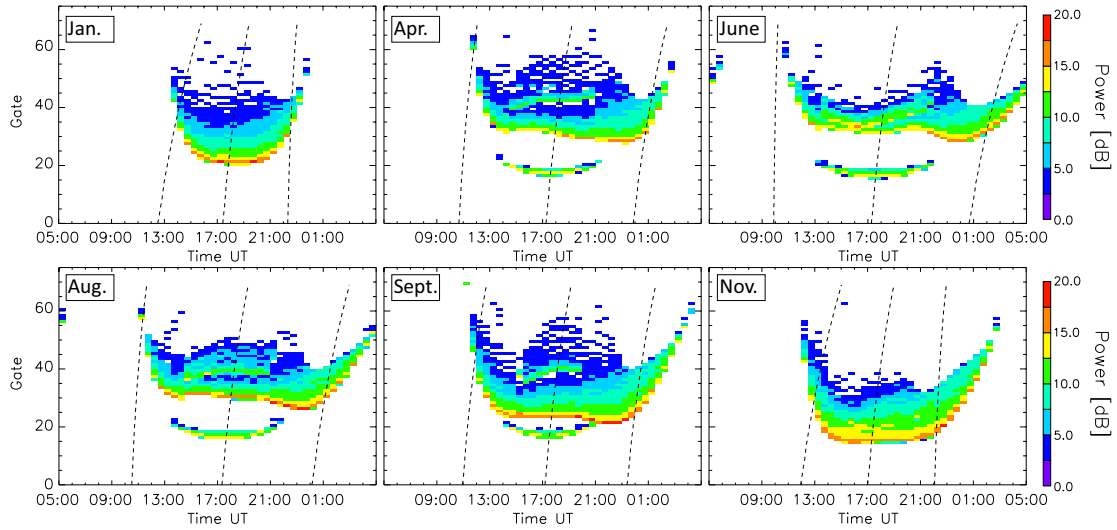

Figure 3.7. Ray-tracing [*Jones and Stephenson*, 1975] coupled with IRI modeling of ground scatter as would be observed by beam 7 of the Blackstone radar in 2010. The plotted power distribution represents the number of rays in each 45 km range-gate.

time resolution. The IRI model [*Bilitza*, 2001] is used to provide typical electron density profiles within the Blackstone field-of-view. Each 30 minute window such as the ones presented in Figure 3.2 are collected and presented on a range-time plot. The simulated initial elevation angles range from 10° to 35° in accordance with expected antenna characteristics and Blackstone's interferometer array measurements. Raytracing results are presented in Figure 3.7 as well as overlaid on Figure 3.6 (light shaded areas).

We compare the modeling results of Figure 3.7 with the observational results summarized in Figure 3.6. January and November present the diurnal pattern symmetrical around solar noon, which is both expected and captured in statistical results. From April to September, a weak ground scatter signature appears around gate 20 that is clearly distinct from the bulk of the ground scatter. Finally, the main ground scatter signatures from April to September are characterized by closer and enhanced ground scatter around sunset.

The weak ground scatter signature around gate 20 is related to the E-region bending part of the rays to the ground, further demonstrating the reason for weaker daily signals shown in radar observations. It should be noted that E-region signa-

tures observed in June (Figure 3.6) were mainly due to sporadic-E, which created an enhanced and disturbed E-region, thus explaining the difference between observations and modeling results in June. The occurrence of intense sporadic-E in June is not expressed by the IRI.

June and August show a very pronounced evening enhancement that is clearly detached from the daytime ground scatter: it is especially noticeable in June that the ground scatter starts recessing before sunset, but increases again through sunset, as can also be seen in radar observations in September (Figure 3.6). It is apparent that the decay of the E-region is correlated to the beginning of the evening enhancement, which confirms that it contributes to the enhancement in F-region related ground scatter. However, as can be seen in Figure 3.2, the F-region skip focusing boundary is associated with higher elevation angles, while the E-region skip focusing boundary is determined by lower elevation angles; consequently, the decay of the E-region cannot account for the decrease in skip focusing distance shown in both observations and modeling.

The comparison of observations and modeling demonstrates the blanking effect of the E layer, and the statistical occurrence of F-region ground scatter presented in Figure 3.6 conforms well to the modeling results. Unlike the summertime mid-latitude sporadic-E, the evening anomaly is very well captured by the IRI. Since the IRI density profiles provide a statistical picture of the ionosphere under standard geomagnetically quiet conditions, it is safe to assume that the evening enhancement in ground scatter is the signature of recurring seasonal ionospheric behavior at mid-latitudes over North America and not an isolated ionospheric perturbation.

3.4 Discussion

3.4.1 Comparison with recent satellite observations

Recent beacon tomography over Japan from *Thampi et al.* [2009] showed an enhancement in electron densities over latitudes greater than 33-34°N maximizing at ∼20-21 LT. Another recent study from *Lin et al.* [2010] reports FORMOSAT-

3/COSMIC observations showing a globally structured summer enhancement in electron densities. Both papers [*Thampi et al.*, 2009; *Lin et al.*, 2010] name this evening enhancement a Mid-latitude Summer Nighttime Anomaly (MSNA) which is also meant to include the Weddell Sea Anomaly (WSA). Results from both studies suggest that the Equatorial Ionization Anomaly (EIA) may be involved in the generating mechanism of the observed enhancement in addition to previously suggested thermospheric neutral winds.

A more comprehensive study by *Liu et al.* [2010] using data from the CHAMP satellite demonstrated that the North-Eastern American sector is part of a well defined mid-latitude summer phase reversal of the diurnal cycle: Figure 1 of [*Liu et al.*, 2010] shows that the region matching the SuperDARN and Millstone Hill observations labeled Northern Atlantic (NA), together with sectors of Eastern Asia (EA) and South Pacific (SP), present depleted daytime electron densities and enhanced evening/nighttime electron densities in the mid-latitude F region.

Assuming a constant eastward and equatorward wind at night and a westward and poleward wind during the day, *Liu et al.* [2010] suggested that the combined effects of neutral winds and the geomagnetic configuration could potentially explain both the daytime depletion and the nighttime enhancement in F-region electron densities. Additional constraints may apply to the neutral wind as altitude will affect the neutral-ion collision frequency, thus limiting the range of altitudes where the neutral winds can efficiently push the ionosphere up or down [e.g., *Kelley*, 2009, p.242-243]. It should also be noted that horizontal wind directions under 150 km altitude can be reversed compared to higher altitudes.

Liu et al. [2010] also suggests that the seasonal variation of the thermal contraction of the ionosphere may significantly contribute to the seasonal variation of the diurnal phase reversal. More modeling would be needed to verify this hypothesis, but earlier work by *Eccles and Burge* [1973] concluded that the thermal contraction of the ionosphere only contributed to modifying the structure of the topside ionosphere such that at high altitudes above the F-region the evening enhancement occurs earlier than it does at the F region peak.

A very recent study by *Burns et al.* [2011] used global maps of COSMIC NmF_2 and hmF_2 data for two months either side of the June and December solstices for 2006-2008, as well as a trace of the ground terminator and its magnetic conjugate. The authors conclude that if there is sufficient time between the crossing of the conjugate terminator first and the real terminator second at mid-latitude, an evening enhancement is observed near the real terminator. It should be noted that the distance between the terminator and its conjugate is directly related to field lines declination, which could impact neutral wind lifting efficiency as detailed in section 4.2. Additionally, *Burns et al.* [2011] suggest that the increase in hmF_2 does not occur at the same time as the increase in NmF_2 as would be expected if neutral winds were responsible for the enhancement. This delay between the lifting of the ionosphere and the electron density enhancement does not appear clearly in our data or in the figures shown in *Burns et al.* [2011]: one could also argue that recombination could start, lifting the F layer peak without resulting in a density enhancement, soon followed by a wind driven additional lift which would stall recombination by pushing ions to higher altitudes, thus producing enhanced F region densities. *Burns et al.* [2011] suggest that polarization electric fields could drive an upward poleward drift that would transport ions associated with the equatorial anomaly. *Burns et al.* [2011] points out that such a transport would require ion drift velocities higher than what is usually observed and that such a mechanism needs further quantitative investigation.

Two mechanisms have now been identified to potentially explain the evening enhancement: thermospheric neutral winds [*Eccles and Burge*, 1973; *Lin et al.*, 2010], and polarization electric fields coupled with inter-hemispheric conjugacy [*Burns et al.*, 2011].

3.4.2 Global models results

Having demonstrated the temporal evolution of the evening enhancement with both radar data (Figure 3.5-3.6) and ray-tracing results (Figure 3.7), we now wish to investigate the global spatial characteristics of this phenomenon. The signifi-

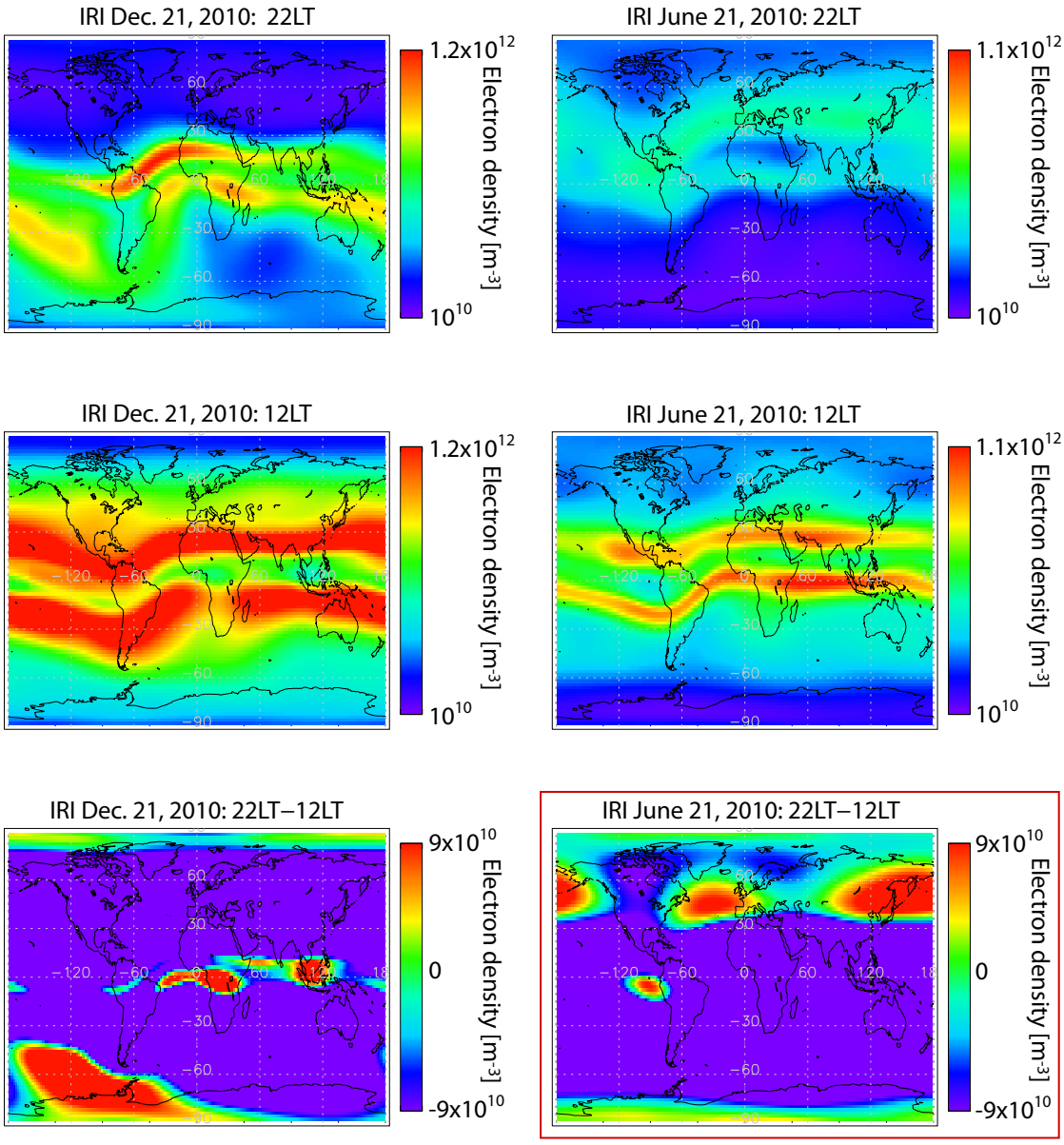

Figure 3.8. Global distribution of electron densities at 300 km altitude obtained with the IRI model [*Bilitza*, 2001]. The two lower maps are generated by subtracting electron densities at 12LT from those at 22LT to represent the intensity and coverage of the summer evening enhancement in both hemisphere. In the bottom panels, positive values are indicative of enhanced evening density, while negative values represent the expected evening reduction in electron density with respect to noon.

cance of the summer evening enhancement is such that it is safe to assume it should appear in a global empirical model such as the IRI [*Bilitza*, 2001]. Figure 3.8 shows a similar figure to the one obtained by *Liu et al.* [2010]: using IRI, electron densities at 300 km altitude are obtained for the summer and winter solstices. The bottom

panel (red box) shows the difference in electron densities between 20LT and 12LT, which clearly shows two sectors of evening enhancement in the Northern hemishere similar to those described by *Liu et al.* [2010]. It can be seen that SuperDARN measurements of the evening enhancement over North-Eastern America are at the edge of the active sector. It should be expected that the extended SuperDARN mid-latitude chain will be able to observe this longitudinal variation.

Using geomagnetic field configuration from the IGRF model combined with horizontal wind from the HWM07 model [*Drob et al.*, 2008] and the equation giving the effective vertical wind as a function of magnetic dip and declination angles [*Titheridge*, 1995, eq. 2], a map of effective vertical winds is presented in Figure 3.9 for the evenings of the summer and winter solstices. The top panels show the input parameters for the effective vertical wind computation: wind vectors at 150 km altitude and 20 LT are represented alongside magnetic dip angle isoclinic and magnetic field declination (positive Eastward, negative Westward). The altitude was chosen to represent a first order approximation of the mean altitude of a source layer to the evening enhancement in electron density. The bottom panels show the combination of horizontal winds at 150 km altitude with magnetic dip and declination into an effective vertical wind at 150 km altitude at 20 LT. The boxed panel is to be compared with the boxed panel of Figure 3.8. Thermospheric winds at 150 km in the Northern hemisphere result in efficient vertical winds with a longitudinal distribution very similar, though misaligned, to the electron density evening enhancement depicted in both IRI results (Figure 3.8) and satellite observations: strong vertical winds can be observed over two regions of the Northern hemisphere during the summer that are not reproduced in the winter. Finally, it is important to notice that there does not seem to be strong effective upward winds at this given altitude and local time during the winter solstice (left panels) that could account for the Weddell Sea Anomaly in the Southern hemisphere. However, it can be reasonably assumed that the HWM07 does not perform as well in the Southern Hemisphere as it does in the Northern. Limited data from the Southern Hemisphere results in less reliable empirical predictions: therefore, model results

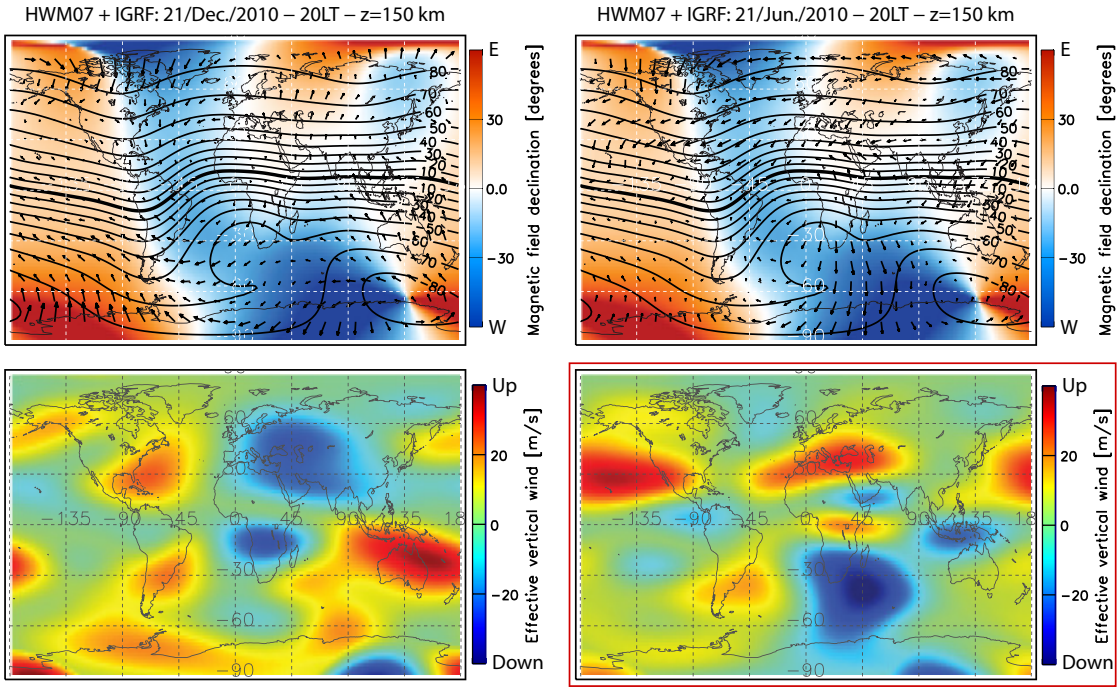

Figure 3.9. (Top panels) Vector wind velocities from HWM07 model [*Drob et al.*, 2008] at 20 LT at altitude 150 km for the summer and winter solstices (right and left, respectively), plotted over magnetic dip isoclinic and magnetic field lines declination from the IGRF model. (Bottom panels) Effective vertical winds computed using model results presented in the top panels [*Titheridge*, 1995, eq. 2].

for this hemisphere should not be interpreted as contradicting the influence of winds in the WSA.

In interpreting Figure 3.9, one has to take into account that the vertical wind influence covers a wide altitude range and this influence is mainly regulated by the ion-neutral collision frequency which decreases with altitude. Considering fixed altitude and time results presented in Figure 3.9, the strong effective vertical winds of 20 to 40 m/s at 150 km altitude modeled in the Northern hemisphere would result in enhanced F-region peak densities (300 km) about 1 to 2 hours later, which may account for the displacement of the longitudinal structure seen in comparing Figures 3.8 and 3.9. For example, the vertical wind enhancement that is centered on the Mediterranean in Figure 3.9 becomes responsible for the evening enhancement seen centered on the North Atlantic Ocean in Figure 3.8. More modeling is needed to evaluate the altitude dependency of the coupling between thermospheric neutral winds and the lower F-region ionosphere, but the initial results presented

here are very encouraging.

3.5 Conclusion

The recent installation of SuperDARN radars at mid-latitude reveals the presence of an evening enhancement in ground scatter characterized by (1) a higher signal to noise ratio around sunset, (2) a reduction of the ground scatter range from the radar, (3) occurrences on most geomagnetically quiet days from April to September. Modeling results from ray-tracing coupled with the IRI shows a very good correlation with observations, suggesting the enhancement is related to a well defined statistically significant ionospheric structure.

A single event was found providing joint observation of the ionosphere on a geomagnetically quiet day by both the Blackstone (37.10°N, 282.05°E) SuperDARN radar and the Millstone Hill Incoherent Scatter Radar (42.6°N, 288.5°E). On this event, a very good correlation appears between the ground scatter enhancement and electron density enhancement in the F-region over Millstone Hill. This correlation suggests that SuperDARN observations of a mid-latitude summer evening enhancement in ground scatter is most likely related to previous reports of a summer evening enhancement in electron densities over Millstone Hill. More joint observations with both SuperDARN mid-latitude radars and the Millstone Hill ISR could provide a good time resolution of the development of the evening enhancement, as well as a better understanding of the day-to-day variability of the enhancement and the role of neutral winds in its development.

Recent satellite observations reporting a globally structured evening enhancement in electron densities in the F-region during Northern hemisphere summers shows promising results and is most likely related to the enhancements observed by both SuperDARN and Millstone Hill. Global electron density maps generated using the IRI model exhibit a very good correlation with satellite observations of the evening enhancement and further verify that SuperDARN observations of the evening enhancement are related to the satellite observations of electron densities in the F-region. Additionally, results from the HWM07 model supports previous

studies that emphasized the importance of the neutral winds in generating the observed evening enhancement.

In this paper we report on the first observation of the evening enhancement by the new mid-latitude SuperDARN radars, and we are able to relate SuperDARN results to previous ISR and satellite observations. We also show that the evening enhancement is very well represented by the IRI model. Finally, results from the HWM07 model suggest that the seasonal variation of the evening enhancement is most likely related to the seasonal variation of thermospheric neutral winds combined with geomagnetic field configuration. Further investigation is needed to quantify the relative importance of the three currently identified factors of the evening enhancement: (1) thermospheric neutral winds, (2) the geomagnetic field configuration, and (3) polarization electric fields coupled with inter-hemispheric conjugacy. More information on the day-to-day variability and the longitudinal structure of the evening enhancement would be needed to establish a proper correlation with the three previously mentioned factors: the recent extension of the SuperDARN mid-latitude chain is expected to consolidate that information.

Chapter 4

Sub-Auroral Ionospheric Irregularities: observations and spatial distribution

Based on de Larquier, S., P. Ponomarenko, A. J. Ribeiro, J. M. Ruohoniemi, J. B. H. Baker, K. T. Sterne, and M. Lester (2013), On the spatial distribution of decameterscale subauroral ionospheric irregularities observed by SuperDARN radars, J. Geophys. Res. Space Physics, 118, doi:10.1002/jgra.50475.

The previous chapter has successfully applied HF propagation analysis to ground backscatter in order to understand a previously unexplained prominent feature in SuperDARN observations. In this chapter, we focus on ionospheric backscatter. This type of scatter requires a more nuanced approach. We study the spatial distribution of low-velocity Sub-Auroal Ionospheric Scatter (SAIS). The following aspects of low-velocity SAIS are analyzed in this chapter:

- azimuthal and range distributions: results from statistical distribution and ray-tracing reveal that the azimuthal distribution is entirely controlled by HF propagation factors, while the range distribution of SAIS is controlled by propagation at its closest edge, and vertical or horizontal ionospheric factors at its furthest edge.

- elevation angle data from the Blackstone interferometer combined with propagation considerations are used to derive altitude and ground range distributions of low-velocity SAIS, showing that the irregularities are observed between 200 and 300 km altitude.
- the range, azimuth and altitude distribution of low-velocity SAIS show that the ionospheric irregularities responsible for such scatter are widely distributed in the sub-auroral ionosphere, beyond the limits suggested by SuperDARN observations.

4.1 Introduction

The geomagnetic mid-latitude ionosphere is typically defined as a buffer zone between the equatorial and auroral regions, with boundaries that vary with geomagnetic activity. During quiet geomagnetic periods ($K_p < 2$), the mid-latitude ionosphere extends approximately from 30° to 60° geomagnetic latitude. The quiescent mid-latitude ionosphere is mainly controlled by photoionization and transport processes [*Heelis*, 2004] such as traveling ionospheric disturbances [e.g., *Tsugawa et al.*, 2007] and neutral winds [e.g., *Titheridge*, 1995]. External forcing by magnetospheric electric fields is largely absent from the quiescent mid-latitude ionosphere due to the effect of shielding in the Alfvén layers [e.g., *Kelley et al.*, 1979; *Huba et al.*, 2005].

The ionosphere is populated by plasma density irregularities. These irregularities result from plasma instabilities driven by combinations of plasma drifts, density and temperature gradients, electric fields and winds [e.g., *Fejer and Kelley*, 1980]. These plasma density fluctuations cover a wide range of scale sizes, spatial distributions and time scales. At mid-latitudes, both plasma and neutral processes are believed to be involved in generating and sustaining ionospheric irregularities. Processes such as the Perkins instability, the Kelvin-Helmholtz instability, and internal gravity waves have been cited to explain observations [e.g., *Kelley*, 2009, ch. 6]. These mechanisms lead to irregularities with scale sizes ranging from tens of

kilometers down to centimeters [e.g., *Tsunoda*, 1988].

Depending on their scale sizes, ionospheric irregularities can be observed by a variety of techniques, both ground- and space-based. For instance, GPS scintillation provides measurements of irregularities with scale sizes of hundreds of meters [e.g., *Fremouw et al.*, 1977]. Top-side sounders are also very common instruments observing meso-scale to large-scale ionospheric irregularities above 500 km altitude [e.g., *Su et al.*, 2006].

A conventional technique for studying decameter-scale irregularities is based on backscatter echoes observed by High Frequency (HF) radars [e.g., *Oksman et al.*, 1979]. The Super Dual Auroral Radar Network (SuperDARN) is a chain of HF radars covering mid and high-latitudes in both hemispheres. SuperDARN radars provide continuous observations of ionospheric dynamics [e.g., *Greenwald et al.*, 1995; *Chisham et al.*, 2007]. They operate at frequencies between 8-18 MHz, making them sensitive to backscatter from decameter-scale quasi-periodic structures. These quasi-periodic structures can be due to ionospheric plasma density irregularities in the E and F regions (responsible for ionospheric backscatter), or due to roughness at the Earth's surface (responsible for ground backscatter). Ground backscatter occurs after the HF signal from the radar is refracted by the ionosphere down to the ground.

In the case of ionospheric backscatter from the F-region, plasma density irregularities are typically highly aligned with the geomagnetic field lines due to the large difference in parallel and orthogonal ambipolar plasma diffusion coefficients [e.g., *Hysell et al.*, 1996]. Consequently, they are only observed when the incident HF wave vector is nearly perpendicular to the geomagnetic field lines, a criterion referred to as the aspect condition. When propagation conditions are conducive to observing ionospheric irregularities, SuperDARN radars can measure their drift velocities via Doppler shift of the backscattered signal. At high-latitudes, the drift velocities are on the order of hundreds to thousands of meters per second. The motion is caused mostly by $\mathbf{E} \times \mathbf{B}$ drift of the ionospheric plasma such that they can be used to infer electric fields and the large-scale plasma convection [e.g., *Ruo-*

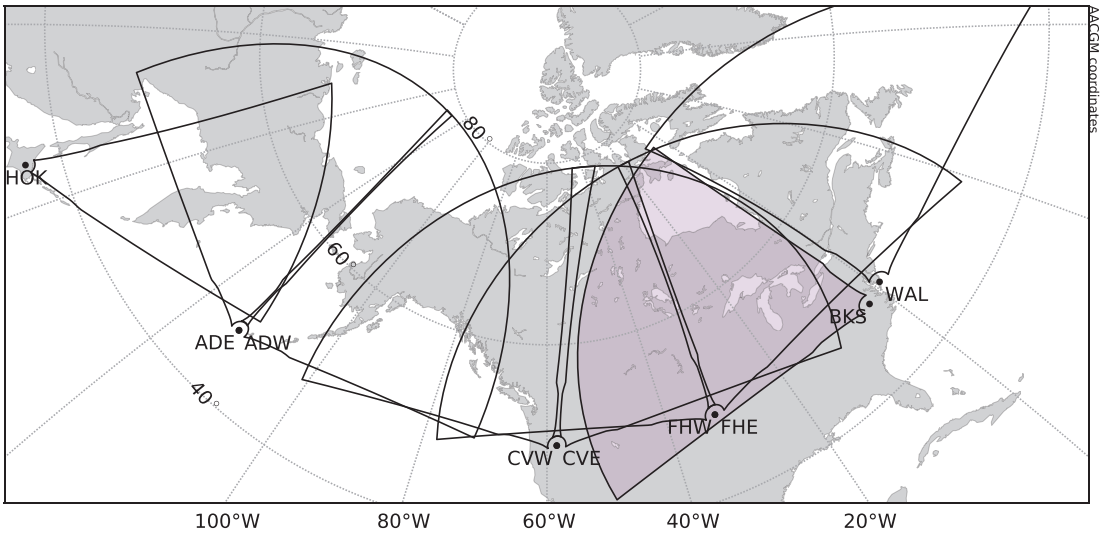

Figure 4.1. Mid-latitude SuperDARN radar coverage in the Northern hemisphere as of March 2013. The field-of-view of the Blackstone radar (BKS) is highlighted.

honiemi and Baker, 1998]. With the expansion of SuperDARN to mid-latitudes (see Figure 4.1), we have acquired new and dramatic views of such well-known sub-auroral disturbance phenomena as Sub Auroral Polarization Streams (SAPS) [e.g., *Oksavik et al.*, 2006; *Grocott et al.*, 2011; *Clausen et al.*, 2012; *Kunduri et al.*, 2012].

More surprisingly, the mid-latitude SuperDARN radars have revealed active irregularity formation during quiet geomagnetic periods [e.g., *Ribeiro et al.*, 2012; *Kane et al.*, 2012]. The backscatter associated with such irregularities has been termed Sub-Auroral Ionospheric Scatter (SAIS) [*Ribeiro et al.*, 2012]. *Greenwald et al.* [2006] reported recurring decameter-scale irregularities with low drift velocities (< 100 m/s) in the quiet-time mid-latitude nightside ionosphere observed with the first mid-latitude SuperDARN radar located at Wallops Flight Facility, Virginia. They suggested that the Temperature Gradient Instability (TGI) [*Hudson and Kelley*, 1976] could be responsible for generating such irregularities. The authors relied on co-located observations by the Millstone Hill Incoherent Scatter Radar (ISR) and the Wallops SuperDARN radar, which showed opposed temperature and density gradients, a geometry that yields a positive growth rate for the TGI. The opposed gradients were attributed to the ionospheric projection of

the plasmapause. However, a thorough statistical survey by *Ribeiro et al.* [2012] demonstrated that these irregularities are observed at latitudes far equatorward of auroral regions and the plasmapause projection. Using three years of data from the Blackstone SuperDARN radar, *Ribeiro et al.* [2012] showed that the low-velocity SAIS associated with these irregularities is confined to local night, and occurs on ∼70% of nights.

One important point of uncertainty in these studies arises from the difficulty in deriving precise SuperDARN backscatter geographical and altitude information. Because the ionosphere refracts HF signals, propagation does not follow a strictly line-of-sight path. The findings of *Greenwald et al.* [2006] relied on the conventional but unverified assumption that the observed irregularities are located in the F-region. Additionally, when studying the geographic distribution of HF ionospheric backscatter, corrections for propagation effects are rarely applied. Resolving the true altitude and geographic extent of ionospheric irregularities is crucial to inferring their potential sources.

The high occurrence rate and large geographical spread of these quiet-time mid-latitude irregularities make them an important, yet poorly understood, part of nighttime ionospheric dynamics. The purpose of this paper is to resolve the HF propagation effects in the observation of backscatter in order to determine the limiting factors in the horizontal and vertical extent of the irregularities. To achieve this objective, we rely on data from the Blackstone SuperDARN radar and apply ray-tracing analysis of HF propagation based on empirical models of the ionosphere and geomagnetic field. The findings from this study will serve as a necessary initial step towards resolving the mechanisms responsible for generating the observed quiet-time nightside mid-latitiude irregularities.

For this study, we combine the data analysis methods presented in Section 4.2.1 and ray-tracing model from Section 4.2.2 with the propagation concepts detailed in Section 4.2.3. In Section 4.3 the ray-tracing is compared with experimental scatter distributions in azimuth, range and elevation to analyze the importance of the spatial irregularity distribution and HF propagation in generating the observed

characteristics of low-velocity SAIS. We interpret the backscatter distributions in terms of the spatial distribution of ionospheric irregularities in Section 4.4.

4.2 Methods and tools

4.2.1 Data sets and analysis

SuperDARN radars consist of an electronically phased linear antenna array operated at frequencies between 8-18 MHz. A full field-of-view scan is completed every 1-2 min. Each scan is divided into 16 to 24 beams stepped in azimuth. Each beam is binned into 45 km slant-range gates: the slant-range represents time-of-flight (group range) of the backscattered signal with respect to the radar. In the case of HF propagation, the exact location of the scatterers is a complex function of the group range, altitude of the scatter and bending of the propagation path due to ionospheric refraction. Each slant-range gate stores a measure of the power, line-of-sight Doppler velocity, spectral-width and elevation angle of the backscatter. The position of the backscatter is estimated with a simple linear model which determines altitude and elevation as a function of slant-range to find ground projections. Geomagnetic coordinates of the backscatter projection are calculated with the AACGM model [*Baker and Wing*, 1989].

The Blackstone radar (37.10°N, -77.95°E) has been operating since February 2008. Its field-of-view provides good coverage of the mid-latitude ionosphere for magnetic invariant latitudes $\Lambda > 50°$. The Blackstone radar was chosen for this study over the Wallops radar used by *Greenwald et al.* [2006] because it is the only mid-latitude radar currently providing validated elevation angle measurements, which is an important parameter for analyzing HF propagation characteristics. The elevation angle is measured through the phase difference between the main antenna array and a secondary interferometer array located in front or behind the radar [*Milan et al.*, 1997b].

Figure 4.2 shows complete scans from the Blackstone (bks) and Wallops (wal) radars projected onto a geomagnetic coordinate system, as well as time-series of the

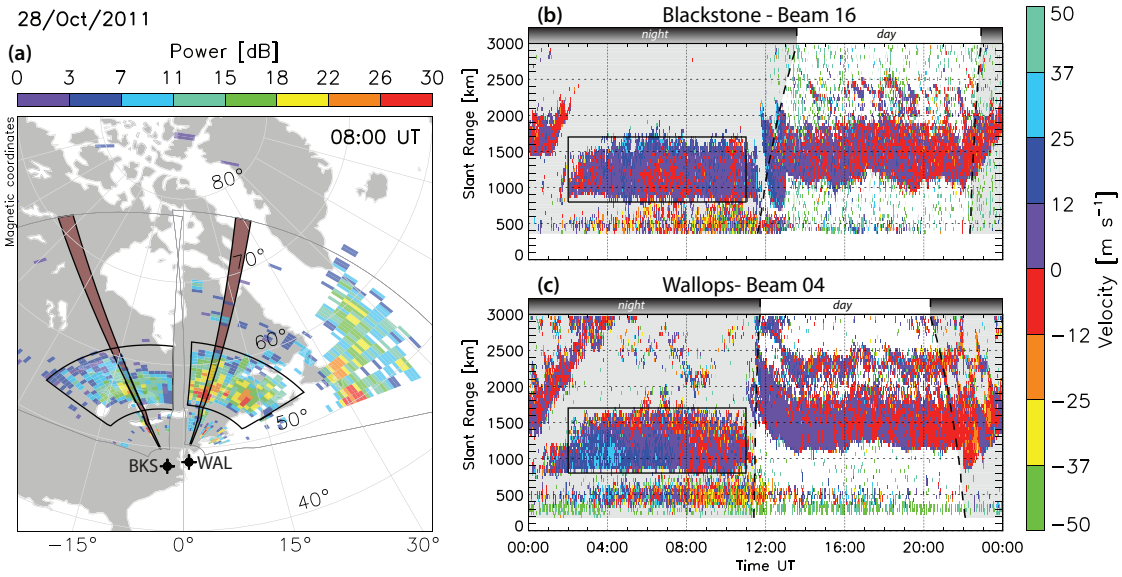

Figure 4.2. Sub auroral ionospheric scatter (boxed regions in all three panels) observed by the Blackstone (BKS) and Wallops (WAL) SuperDARN radars on October 28, 2011 during quiet geomagnetic time. **(a)** Backscatter power in the radars fields-of-view at 8:00 UT showing a wide band of ionospheric scatter (boxed regions). Beams 16 (-25.58°E) and 4 (58.35°E) of the Blacktsone and Wallops radars are highlighted in dark pink. **(b-c)** Range-time distribution of HF backscatter observed by (b) beam 16 of the Blackstone radar and (c) beam 4 of the Wallops radar, showing a typical time and range distribution of low-velocity SAIS (boxed regions). Nighttime is shaded in grey and bounded by dashed traces marking the day-night terminator.

slant-range distribution of the backscatter for selected beams. Figure 4.2a displays the backscatter power as a function of azimuth and range for a single scan at 8:00 UT on October 28, 2010. In Figure 4.2b-c, beams 16 and 4 of the Blackstone and Wallops radars are selected and the observed velocity distributions plotted versus time. Positive (negative) velocities indicate movement towards (away from) the radar. In all three panels, the occurrence of ionospheric backscatter is indicated by the boxed regions.

The time-series of Figure 4.2b-c show typical features observed by the mid-latitude SuperDARN radars during quiet periods. In both panels, the first patch of scatter at 00:00 UT, which starts at 1500 km slant-range and moves away from the radar as time passes, is ground scatter. Ground scatter is observed when the HF signals are reflected from the ionosphere down to the ground and part of the signal is scattered back to the radar along the same path by the rough ground surface. This type of scatter is prominent during the day, as seen in the large patch

of ground scatter between the day-night terminators (dashed traces marking the transition between shaded and non-shaded areas in Figure 4.2b-c). Note that the sudden jumps in slant-range of the observed scatter at 13 UT in Figure 4.2b and at 22 UT in Figure 4.2c are due to a change in operating frequency at the radars. During nighttime the ionosphere is dominated by recombination, which decreases electron densities and raises the ionosphere, resulting in the ground scatter moving further away from the radar. Most nights, electron densities are too low to reflect the HF signals to the ground, and ground scatter disappears. The activity is then dominated by ionospheric backscatter from geomagnetic-field-aligned density irregularities as seen in the boxed regions. There is also backscatter from meteor trails at closer ranges (< 500 km).

The occurrence of ionospheric backscatter depends both on the presence of decameter-scale irregularities and the angle between the HF wave vector and the background geomagnetic field lines in the vicinity of irregularities. The angle between the plane perpendicular to the magnetic field lines and the radar wave vector is referred to as aspect angle. There is a large body of work relating to auroral E-region aspect conditions reporting sensitivities from -10 to -15 dB/° [e.g., *Bates and Albee*, 1969; *Foster et al.*, 1992]. Few studies provide quantitative information on F-region aspect sensitivity. *Bates and Albee* [1970] estimated that most of the F-region aspect-sensitive echoes where observed within 5° of perpendicularity with the magnetic field. Their observations yielded an aspect sensitivity on the order of 5 dB/°. In this study, we will denote α as the complement of the aspect angle, and aspect conditions will be considered satisfied when $\alpha = 90 \pm 1°$.

In order to understand the influence of aspect and propagation conditions on low-velocity SAIS, we build statistical distributions of the scatter throughout the night. Low-velocity SAIS is identified using a method introduced by *Ribeiro et al.* [2011]. Once blocks of low-velocity SAIS are identified, the statistical backscatter distributions are built by counting scatter occurrence where the backscatter power is greater than 6 dB, in each gate-beam cell, during the 6 hours centered on local midnight. Each cell's slant-range, azimuth and elevation are recorded to build

distributions for all three of these parameters. The resulting distributions are normalized on the maximum scatter count for each night to remove daily variations in intensity. A scatter distribution value of 1 marks the region of highest scatter occurrence during a particular night, whereas a scatter distribution value of 0 means no scatter was observed.

Scatter distributions between November 2010 and May 2011 were searched for low-velocity SAIS. This period was selected specifically for the availability of calibrated elevation angle measurements. All events identified during this period have similar characteristics to those seen in Figure 4.2. Each event exhibits low-velocities (< 100 m/s), lasts for several hours, extends between 500 to 2000 km slant-range from the radar, and fades with increasing westward azimuth across the Blackstone field-of-view. For this study, we chose a representative day on November 18, 2010, when azimuth, range, elevation and time distributions are typical of low-velocity SAIS.

4.2.2 Ray tracing model

To properly interpret backscatter signatures in terms of ionospheric behavior, HF propagation in the ionosphere can be modeled using ray-tracing [e.g., *Hall et al.*, 1999]. The model employed in the present study relies on a two-dimensional (2-D) formulation of Fermat's principle in the propagation plane [*Coleman*, 1998]. The latest International Reference Ionosphere (IRI-2012) [e.g., *Bilitza and Reinisch*, 2008] and International Geomagnetic Reference Field (IGRF-11) are coupled with the ray-tracing. The IRI is used to compute the refractive index using the non-collisional transverse Appleton-Hartree formula as a function of electron density and signal frequency [*Davies*, 1990].

The ray-tracing equations are implemented in a 2-D simulation domain with origin at the center of the Earth and integrated using an adaptive step Runge-Kutta Cash-Karp numerical method [*Press et al.*, 2002]. The integration step is expressed in terms of group path length and is constrained between 1 m and 10 km for best performance/accuracy trade-off. A parallel version of the code is

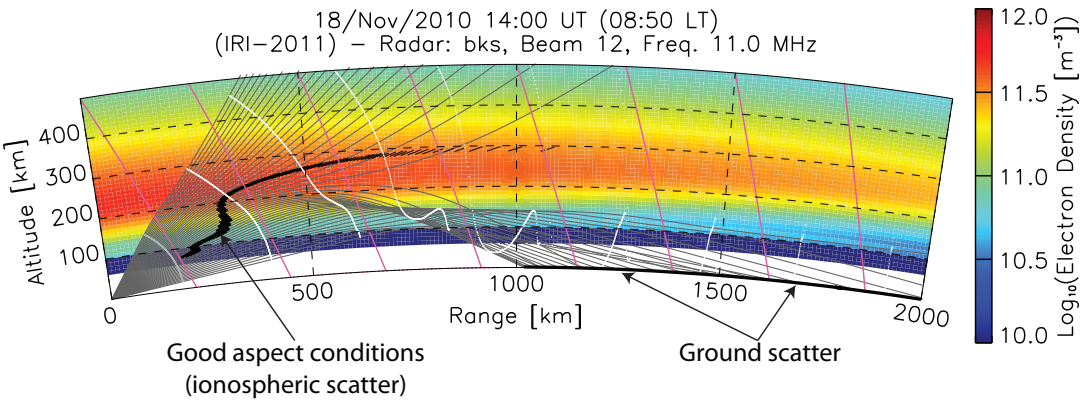

Figure 4.3. Ray-tracing results in an IRI generated ionosphere for beam 12 (-14.40°E) of the Blackstone radar on November 18, 2010 at 14:00 UT. Each ray is plotted in grey and the length of a ray-path to a scatter point is the slant-range. Black segments mark regions where rays are within one degree of orthogonality with the background geomagnetic field lines (pink lines). Rays reaching the ground between 1000 and 2000 km are responsible for ground scatter. The solid white traces serve as range markers: the first trace from the transmitter is at 180km, and all subsequent traces are 225 km apart.

implemented to allow for large statistical comparisons with SuperDARN observations and real-time online access for the SuperDARN user community (available at http://vt.superdarn.org/ray-tracing).

To simulate standard mid-latitude SuperDARN operations, rays are typically launched at all elevation angles between 5° and 55° in steps of 0.1°, at the selected azimuth and frequency. The range of elevation angles used in the model is chosen to include typical elevation angles measured at mid-latitudes. Each ray is examined for the occurrence of ionospheric or ground scatter. Figure 4.3 shows a typical example of HF propagation in the daytime mid-latitude ionosphere obtained with the ray-tracing code described above. The electron densities are color coded and show maximum values around 250 km altitude. Geomagnetic field lines, plotted in pink, indicate the geomagnetic aspect geometry. Rays themselves are plotted in gray and marked with white slant-range markers at 180 km first (range gate 0 at the radar), then every 225 km (5 range gates). It can be seen that with increasing elevation angle, rays reach higher altitudes and experience less refraction until they penetrate through the ionosphere. Lower angle rays are reflected to the ground where they are identified as ground scatter. Along each ray path, segments of good aspect conditions ($\alpha = 90 \pm 1°$) are shaded in black.

Figure 4.3 identifies two types of backscatter observed by SuperDARN radars, namely ionospheric and ground scatter. Each ray reaching the ground after reflection in the ionosphere is identified as ground backscatter, and the number of rays falling into each 45 km slant-range bin is counted. The count is then weighted by $1/r^3$, where r is the slant-range of a given bin (i.e., the length of a grey ray to the scatter point). The $1/r^3$ weight accounts for geometric power decay in the case where the ground acts as a backscatter target. In this case, the target's size increases linearly with range, thus compensating in part for the $1/r^4$ geometric power decay. Terrain geometry and reflective properties are ignored in this modeling approach.

Ionospheric scatter predictions are based on the relative orientation of the background magnetic field with each ray. For field-aligned ionospheric irregularities, maximum backscatter power is obtained when the radar wave vector $\mathbf{k}$ is nearly orthogonal to the geomagnetic field $\mathbf{B}$. The angle between $\mathbf{k}$ and $\mathbf{B}$ is the complement of the aspect-angle α and is calculated at each ray-path step: if α is within 1° of orthogonality, the current step is marked as potential ionospheric scatter, and the respective slant-range r and electron density N_e are stored. Each marked ray step is then weighted by N_e^2/r^3. This weight accounts for geometric power decay and spatial variation of irregularity intensity, which is assumed to be proportional to the squared background plasma density (see [*Ponomarenko et al.*, 2009]). The scaling of irregularity intensity as N_e^2 holds when the relative amplitude of density fluctuations is constant throughout the ionosphere. This modeling approach effectively assumes a uniform irregularity distribution. The resulting backscatter power for each 45 km slant-range bin is then calculated as a sum of the weighted powers for respective steps. With this approach to modeling ionospheric backscatter, if IRI provides a realistic ionosphere then the true irregularity distribution is the main source of differences between the modeled and observed distributions of ionospheric scatter.

The example presented in Figure 4.3 shows the regions where ground or ionospheric scatter have been identified. It should be noted that the locations of ground

and ionospheric scatter depend on ionospheric conditions, and one or both types of backscatter can completely disappear. Ray-tracing results such as that presented in Figure 4.3 can be processed into formats compatible with SuperDARN data, such as the field-of-view and range-time parameters plots discussed in Section 4.2.1 and shown in Figure 4.2.

4.2.3 Geometric parameters

In this section, we summarize the main parameters necessary to study HF propagation effects on ionospheric backscatter. The analysis of HF propagation requires a distinction between line-of-sight propagation and true propagation. Figure 4.4 illustrates this distinction, with the line-of-sight propagation following the red dashed line and the true propagation following the solid red curve. Both propagation paths start at O with an elevation angle δ. Both paths have the same time-of-flight Δt. The slant-range r is calculated as a function of the time-of-flight Δt and the speed of light in free space c as $r = c\Delta t$. In the ionosphere, the refractive index $\mu < 1$, such that the group velocity $v_g < c$: consequently the slant-range r (OX') is larger than the physical length of the path OX. The altitude of X' is called virtual altitude and is higher than the backscatter physical height at X. Note that for a planar ionosphere with only vertical variations, Breit and Tuve's theorem [e.g., *Davies*, 1990, ch. 6] yields that X and X' would be vertically aligned. Finally, the scatter occurs when the complement of the aspect angle α is within 1° of orthogonality: this aspect condition requires increased angle of refraction (i.e., bending of the path), hence a lowering of X, as the magnetic field $\mathbf{B}$ gets closer to vertical.

The concepts summarized in this section provide a framework for the propagation analysis presented next.

4.3 Results

In this section we present the main characteristics of observed and modeled backscatter distributions for November 18, 2010. Recall that this day has been picked for

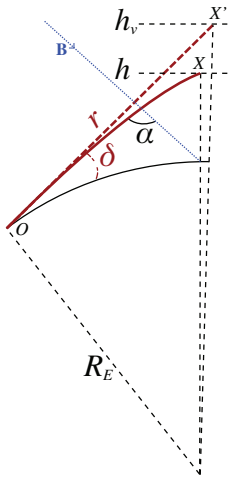

Figure 4.4. Ray propagation geometry. The red traces show propagation path, where the solid curve is a realistic path and the dashed line is the line-of-sight path. h and h_v are the physical and virtual altitudes respectively, α is the aspect-angle, δ is the elevation angle, and r is the slant-range along the propagation path; R_E is the radius of the Earth and **B** is the geomagnetic field.

having azimuth, range, elevation and time distributions typical of low-velocity SAIS. We will interpret the backscatter distributions in terms of the distribution of ionospheric irregularities in Section 4.4.

4.3.1 Azimuth distribution

The example of low-velocity SAIS presented in Figure 4.2a shows most of the scatter located near the center of the combined fields-of-view of the two radars. The observed backscatter distribution across all 16 beams of the Blackstone radar during 6 hours on the night of November 18, 2010 is shown in Figure 4.5a, next to the model distribution obtained using the ray-tracing results (Figure 4.5b). The observed distribution in Figure 4.5a is scaled with iso-contours that are also overlaid on Figure 4.5b for reference. The experimental data show a marked offset towards the rightmost beams, a feature also seen in the model results (see Figure 4.5b). The region where scatter occurrence is greater than 0.5 of its maximum is located between beams 7 and 15 (-34.10° and -1.96°). This distribution bias can be interpreted either in terms of irregularity distribution or in terms of HF propagation.

We use the model results from the ray-tracing to analyze the relative influence of

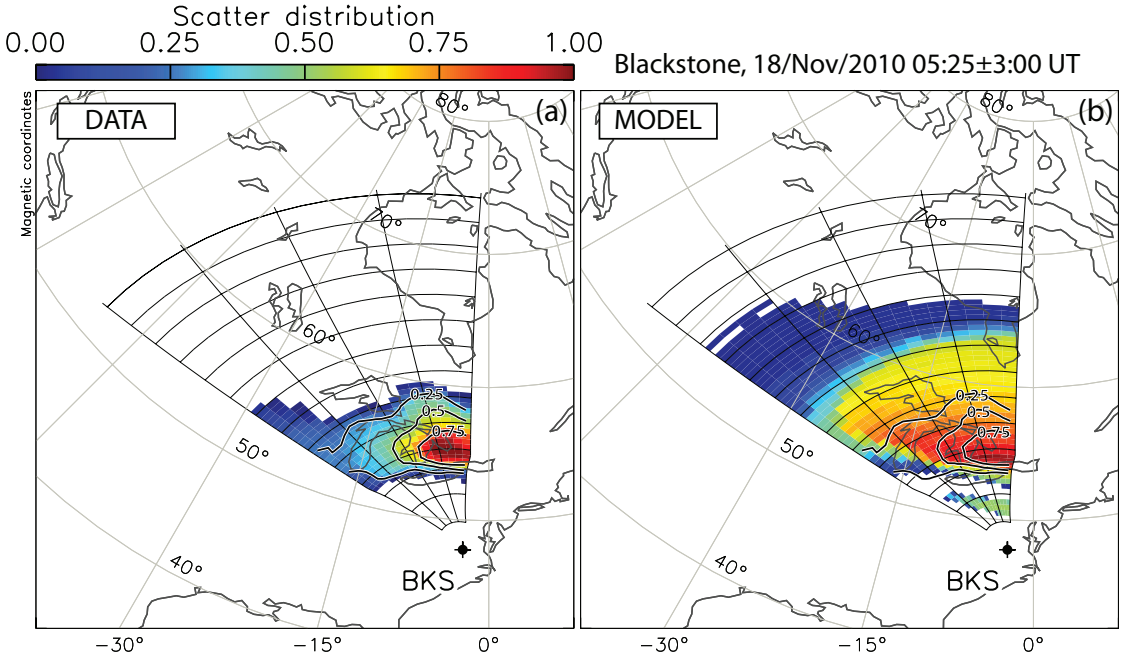

Figure 4.5. Azimuth distribution of low-velocity SAIS in the Blackstone SuperDARN radar field-of-view during six hours centered around local midnight on November 18, 2010. The field-of-view begins 180 km (slant-range) away from the radar and is gridded every 5 slant-range gates (225 km) and 4 beams (12.96 degrees), from beam 0 (westernmost) to beam 15 (easternmost). On both panels, contours of the radar data distribution at 0.25, 0.5 and 0.75 have been overlaid (solid thick black lines). **(a)** Radar observations. **(b)** Ray tracing results. The color bar applies to both panels a and b.

both effects on the scatter azimuth distribution. The model propagation characteristics depend on IRI generated electron densities and IGRF modeled geomagnetic field geometry. Note that the simulated distribution (Figure 4.5b) exhibits less dramatic azimuthal variations than the observed data distribution (Figure 4.5a). However, in both cases, the location of maximum scatter occurrence is between beams 7 and 15 (-34.10° and -1.96°) at approximately 900 km slant-range.

4.3.2 Slant-range distribution

Figure 4.5 is also key to revealing and understanding the range distribution. From Figure 4.2b-c it appears that, within a given beam, low-velocity SAIS occupies a quasi-constant slant-range band from 800 to 1600 km. In Figure 4.5a, the contour region where the scatter occurrence is greater than 0.25 of its maximum value suggests that the range extent narrows toward the leftmost beams. Figure 4.5b captures a similar narrowing of the range distribution for scatter occurrences

greater than 0.25. However, in the region of low scatter occurrence (< 0.25) this slant-range narrowing is absent from both the data and simulated distributions.

The simulated distribution shown in Figure 4.5b suggests that in an ionosphere uniformly populated with irregularities scatter could occur at further ranges than observed in Figure 4.5a. Note that ray-tracing results in Figure 4.5b exhibit an additional region of scatter closer to the radar and detached from the main scatter patch. This closer scatter patch corresponds to potential scatter from E-region irregularities ($\sim$110 km altitude). Its absence in the observational data despite favorable propagation conditions indicates the absence of irregularities in the E-region. Note that this patch of predicted E-region scatter is reproduced in all subsequent distributions presented in this study. In our analysis, we focus on the region where the relative scatter occurrence is greater than 25%. Both data and model results show almost identical positions of the leading slant-range edge of the scatter distribution, following the closest contour line, starting at $\sim$600 km in the rightmost beam (beam 15, -1.96°E) to 900 km in the leftmost beam (beam 0, -59.28°E). However, the trailing edge of the modeled distribution appears much further at $\sim$2000 km than observed in the data at $\sim$1300 km.

It is important to note that although we are showing the slant-range distribution in a geomagnetic coordinate system projected on the surface of the Earth, slant-range limits depend on both the horizontal and vertical distance traveled by the transmitted signal.

4.3.3 Elevation distribution

Conventional SuperDARN software does not permit to estimate the altitude of the scatter. Instead, a simplistic model is used to determine geographical coordinates of the scatter footprint [*Chisham et al.*, 2008], which can produce a large uncertainty at ranges exceeding 1000 km [*Yeoman et al.*, 2008]. Potentially, a combination of elevation angle data and ray-tracing can provide more accurate information on the actual location of the effective scattering volume.

Figure 4.6 shows the elevation angle distribution as a function of slant-range

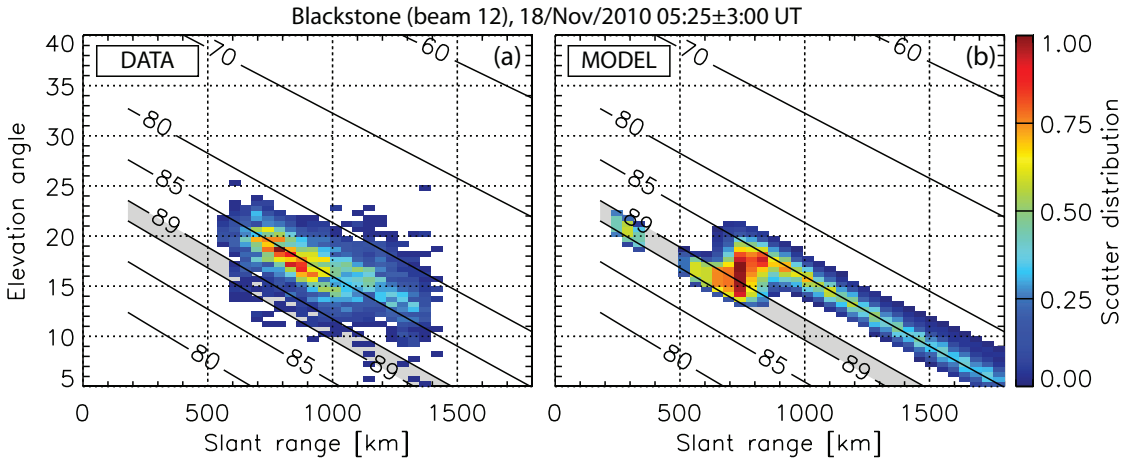

Figure 4.6. Elevation angle distribution of low-velocity SAIS as a function of slant-range in beam 12 of the Blackstone SuperDARN radar during six hours centered around local midnight on November 18, 2010. Contours of the angle between the radar wave vector and the background geomagnetic field are calculated for line-of-sight propagation and overlaid. **(a)** Radar observations. **(b)** Ray tracing results. The color bar applies to both panels a and b.

in the case of observed (Figure 4.6a) and modeled (Figure 4.6b) scatter for beam 12 (-14.40°E) of the Blackstone radar during the selected 6 hours of the night of November 18, 2010. Beam 12 was selected for being at the center of the highest scatter occurrence region in Figure 4.5. Notice that, to first order, the observed and modeled distributions are very similar. In the simulated distribution of Figure 4.6b, as in Figure 4.5b, we note a patch of predicted E-region scatter at closer ranges (200-400 km) and the absence of such scatter in the observations. To estimate the amount of refraction (i.e., bending of the rays) and the aspect sensitivity, aspect-angle contours for the case of straight-line propagation are overlaid on both data and model distributions. If the propagation were truly line-of-sight, the observed scatter would be expected to lie close to the $\alpha = 90°$ contour line, between the $\alpha = 89°$ contours (see section 4.2.2).

The most significant difference between Figures 4.6a and 4.6b occurs near 700 km slant-range. There, the model predicts a wide range of elevation angles where SAIS could be observed. However, the data only shows scatter in the upper portion of these elevation angles. Since increasing elevation angles at a fixed slant-range are associated with increasing altitudes, this difference suggests a lower bound to the irregularities' vertical extent.

In Figure 4.6a-b the scatter at slant-ranges greater than 700 km is aligned with the $\alpha = 85°$ isoclines. This implies a $\sim$4-5° elevation angle deviation from straight-line. At closer slant-ranges (500-700 km), scatter predicted by the ray-tracing (Figure 4.6b) gets closer to the line-of-sight direction. In both modeled and observed scatter distributions, most of the scatter (> 0.5) is observed with elevation angles ranging from 15° to 20°, and with slant-ranges between 700-1000 km. We consider that the high degree of similarity between these distributions indicate that the model realistically reflects actual propagation conditions.

We also consider the width of the scatter distribution along the elevation axis. We restrict our analysis to the part of the distribution where scatter occurrence is greater than 50% of its maximum value (> 0.5) in order to maximize the statistical significance of the backscatter elevation. With this constraint, the width of the elevation distribution is close to the angular distance between the $\alpha = 89°$ isoclines. This means that for the scatter considered here, the 1° ad-hoc aspect sensitivity condition appears to be valid.

Elevation, angle of refraction, and slant-range can be combined to estimate altitude and ground-range distributions of the observed low-velocity SAIS. A zeroth order estimate for the center of the scatter distribution at 800 km slant-range and 18° elevation yields a physical altitude $h \simeq 240$ km. This indicates that the assumption by *Greenwald et al.* [2006] that SAIS originates from the ionospheric F-region was correct.

4.4 Discussion

We analyze the azimuth, slant-range and elevation distributions of low-velocity ionospheric backscatter at mid-latitudes presented in Section 4.3 to decouple HF propagation effects from the observations and so deduce information on the spatial distribution of the ionospheric irregularities. The multiple similarities and few differences between the observed and modeled distributions are key to this discussion.

4.4.1 IRI effects on modeled HF propagation at mid-latitude

The modeling results rely on the IRI to predict scatter distributions. Consequently, the IRI is an important factor influencing the comparison between the modeled and observed distributions presented in Figure 4.5 and 4.6. Previous comparison between mid-latitude SuperDARN data and IRI-based ray-tracing during quiet geomagnetic periods has shown good correlation for ground scatter events [*de Larquier et al.*, 2011].

The case of ionospheric scatter is more complex as the ray-tracing model assumes uniform distribution of ionospheric irregularities so that it can only predict potential scatter distributions, but cannot account for the presence or absence of irregularities required to observe ionospheric scatter. The IRI is used to determine the amount of vertical refraction a ray-path experiences, thus determining the region where the ray can satisfy aspect conditions ($\alpha = 90 \pm 1°$) so that irregularities can be observed. We investigated the sensitivity of the modeled spatial distributions of the backscatter to 20% variations in IRI maximum height and electron density of F2 layer. We observed only $\sim 10\%$ variations in the effective altitude and ground range of the scatter maximum occurrence. This means that the modeled ionospheric scatter distributions are only marginally affected by the intrinsic uncertainties of the IRI model.

This is not unexpected because the quiet-time mid-latitude ionosphere is an ideal candidate for empirical models such as IRI. The high adequacy of IRI under the conditions of interest to this study imply that differences between modeled and observed backscatter distributions provide meaningful information about the distribution of irregularity.

4.4.2 Irregularities altitude range

An important yet elusive parameter in HF observations is the altitude of the backscattering irregularities. Studies based on SuperDARN observations generally use a simple stepped linear model depending on slant-range only [*Chisham et al.*, 2008]. More accurate models have also been used to estimate backscatter

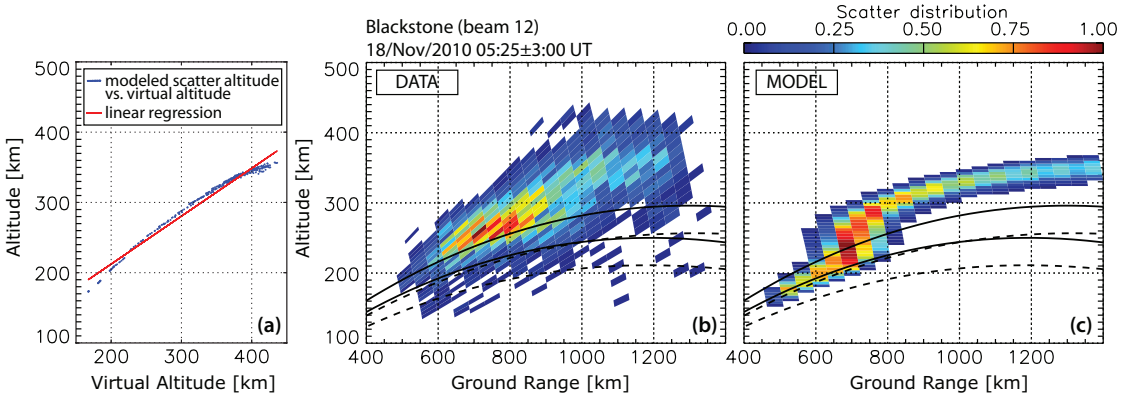

Figure 4.7. Altitude distributions for the Blackstone SuperDARN radar during six hours centered around local midnight on November 18, 2010. Physical altitude of the observed backscatter (data) is calculated from slant-range, virtual height, and a linear coefficient derived from model results as shown in panel (a). The two solid curves and two dashed curves in panels (b) and (c) mark the regions where the complementary of the aspect-angle $\alpha = 90 \pm 1^\circ$ for beam 12 (solid) and beam 0 (dashed), respectively. **(a)** Altitude versus virtual altitude of the modeled scatter distribution (blue dots) used to estimate the linear transformation between altitude and virtual altitude (red line). **(b)** Radar observations. **(c)** Ray tracing results.

altitude [e.g., *Chisham et al.*, 2008; *Liu et al.*, 2012]. If accurate elevation angle measurements are available, then the virtual altitude h_v (see Figure 4.4) can be calculated. However, the actual altitude depends on the amount of vertical refraction.

In the case of low-velocity SAIS, we benefit from a relatively quiet and weak background ionosphere. Figure 4.6 shows that the modeled scatter follows the same isocline (85°) as the observed scatter at slant-ranges 700-1400 km. This suggests that the ray-tracing adequately reproduces vertical refraction, such that it can provide a reliable estimate of the observed scatter altitude. Furthermore, the deviation from line-of-sight appears to be small ($< 0.5^\circ/100$ km), indicating minimal refraction. In this case the relation between virtual altitude h_v and physical altitude h can be approximated as a linear function of slant-range r such as $h = h_v - \gamma r$, where γ is a dimensionless constant expressing the bending of the ray-paths during the night of November 18, 2010. The coefficient γ is calculated from the known virtual and physical height of the modeled scatter distributions. Figure 4.7a shows the physical versus virtual altitude of the modeled scatter (blue markers), as well as the result of a linear regression through these points (red line).

The slope of the linear regression is the coefficient γ.

The result of this transformation from elevation to physical altitude of observed SAIS is presented in Figure 4.7b. For consistency, the ray-tracing altitude distribution shown in Figure 4.7c is obtained with the same transformation rather than directly from the modeled altitude. On the same graphs we plot the $\alpha = 89°$ isoclines for line-of-sight propagation for beams 12 (solid curves) and 0 (dashed curves). Most of the scatter is observed between 220 and 320 km altitude, typically corresponding to the nighttime bottom-side F-region ionosphere (on the night considered here, IRI places the F-region peak at 340 km). Note also that the model predicts favorable propagation conditions at E-region altitudes but experimentally no scatter is observed, indicating the absence of E-region irregularities. To our knowledge, this is the first experimental estimation of the height of low-velocity SAIS.

It is worth noting that the bottom side F-region is characterized by a strong vertical electron density gradient. Moreover, at mid-latitudes, this gradient has a significant component in the direction perpendicular to the geomagnetic field. Electron density or temperature gradients perpendicular to the magnetic field are an important aspect of several plasma instabilities, [*Hudson and Kelley*, 1976], such as the TGI or Gradient Drift Instability (GDI) [*Baker et al.*, 1986]. The confinement of the observed backscatter to the bottom-side F-region may therefore indicate that the irregularities are produced by one of the above instabilities.

4.4.3 Horizontal extent of irregularities

We now consider the horizontal extent of the irregularities implied by the azimuth and slant-range backscatter distributions. Several previous studies analyzed statistical distributions of irregularities at high and mid-latitudes during moderate to active geomagnetic periods [e.g., *Hosokawa et al.*, 2002; *Hughes et al.*, 2002; *Parkinson et al.*, 2002; *Nishitani and Ogawa*, 2005; *Kane et al.*, 2012]. However, none of them have focussed specifically on low-velocity SAIS and the distinctive features of the backscatter distribution within the radar fields-of-view.

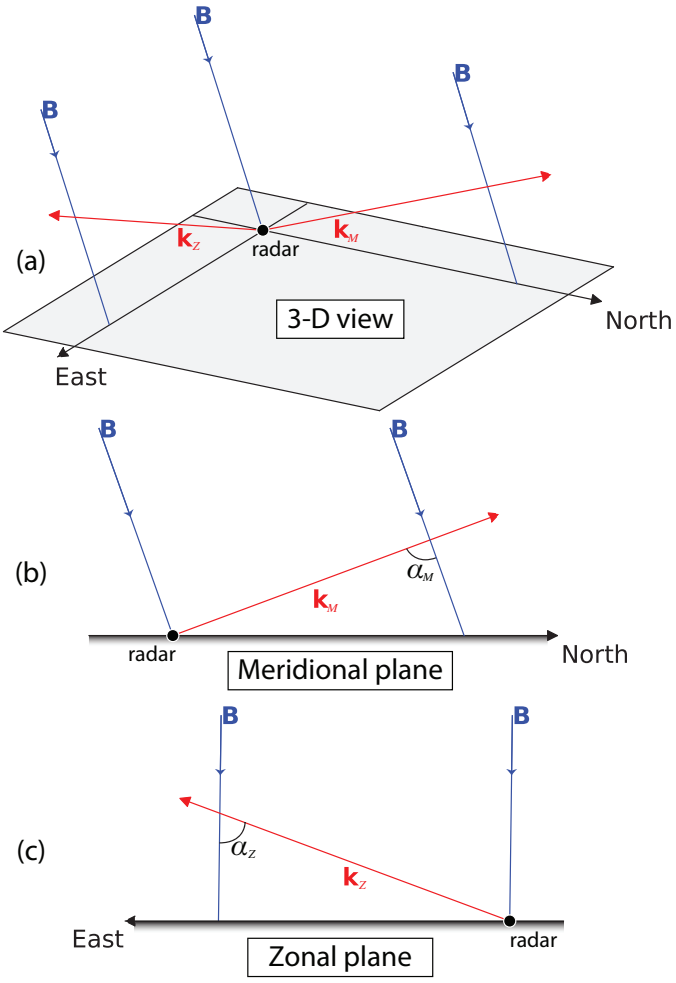

Figure 4.8. Idealized illustration of the effect of propagation azimuth on aspect geometry at sub-auroral latitudes for a flat Earth. $\mathbf{k}_M$ and $\mathbf{k}_Z$ denote the wave vector in the merdional and zonal directions, respectively. **B** is the geomagnetic field with a fixed dip angle representative of the Blackstone SuperDARN radar. North and East are indicated with respect to geomagnetic North. **(a)** 3-D view. **(b)** 2-D side view along a meridional beam. **(c)** 2-D side view along a zonal beam. α_M is closer to 90° than α_Z, indicating that a lower elevation angle or increased refraction is required in the zonal plane to achieve good aspect conditions.

The most prominent feature, captured in both data and model, is the azimuthal bias (see Figure 4.5). To assist our discussion, the azimuths with respect to geomagnetic North for the extreme beams of the Blackstone and Wallops radars are presented in Table 4.1. From this table, it is apparent that the scatter is concentrated in the meridional beams. This still does not preclude the possibility that irregularities are simply confined to this particular region. However, similar low-velocity SAIS is observed with other SuperDARN radars, with the same bias

towards the most meridional beams (not shown).

Radar	First beam	Last beam	Beam separation
bks	-59.28°E	-1.96°E	3.86°
wal	-1.36°E	84.35°E	3.24°

Table 4.1. Beam-azimuth conversion with respect to geomagnetic North for the Blackstone and Wallops SuperDARN radars. Note that beams are always numbered from West to East.

This bias can be consistently explained in terms of propagation geometry. To visualize this geometry, Figure 4.8 represents the idealized situation at the Blackstone radar, where the average magnetic field dip angle is 70°, two beams are looking North and East with an elevation angle of 20°, and the Earth is flat. Figure 4.8a shows a three-dimensional view of the two signals propagating in a straight line (i.e., no refraction), one northward along a magnetic meridian, and the other eastward perpendicularly to the same meridian. Figure 4.8b shows that in the meridional direction, the wave vector achieves perpendicularity with a geomagnetic field line without refraction at some altitude, thus satisfying aspect conditions and allowing irregularities to be observed. However, Figure 4.8c shows that the wave vector in the zonal direction is further away from good aspect conditions at the same altitude, and requires either increased refraction or a lower elevation angle to achieve perpendicularity. Consequently, under fixed ionospheric conditions (constant refraction) moving the propagation direction away from the magnetic meridian shifts aspect-friendly areas to further ranges and lower altitudes. As a result, under quiet nighttime conditions characterized by weak refraction, off-meridional beams should see ionospheric scatter moving further away from the radar with reduced occurrence, as observed in Figure 4.5.

Further illustration of this propagation effect is given in Figure 4.7. The solid and dashed contours mark regions of good line-of-sight aspect conditions for a mostly meridional beam (beam 12) and the most zonal beam (beam 0), respectively. For the zonal beam, the region of good aspect conditions occurs at lower altitudes than for the meridional beam. Under uniform ionospheric conditions within the radar field-of-view, these line-of-sight contours reflect the relative position of good aspect condition regions of a meridional and zonal beam. Thus, zonal

beams are constrained to lower altitudes than meridional beams. Since scatter occurrence declines sharply with beam direction moving away from magnetic North, one can assume that the irregularities are confined to the F-layer and disappear at lower altitudes. This result points to the effect of HF propagation on the observable region of irregularities. An important implication is that the backscattering irregularities likely extend beyond the azimuth limits of the observed scatter, covering a much larger longitude swath of the mid-latitude ionosphere than suggested by the apparent azimuthal distribution in the radar data.

The propagation constraints on the altitude and range of good aspect conditions also explains why the leading edge of the modeled and observed scatter shown in Figure 4.5a-b match very well. As the radar scans towards off-meridional beams, aspect conditions are lowered and pushed further in range, which describes the slanted leading edge of the scatter distribution across the field-of-view. However, the mismatch in the trailing edge between the model and data distributions remains unexplained, and could be interpreted either as a horizontal or vertical limit on the spatial extent of irregularities. This information would provide valuable insight into the underlying plasma instabilities, such as the relative importance of vertical and horizontal gradients or the identification of a source region. According to Figure 4.7c, for a given beam direction, increasing ground range leads to increasing height with favorable aspect conditions. Additionally, the furthest distribution contour in Figure 4.5a appears to follow a constant slant-range line rather than a constant geomagnetic latitude. These observations argue that the range limit to the observed scatter distribution is likely due to the absence of irregularities at altitudes exceeding the F-region peak.

The high similarity between experimental and modeled spatial distributions of the HF backscatter argues that the observability of the nighttime echoes is subject to aspect-angle restrictions. The matching close-range and off-meridional limits suggest that the actual horizontal extent of the ionospheric irregularities spreads well beyond the field-of-view of the radar. Additionally, the boundary mismatch at the far ranges points at a limited vertical extent of the scatterers, which seems

to be confined to the bottom part of the F region. These results combined with the results from *Ribeiro et al.* [2012] provide a full description of the spatial and temporal characteristics of nightside quiescent mid-latitude irregularities.

4.5 Summary

In this paper we have analyzed the spatial distributions of low-velocity Sub-Auroral Ionospheric Scatter (SAIS) and their implications for understanding a prominent type of quiet-time sub-auroral irregularities. The occurrence of such scatter shows a bias towards meridional beam directions. It also shows reduced slant-range at the leading edge of the scatter for the most meridional beams, but quasi-constant slant-range for the trailing edge of the scatter across all beams. We have demonstrated that the limited spatial extent of this category of ionospheric backscatter within SuperDARN fields-of-view is a consequence of HF propagation and the finite extent of irregularity altitude. We were able to show that the observed backscatter distributions from the decameter-scale ionospheric irregularities in the mid-latitude ionosphere are consistent with a 1° aspect sensitivity. Propagation effects were shown to control the altitude and range extents of the irregularities visible to the SuperDARN radars. This indicates that the irregularities extend over wide regions of the mid-latitude ionosphere, but their appearance within radars fields-of-view is constrained by propagation geometry. Backscatter also seems to be constrained by the finite vertical extent of the irregularities. For the first time, the altitudes of the sub-auroral ionospheric irregularities is estimated to extend between 200-300 km, which agrees with previous assumptions about SAIS. Conclusions presented in this paper further reinforce the prominence of such irregularities, both temporally due to their high occurrence rate and durations, and spatially as evidenced in this study. These findings clarify our understanding of the nature of plasma instability responsible for the observed irregularities. Instruments such as ISRs or in-situ rocket measurements could be used to obtain simultaneous complementary plasma diagnostics.

Chapter 5

Sub-Auroral Ionospheric Irregularities: Plasma Environment and Instability Mechanism

Based on S. de Larquier, A. Eltrass, A. Mahmoudian, J. M. Ruohoniemi, J. B. H. Baker, W. A. Scales, P. J. Erickson, and R. A. Greenwald (2013), Investigation of the Temperature Gradient Instability as the Source of Mid-Latitude Quiet-Time Decameter-Scale Ionospheric Irregularities: Part 1, Observations, Submitted to J. Geophys. Res. Space Physics.

The previous chapter provides a clear representation of the spatial occurrence of ionospheric irregularities responsible for low-velocity Sub-Auroral Ionospheric Scatter (SAIS). In this chapter, we leverage this new information in conjunction with previous studies of low-velocity SAIS to evaluate the role of the Temperature Gradient Instability in the growth of the observed irregularities.

5.1 Introduction

The mid-latitude ionosphere (between 30° and 60° geomagnetic latitude) is a largely quiescent plasma, particularly during periods of low geomagnetic activity ($K_p \leq 2$). Yet, even under such conditions, the mid-latitude ionosphere is

populated by plasma density irregularities. These irregularities result from plasma instabilities driven by combinations of plasma drifts, density and temperature gradients, electric fields and winds [e.g., *Fejer and Kelley*, 1980]. Both plasma and neutral processes are believed to be involved in generating and sustaining the ionospheric irregularities. Processes such as the Perkins instability, the Kelvin-Helmholtz instability, and internal gravity waves have been cited to explain observations of ionospheric irregularities [e.g., *Kelley*, 2009, ch. 6]. These mechanisms lead to irregularities with scale sizes ranging from tens of kilometers down to centimeters [e.g., *Tsunoda*, 1988].

Depending on their scale sizes, ionospheric irregularities can be observed by a variety of techniques, both ground- and space-based. For instance, GPS scintillation provides measurements of irregularities with scale sizes of hundreds of meters [e.g., *Fremouw et al.*, 1977]. Top-side sounders commonly observe meso-scale (50-1000 km) to large-scale ionospheric (>1000 km) irregularities above 500 km altitude [e.g., *Su et al.*, 2006].

High Frequency (HF) radars observe coherent backscatter echoes from ionospheric density perturbations with scale lengths on the order of ten meters [e.g., *Oksman et al.*, 1979]. The Super Dual Auroral Radar Network (SuperDARN) is a chain of HF radars covering mid- and high-latitudes in both hemispheres, that provides continuous observations of the ionosphere, including the occurrence of decameter-scale ionospheric irregularities [e.g., *Greenwald et al.*, 1995; *Chisham et al.*, 2007]. These irregularities are often simply used as tracers to image plasma flow in the ionosphere [e.g. *Frissell et al.*, 2011; *Kunduri et al.*, 2012; *Thomas et al.*, 2013].

Greenwald et al. [2006], following the construction of the first mid-latitude SuperDARN radar in Wallops Island, Virginia (WAL), reported the common occurrence of backscatter from mid-latitude irregularities during low geomagnetic activity. *Ribeiro et al.* [2012] showed that such irregularities could also be observed with a second mid-latitude SuperDARN radar located at Blackstone, Virginia. They established that such irregularities were only seen at night and remained equator-

ward of both the auroral region and the ionospheric projection of the plasmapause. *de Larquier et al.* [2013a] demonstrated that this type of ionospheric irregularity is widely distributed horizontally within the mid-latitude ionosphere, populates the bottom side F-region (200-300 km altitude), and is highly field aligned. One question which remains unanswered is the identity of the plasma instability mechanism that is responsible for the growth of these quiet-time sub-auroral decameter-scale irregularities.

Only recently have the spatial and temporal characteristics of these irregularities been established, and it is timely for us to re-investigate previous experiments to understand the ionospheric conditions during such events. *Greenwald et al.* [2006] presented electron density and temperature measurements from the Millstone Hill Incoherent Scatter Radar (MHO) within the region of ionospheric irregularities observed by WAL. Their analysis led them to suggest that the Temperature Gradient Instability (TGI) [*Hudson and Kelley*, 1976] could be responsible for generating the irregularities. This conclusion was reached due to the presence of opposing horizontal electron temperature and density gradients at 300 km altitude. However, this approach neglected to consider the fact that the electron temperature and density gradients driving the TGI should be perpendicular to the geomagnetic field $\mathbf{B}$, which has a dip angle of $\sim 70^{\circ}$ in the observation region. Additionally, only three of the five hours during which irregularities were observed exhibited favorable growth conditions for the TGI, further casting doubt on the role of the TGI in causing the observed irregularities.

In this paper, we present a new approach to the analysis of TGI growth conditions during this event. Using the Millstone Hill and SuperDARN data presented by *Greenwald et al.* [2006], we re-derive the electron density and temperature gradients in the plane perpendicular to $\mathbf{B}$ (hereafter referred to as *perpendicular gradients*). We use these new gradients to re-evaluate the role of the TGI in generating the observed irregularities. In a companion paper [*Eltrass et al.*, this issue], the TGI growth rate for this event is computed using a kinetic model and compared to another common instability mechanism, the Gradient Drift Instability (GDI).

In section 5.2 of this paper, we introduce the SuperDARN and Millstone Hill observations. In section 5.3, the electron density and temperature gradients are derived in different ionospheric regions and along different directions relevant to the observed irregularities. The implications of the direction and amplitude of these gradients for the role of the TGI in the growth of irregularities observed by mid-latitude SuperDARN radars are discussed in section 5.4.

5.2 Observations

The observations from the night of February 22-23, 2006 used in this study were originally introduced by *Greenwald et al.* [2006]. In this section, we provide a brief description of these observations.

5.2.1 SuperDARN observations

SuperDARN radars consist of an electronically phased linear antenna array operated at frequencies between 8-18 MHz. During the night of February 22-23, 2006, the Wallops Island SuperDARN radar (WAL: 37.93°N, -75.47°E) was operating in its standard 16-position azimuth-scanning mode, dwelling for 3 seconds in each azimuth direction, and starting a new azimuth scan every 60 seconds. Each beam is divided into 45 km slant-range gates (where slant-range represents time-of-flight of the backscattered signal with respect to the radar) extending from 180 km to over 4000 km. Each slant-range gate stores a measure of the power, line-of-sight Doppler velocity, spectral-width and elevation angle of the backscatter. The geographic positions of the backscatter echoes are estimated with a simple linear model which determines altitude and elevation as a function of slant-range [*Chisham et al.*, 2008]. Geomagnetic coordinates of the backscatter positions are calculated using the Altitude Adjusted Corrected GeoMagnetic (AACGM) coordinate system [*Baker and Wing*, 1989].

Figure 5.1 shows the backscatter power and line-of-sight Doppler velocity observed by the Wallops Island radar on the night of February 22-23, 2006. Panels a and b show backscattered power across the Wallops field-of-view at 01:00 and 03:00

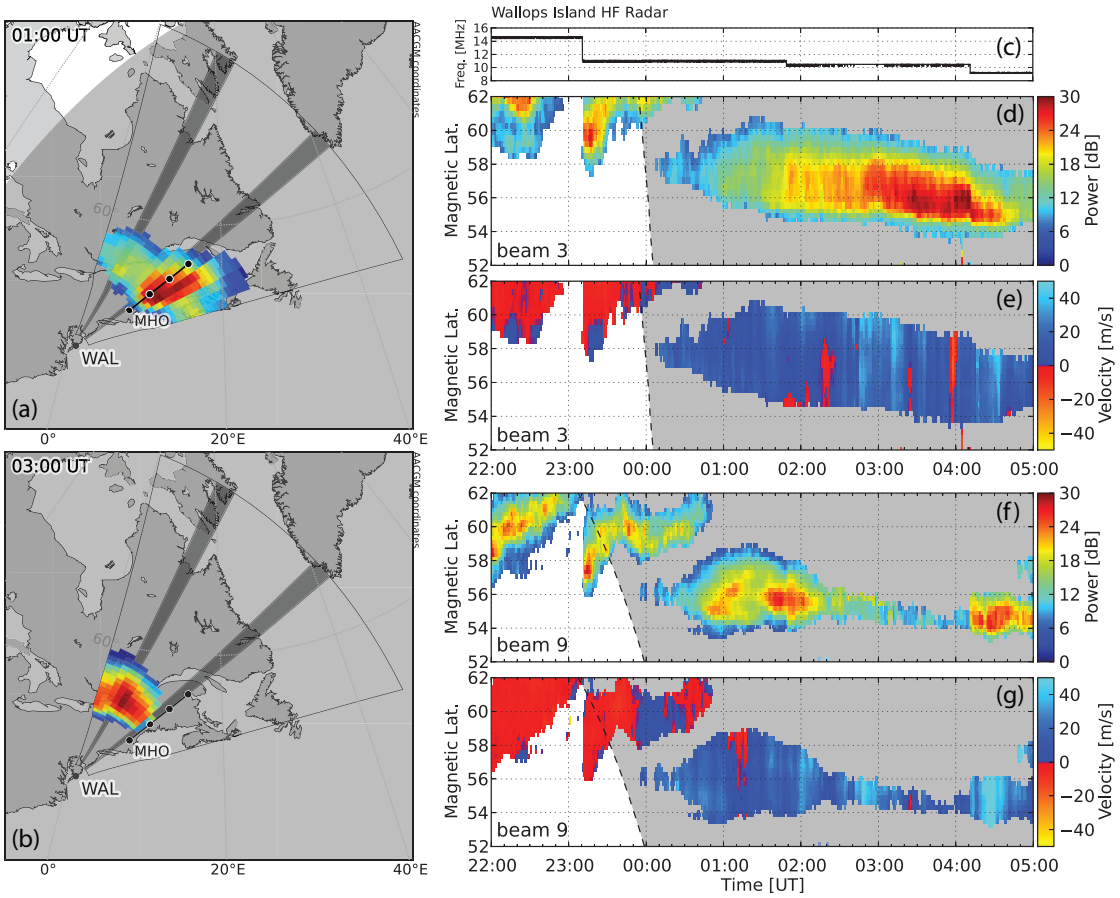

Figure 5.1. Backscatter echoes from the Wallops Island SuperDARN radar (WAL) on February 22-23, 2006. In all panels, nighttime is indicated by grey shading. (a-b) Backscatter power at 01:00 and 03:00 UT. Beams 3 (left) and 9 (right) are highlighted in dark grey. The position of the Millstone Hill Incoherent Scatter Radar (MHO) is indicated as well as the intersection of all 4 MHO pointing directions with 300 km altitude (black dots with white edges). (c) Operating frequency of WAL. (d-e) Bakcscatter power and line-of-sight Doppler velocity measured along beam 3. (f-g) Backsatter power and line-of-sight Doppler velocity measured along beam 9.

UT. These times are chosen simply to illustrate two distinct phases of the observed event. A time-lapse (not shown here) of backscatter power reveals that the peak power moves across the field-of-view from East to West for the first 2 hours of the event, until it reaches the situation shown in panel b. The distribution seen in panel b is typical of low-velocity Sub-Auroral Ionospheric Scatter (SAIS), where the apparent absence of irregularities in the rightmost part of the field-of-view is due to HF propagation effects [*de Larquier et al.*, 2013a]. Aside from the two hours immediately following sunset (dashed line in panels d through g), panel b is more representative of the backscatter distribution throughout the event.

Figure 5.1c shows that the radar operating frequency changed multiple times during the experiment. The first change at 23:10 UT from 14.5 MHz to 11.0 MHz was scheduled and made to accommodate for the drop in plasma critical frequency during the night. Subsequent changes in frequency were small and should not significantly affect propagation or scattering. Panels d through g show the backscatter observed through the experiment along beams 3 (panels d-e) and 9 (panels f-g). The scatter observed before sunset is ground backscatter, which occurs when the ionospheric plasma frequency is high enough that the HF signal gets reflected down to the ground where part of the signal can be reflected back to the radar. The discontinuity at 23:10 UT is due to the one large change in frequency which decreased the skip focussing distance [e.g., *Davies*, 1990, ch. 7]. The scatter that begins shortly after sunset is from decameter-scale ionospheric irregularities located in the F-region ionosphere and is an example of SAIS [*Ribeiro et al.*, 2012]. This is the activity of interest in this study.

The line-of-sight Doppler velocities associated with the ionospheric backscatter between 00:10 and 05:00 UT were L-shell fitted assuming a purely zonal plasma flow [*Ruohoniemi et al.*, 1989] in order to obtain estimates of the 2-D velocity. Using these fitted velocities and assuming the plasma drift is mainly driven by $\mathbf{E} \times \mathbf{B}$ drift, the F-region electric field is calculated as $E = vB$, where E is the electric field and B is the magnetic field. For this event, electric fields did not exceed 3 mV/m in the F-region. Such small electric fields are typical of quiet-time SAIS. The corresponding plasma velocities measure in the low tens of meters per second, which is much less than what is characteristic of auroral zone plasma flows. For this study, WAL data provide electric field, and the spatial and temporal extents of ionospheric backscatter occurrence.

5.2.2 Millstone Hill ISR observations

In order to determine the plasma instability mechanism responsible for the observed irregularities, we use data from the Millstone Hill Incoherent Scatter Radar (MHO). MHO is a UHF (440 MHz) radar consisting of both zenith-pointing and

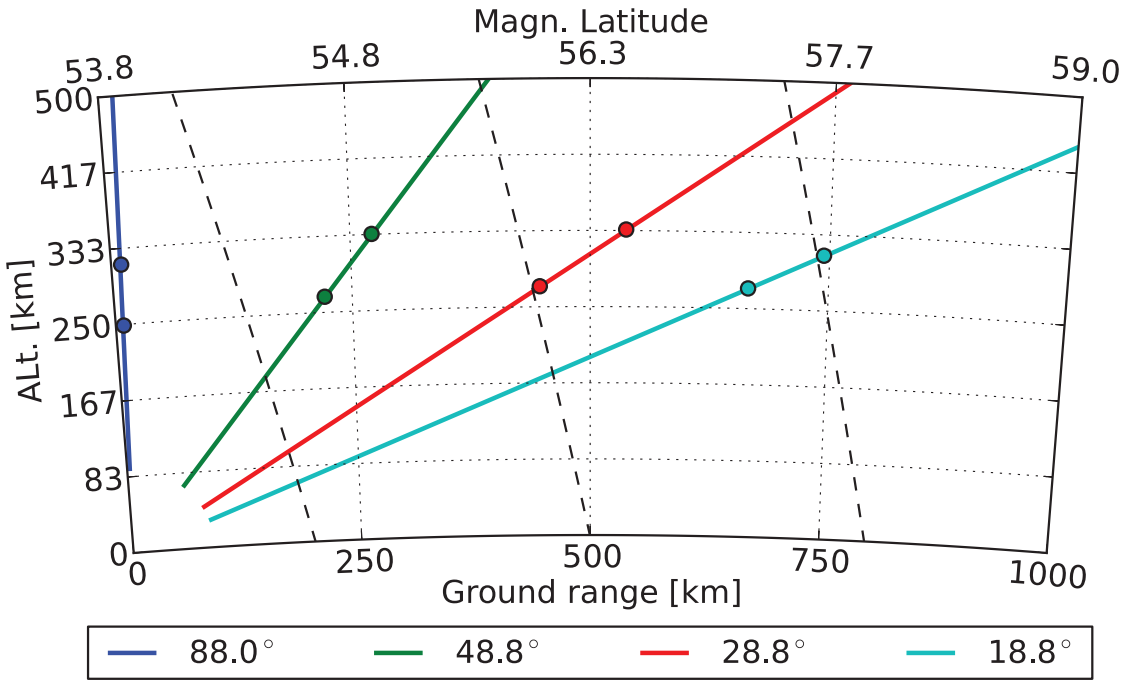

Figure 5.2. Millstone Hill pointing directions during the February 22-23, 2006 experiment. The zenith (88°) was scanned between each of the other pointing directions. The colored dots with black edges represent the extreme positions of hmF_2 between 22:00 and 05:00 UT.

steerable antenna dishes. It can measure electron densities, electron and ion temperatures, ion velocities and ion composition.

For this experiment, measurements were obtained with the zenith-pointing antenna and the steerable antenna at a geographic azimuth of 33° and elevation angles of 49°, 29° and 19°. This azimuth direction is aligned with beam 9 of the Wallops SuperDARN radar, as illustrated in Figure 5.1a-b. Each pointing direction is integrated for 240 seconds to obtain a high signal-to-noise-ratio even with the low nighttime electron densities. The zenith direction is repeated between oblique soundings, giving its data a time resolution of 8 min compared to 24 min for the other three pointing directions. The ionospheric pierce point at 300 km altitude of each pointing direction is indicated in Figure 5.1a-b.

Figure 5.2 illustrates the four pointing directions and their relative orientation with respect to geomagnetic field lines. The magnetic latitude Λ at 300 km is reported on the top y-axis of Figure 5.2, showing that the Millstone Hill observations provide significant coverage of the F-region ionosphere between $53.8° \leq \Lambda \leq 57.8°$.

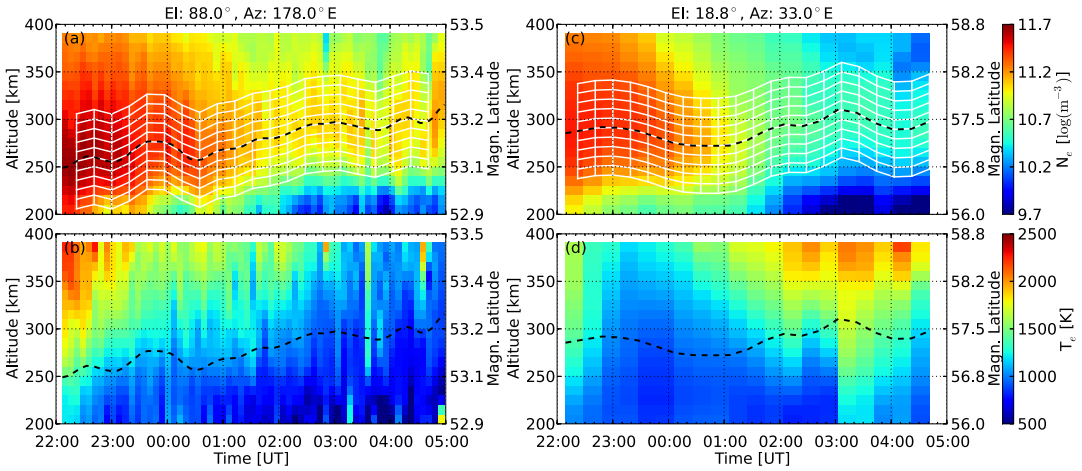

Figure 5.3. Electron density (top panels) and electron temperature (bottom panels) measured by the Millstone Hill Incoherent Scatter Radar (MHO) during the February 22-23, 2006 experiment. The left panels show observations along the zenith direction while the right panels show the lowest elevation observations. The dashed curves represent hmF_2. The white grid is made of 10 km by 20 min cells extending to 50 km above and below the F_2 peak altitude (hmF_2).

This allows proper estimation of shallow horizontal gradients near the plasmapause boundary as well as sharp vertical gradients in the top- and bottom-side F-region. Note that none of these pointing directions are perpendicular to the geomagnetic field **B**, which is the direction of importance for gradients responsible for the TGI [*Hudson and Kelley*, 1976; *Eltrass et al.*, 2013]. In Figure 5.2 we also indicate the extreme positions of F-peak altitude (hmF_2) through the hours of observations. The peak appears to have been very consistent in altitude (250-300 km) across all pointing directions.

The electron density and temperature profiles obtained with this configuration are presented in Figure 5.3 for the highest (zenith) and lowest (19°) elevations. The time sampling difference between the zenith and lower elevation is very apparent. In our analysis, we down-sample the zenith observations to the same ∼24 min resolution common to the three other pointing directions. The down-sampled values are estimated using a simple linear interpolation. Each altitude profile between 200 and 400 km (F-region) is first interpolated onto a regularly spaced altitude grid using a cubic spline interpolation, which introduces minor smoothing while preserving a great degree of fidelity to the original data. Then, the interpolated

data undergoes a convolution with a scaled Hanning window in order to smooth out any small-scale perturbations (<10 km). These two mild processing steps remove most of the noisy data by essentially smoothing out anomalous data points. This allows for more consistent evaluation of vertical and horizontal gradients. Combining measurements from the two directions presented in Figure 5.3 as well as the two other directions, the MHO data can be used to estimate electron density and temperature gradients in the F-region ionosphere.

5.3 Results

Two important points were presented in the previous section. First, hmF_2 varies between 250 km and 300 km altitude during the experiment (Figure 5.2). In Figure 5.3 we can see that in addition to time variations, hmF_2 also varies spatially within the observations region. The analysis of *Greenwald et al.* [2006] only considered the horizontal gradients by combining electron density and temperature measurements from the three highest pointing directions (28.8°, 48.8° and 88.0° elevation) at a fixed altitude of 300 km. As can be seen in Figure 5.3, this altitude could be in the top-side F-region along one pointing direction, and in the bottom-side along another. This effectively means that the computed gradients, while intended to be horizontal, included some measure of the vertical gradients. Second, and perhaps more importantly, we noted in the Introduction and again in Section 5.2.2, that the gradients driving the TGI should be perpendicular to **B**, as illustrated in Figure 5.4. This perpendicularity is a fundamental part of the TGI theory [*Hudson and Kelley*, 1976; *Eltrass et al.*, 2013]. Note that horizontal gradients in the zonal directions are perpendicular to **B**. However, the main sources of gradients lie in the meridional direction, corresponding to variations across the plasmapause footprint and auroral oval [*Holt et al.*, 2002]. For this reason, we can reasonably reduce all non-vertical gradients to their meridional component. In the following discussion, *perpendicular gradients* will refer to gradients perpendicular to **B** along the meridional direction, and *horizontal gradients* will refer to horizontal gradients along the meridional direction. Figure 5.4 describes these three gradients directions and their position

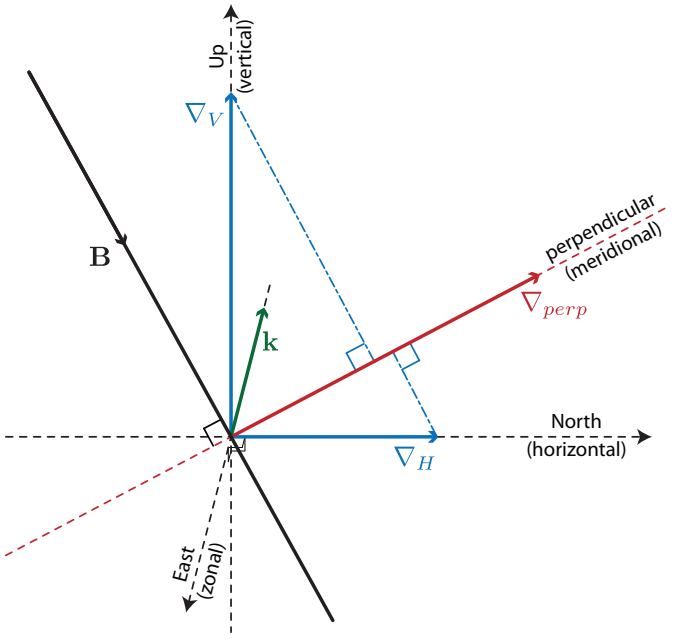

Figure 5.4. Sketch of the TGI geometry in the mid-latitude ionosphere. **B** is the Earth's magnetic field. ∇_H, ∇_V, ∇_{perp} are the horizontal, vertical and perpendicular gradients, respectively. ∇_{perp} is calculated as the sum of the projections of ∇_H and ∇_V onto the perpendicular direction. **k** is a potential TGI wave vector, which lies in the direction perpendicular to both **B** and ∇_{perp}, in the case where the density gradient is poleward and the temperature gradient equatorward. Note also that, as a drift wave, **k** could have a small component parallel to **B**.

with respect to **B** and a local East-North-Up coordinate system. In the meridional direction the perpendicular gradients lie $\sim 20^\circ$ out of the horizontal plane, further motivating the need to re-analyze data from *Greenwald et al.* [2006].

To accommodate these two important new considerations, we calculated the true perpendicular gradients, in both the top- and bottom-side F-region. Since none of the Millstone Hill pointing directions are perpendicular to **B**, the purely horizontal and vertical gradients are calculated first, then combined by estimating the geomagnetic field dip angle from the International Geomagnetic Reference Field (IGRF) model.

In order to calculate gradients using all four pointing directions, we created a 100 km altitude grid with 10 km steps centered on hmF_2, updated every $\sim$24 min. This grid allows reasonable sampling of electron temperature and density measurements. It also ensures that measurements in a given altitude cell in each pointing direction are located in the same ionospheric region with respect to the

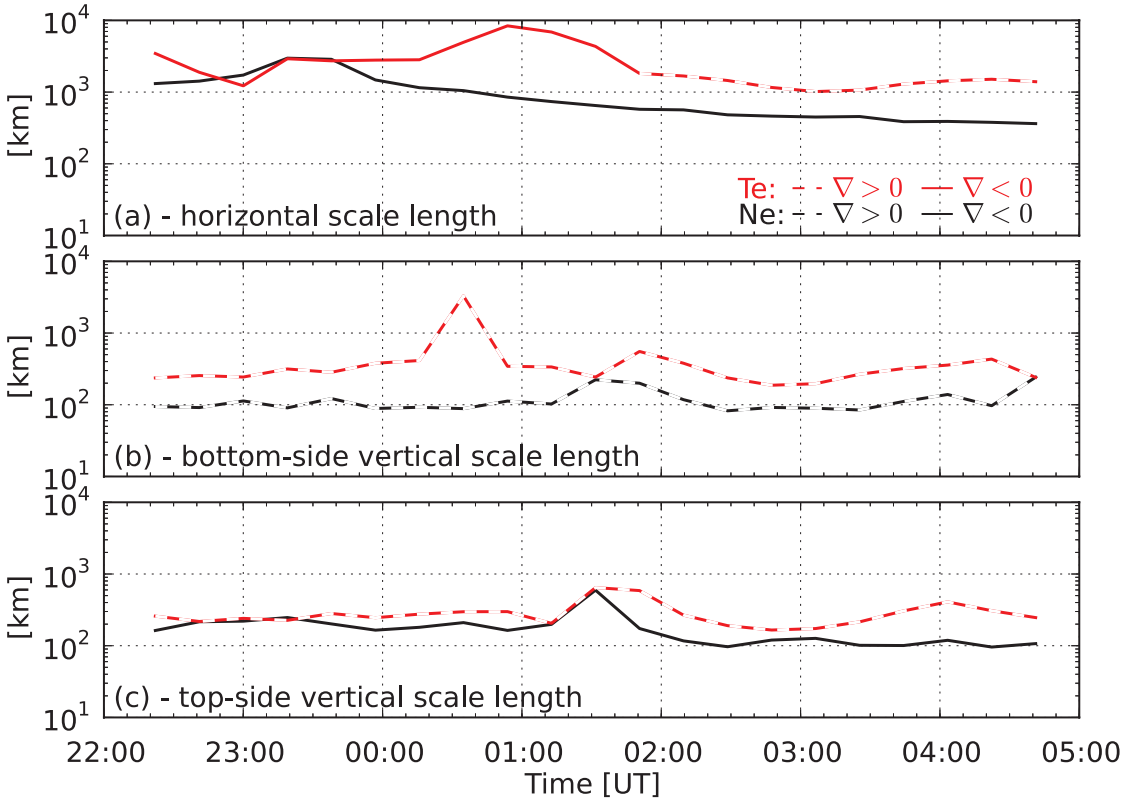

Figure 5.5. Electron density (black curves) and electron temperature (red curves) scale lengths along the (a) horizontal, (b-c) and vertical directions. The vertcial scale lengths are computed in both the 50 km below (b) and above (c) the F_2 peak. Positive gradients (dashed) are poleward for the horizontal direction and upward for the vertical direction. Negative gradients (solid) are equatorward for the horizontal direction and downward for the vertical direction.

F-peak. Figure 5.3a-b shows this grid along two of the four pointing directions. Horizontal gradients are calculated between grid-cells of equal relative altitude with respect to hmF_2 in all four pointing directions. These horizontal gradients are computed at each 10 km altitude step, and averaged over the 100 km altitude range, thus limiting the effect of anomalous measurements. Vertical gradients are calculated along the two highest elevation pointing-directions, in the bottom-side (5 lowest grid cells) and top-side (5 highest grid-cells) ionosphere. Only the two highest pointing directions are considered in order to limit the influence of horizontal gradients due to the slanted pointing directions. The vertical gradients from both pointing directions are then averaged to obtain unique values in the bottom- and top-side ionosphere at each time step.

The results of the above analysis are presented in Figure 5.5 showing the horizontal, bottom- and top-side vertical scale lengths. The scale lengths are calculated as $N_e/\nabla(N_e)$ and $T_e/\nabla(T_e)$ for the electron density (N_e) and temperature (T_e), respectively. Notice in Figure 5.5a that the horizontal temperature gradients change direction from equatorward to poleward around 01:40 UT, which can also be qualitatively observed from Figure 5.3b-d. This change of direction was noted by *Greenwald et al.* [2006] who suggested that it is due to post-sunset cooling in the equatorward region and heating due to Coulomb collisions with energetic particles in the poleward region. After 01:40 UT, the horizontal electron temperature and density gradients become opposed. However, the vertical gradients preserve their relative directions throughout the experiment. Bottom-side electron density and temperature vertical gradients are directed upward, which is consistent with typical F-region plasma density distributions and ionospheric electron temperature profiles. Following the same consistency, top-side vertical gradients are opposed, with the temperature gradients directed upward and the density gradients downward. Note that the scale lengths in the vertical direction are about an order of magnitude smaller than scale lengths in the horizontal direction. This is expected because horizontal differences in electron density and temperature are driven by large scale features such as the plasmapause projection or the auroral boundary. Additionally, horizontal gradients are measured over ∼800 km, making scale lengths on the order of 10^3 km reasonable. Vertical gradients are measured over 50 km, making scale lengths on the order of 10^2 km reasonable. These results provide most of the information needed to calculate the perpendicular electron density and temperature gradients.

Perpendicular gradients can be expressed as the sum of the projections of both vertical and horizontal gradients in the direction perpendicular to $\mathbf{B}$ (see Figure 5.4). The IGRF model indicates that the magnetic dip angle within the region of interest is ∼70°. This means that the perpendicular gradients are composed of 30% of the vertical gradients and 90% of the horizontal ones, suggesting that the latter dominates the global behavior of perpendicular gradients. However, as previously

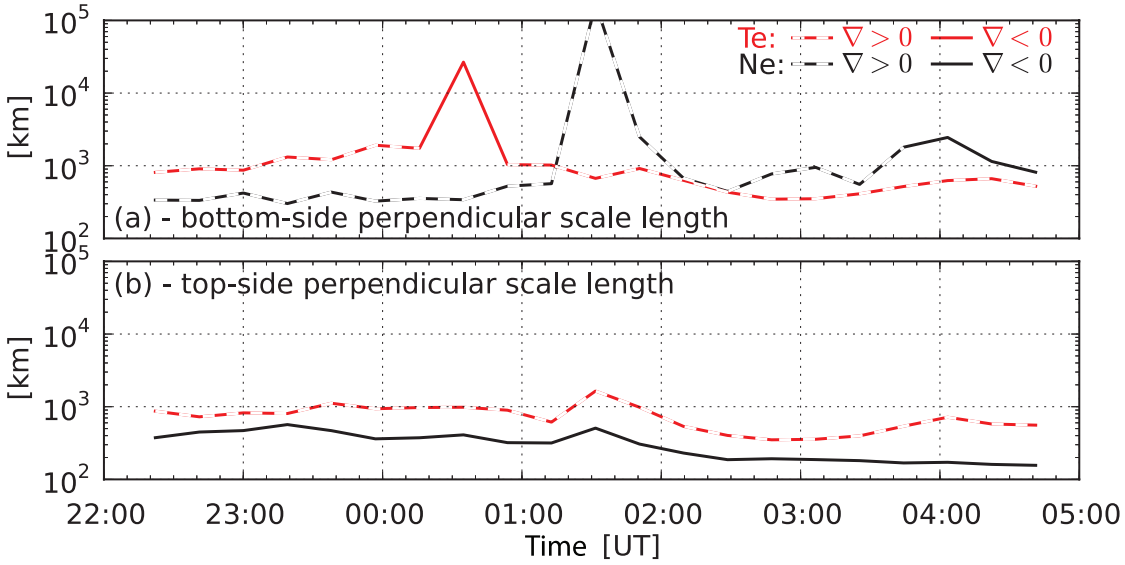

Figure 5.6. Electron density (black curves) and electron temperature (red curves) scale lengths along the direction perpendicular to the geomagnetic field **B**. Positive gradients (dashed) are poleward and up, while negative gradients (solid) are equatorward and down.

noted, due to larger gradients in the vertical direction, calculations indicate that the vertical gradients have a strong influence on the perpendicular ones. Figure 5.6 shows the perpendicular electron density and temperature scale lengths. The large values at 00:30 and 01:30 UT can be attributed to very small calculated gradients, which are most likely the results of noisy measurements. Comparing Figure 5.6 to 5.5b-c, the influence of vertical gradients is apparent, especially in the sign of the perpendicular gradients. It can be seen that, for most of the experiment, the bottom-side perpendicular temperature and density gradients are in the same direction (poleward and upward). The change in the sign of the temperature gradient around ∼00:30 UT is associated with the increase in the bottom-side vertical scale-lengths (Figure 5.5b), allowing the horizontal gradient to dominate. This however is likely an anomaly, since the top- and bottom-side temperature scale lengths are almost identical, except for this peak at 00:30 UT. The change in the sign of the electron density gradient around ∼04:00 UT is due to the horizontal scale length becoming similar in magnitude to the vertical one, and may have implications for the observed irregularities. The top-side perpendicular gradients are in opposite directions throughout the experiment, which is a fundamental growth

condition of the TGI. The implications of these new results are discussed in the next section.

5.4 Discussion

The results of Figure 5.5a are closely related to those of *Greenwald et al.* [2006]. The main difference between Figure 5.5a and the scale lengths calculated by *Greenwald et al.* [2006] is that we corrected for hmF_2 variations, while they used a fixed altitude of 300 km. Both approaches show a reversal of the horizontal electron temperature gradients just before 02:00 UT. This led *Greenwald et al.* [2006] to conclude that the TGI could be responsible for the observed irregularities. However, since irregularities were observed prior to this reversal, they had to suggest that another mechanism may account for the irregularities observed between 00:00 and 01:40 UT. This additional mechanism was associated with a type of scatter called dusk scatter in SuperDARN literature [*Ruohoniemi et al.*, 1988]. Dusk scatter does not typically connect with scatter from other irregularity types in a smooth transition such as seen in Figure 5.1d-f. The continuity of the scatter presented in Figure 5.1d-f suggests that it is more likely to be the result of a common group of irregularities with similar growth conditions. Most importantly, the TGI growth conditions rely on gradients perpendicular to $\mathbf{B}$, a criterion that the horizontal gradients fail to satisfy by $\sim 20°$.

Having calculated the perpendicular gradients, we are now presented with the opposite problem, where growth conditions seem satisfied for the duration of the experiment (Figure 5.6b), yet irregularities were only observed for 5 of the 7 hours of observations. We note that even if growth conditions were only satisfied in the top-side F-region, the irregularities might be able to grow anywhere in the F-region due to the high conductivity of magnetic field lines.

The absence of observed irregularities between 22:00 and 00:00 UT can be the result of two distinct conditions. The first is that HF propagation conditions are such that, even with irregularities present, aspect conditions [e.g. *Davies*, 1990] are not satisfied in the proper ionospheric region (altitude and latitude). In Figure

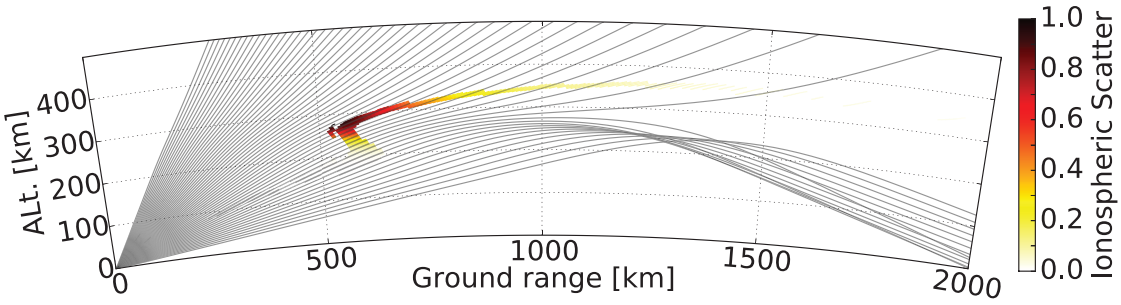

Figure 5.7. Ray-tracing coupled with IRI at 23:30 UT on February 22, 2006, for beam 3 of the Wallops SuperDARN radar, at a frequency of 11 MHz. The time is chosen to be slightly before irregularities are observed. IRI hmF_2 and NmF_2 are forced to the values measured by the Millstone Hill ISR at this time. The color scale indicates good aspect conditions weighted by range and background electron densities. Individual rays are plotted in grey.

5.7 we have computed ray paths using a ray tracing model coupled with the International Reference Ionosphere (IRI). To increase realism, we have constrained IRI to the hmF_2 and peak electron density (NmF_2) measured by MHO. We identify regions of good aspect conditions weighted by range from the radar and background electron density to estimate the relative amplitude of backscatter from irregularities that are assumed to be uniformly distributed throughout the ionosphere [*de Larquier et al.*, 2013a]. The results presented in Figure 5.7 show that propagation conditions are favorable to observing decameter-scale irregularities in the F-region earlier than is observed. This ray-tracing analysis has been shown to account substantially for the distribution of SAIS seen with SuperDARN [*de Larquier et al.*, 2013a], suggesting that propagation was not the controlling factor and did not limit the observation of irregularity backscatter.

The second potential explanation is the E-region conductivity, which can short-out electrostatic waves generated in the F-region. The E-region conductivity is directly related to E-region electron densities, which at these latitudes and geomagnetic activity levels is mainly controlled by photoionization. The day-night terminator for the ionosphere at 300 km altitude (zenith angle of 107°) was plotted in Figure 5.1 and occurred around 00:00 UT. It can be seen that irregularities were being observed within 10 to 20 minutes after the sun had set in the ionosphere. This short delay between sunset and irregularity observations argues in favor of the E-region as the controlling factor for irregularity growth. Note, however, that

this delay is longer than typical E-region recombination rates [e.g., *Schunk and Nagy*, 2009, ch. 11]. The effect of the Southern hemisphere on the appearance of these irregularities may also be neglected as it remains sunlit during this transition. Unfortunately, the data available to this study are not sufficient to establish the cause of the short delay between the dissipation of the E-region and the start of irregularity observations. It is, however, very likely that the E-region is responsible for the absence of observed irregularities before sunset in spite of favorable growth conditions for the TGI in the top-side F-region. After sunset, irregularities were able to grow from the TGI for the remainder of the experiment, as suggested by the top-side gradients (Figure 5.6b) and Wallops observations (Figure 5.1). The restriction of SAIS to hours of darkness was demonstrated statistically by *Ribeiro et al.* [2012].

Interestingly, the involvement of the E-region in shorting out F-region electric field before and around sunset raises another important question about the wavelength of the irregularities. It can be shown that perpendicular structures with scale sizes smaller than 1 km are greatly attenuated when mapped from the F- to the E-region [e.g. *Farley*, 1959; *Kelley*, 2009, Ch. 2]. We numerically integrated the electric potential differential equation from [*Farley*, 1959] using a Gauss-Seidel method [*Potter*, 1973, e.g.], assuming a harmonic solution in the plane perpendicular to $\mathbf{B}$. We used realistic conductivity profiles derived from IRI, MSIS and IGRF for the night of the experiment described in this Chapter at 23:30 UT. In Figure 5.8, we show the results of this integration as the electric potential attenuation from a source located near 350 km altitude at 23:30 UT on the night of the presently described experiment. It can be seen that electric fields with scale sizes of one kilometer or less are several orders of magnitude attenuated by the time they reach the E-region. This effectively means, that for small scale sizes, the top-side F-region and E-region are not electrically connected. Consequently, for the E-region to be responsible for shorting out the F-region TGI electric fields, the irregularities should be on the order of a few kilometers. This would also imply that a cascade process down to the observed decameter-scale irregularities must

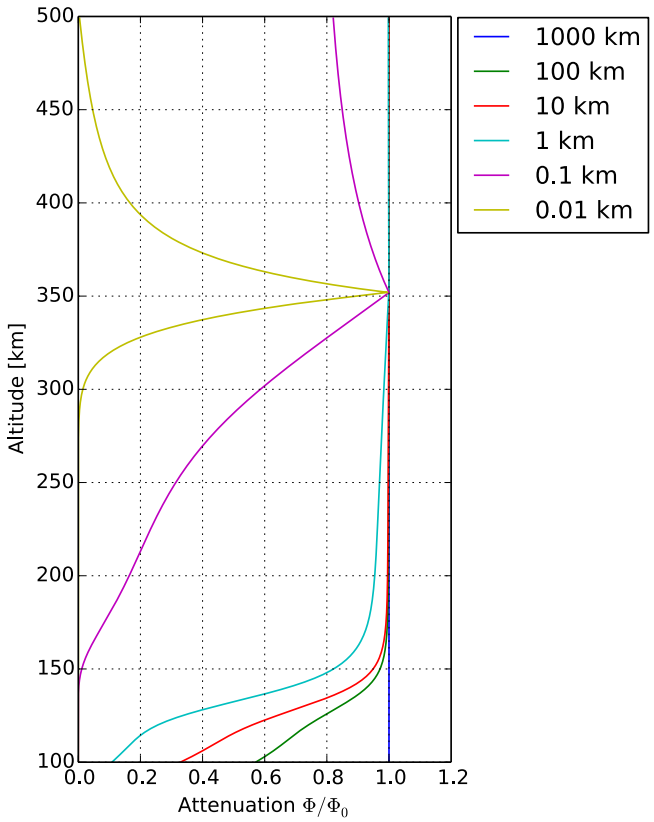

Figure 5.8. Electric potential attenuation between the top-side F-region and the E-region for different perpendicular scale sizes. Conductivity profiles used to calculate the potential are derived from IRI, MSIS, and IGRF on the night of the experiment at 23:30 UT, using NmF_2 and hmF_2 measured by MHO.

occur. More details on the dependence of TGI growth on wavelength is discussed in the companion paper [*Eltrass et al.*, 2013].

5.5 Summary

Data from the Millstone Hill ISR and the Wallops SuperDARN radar have been analyzed to investigate the potential role of the TGI in the formation of widespread decameter-scale mid-latitude irregularities. Previous results from *Greenwald et al.* [2006] were improved to account for hmF_2 variations and magnetic dip angle. Both parameters provide necessary but overlooked information to evaluate electron temperature and densities in the plane perpendicular to the geomagnetic field. In this plane, most variations are along the meridional direction, allowing gradients in

the perpendicular plane to be reduced to this single component. Only when electron density and temperature gradients along this direction are opposed can the Temperature Gradient Instability (TGI) grow. We showed that growth conditions exist in the top-side F-region ionosphere throughout the experiment. This result modifies previous conclusions which relied on a different instability mechanism to explain a portion of the observed irregularities. We show that while growth conditions existed at the beginning of the experiment, no irregularities were observed for 2 hours. Two factors are suggested to explain the absence of observed irregularities. The first is a restriction due to unfavorable HF propagation conditions. However, ray-tracing results using Millstone Hill electron density information and IRI show the likelihood of a region of good aspect conditions at F-region altitudes 30 minutes before irregularities were observed. The second factor which can potentially explain the absence of observed irregularities for the first 2 hours is shorting out of F-region electric fields by the E-region conductivity. This is indicated by the near coincidence of sunset in the ionosphere and the onset of backscatter from irregularities. After the sun sets, the TGI growth conditions remain satisfied and could very well be responsible for the observed irregularities. A more quantitative analysis of growth rates and time-scales is the next logical step to the analysis presented in this study, and is carried out in the companion paper [*Eltrass et al.*, 2013]. Additional insight could be obtained by reproducing the experiment described in this study under more varied sets of geomagnetic and seasonal conditions.

Chapter 6

Summary and Suggestions for Future Research

6.1 Summary of Results

We set out to identify and characterize prominent recurring features of the sub-auroral ionosphere under quiet geomagnetic conditions. First, for this purpose, we developed a model of HF propagation in the quiet-time sub-auroral ionosphere for comparison with SuperDARN observations. Second, using the aforementioned model, we investigated a Summer Evening Anomaly (SEA) in ground backscatter observed with the Blackstone SuperDARN radar. Third, based on successful comparison between model results and SuperDARN observations, we derived the characteristics of nighttime low-velocity Sub Auroral Ionospheric Scatter (SAIS). Finally, armed with new and more accurate spatial and temporal information concerning the ionospheric conditions during periods of SAIS occurrence, we tested the validity of the Temperature Gradient Instability (TGI) as the growth mechanism for SAIS irregularities.

The principal scientific contributions presented in this thesis can be summarized as follows:

- Development of a fast and robust ray-tracing model which can be coupled with various ionospheric models (IRI, ISRIM, ...) providing a realistic framework

for interpreting SuperDARN observations in the mid-latitude ionosphere:

  - The model was shown to accurately represent the distribution of ground scatter as seen by mid-latitude SuperDARN radars, including daily and seasonal variations;
  - Prediction of potential ionospheric scatter distribution under quiet geomagnetic conditions has been shown to compare well with the location of observed low-velocity Sub-Auroral Ionospheric Scatter (SAIS);
  - A parallel implementation with an online interface provides public access to the model, enabling the SuperDARN community to easily compare SuperDARN observations with expected High Frequency (HF) propagation.

- Identification and characterization of the Summer Evening Anomaly (SEA) and Weddell Sea Anomaly (WSA) in SuperDARN observations:
  - Successfully reproduced observations using the ray-tracing model coupled with IRI;
  - Demonstrated that the IRI model accurately captures both anomalies, which had never previously been reported in the case of the SEA;
  - Modeled the potential role of neutral winds and the global geomagnetic field configuration in the formation of the electron density enhancement associated with the SEA.

- Characterization of recurring sub-auroral ionospheric irregularities during quiet geomagnetic conditions associated with low-velocity SAIS:
  - Observation of such irregularities by SuperDARN radars is limited by a 1° aspect condition, proving that these irregularities are highly field-aligned;
  - The irregularities are confined to the bottom-side F-region, between 200 and 300 km altitude;
  - The irregularities extend across a large portion of the mid-latitude ionosphere, wider than the SuperDARN scatter limits due to HF propagation factors.

- Analysis of SuperDARN and Millstone Hill data shows that the Temperature Gradient Instability (TGI) is a potential mechanism for the growth of recurring sub-auroral ionospheric irregularities during quiet geomagnetic conditions:
  - Electron temperature and density gradients in the direction perpendicular to **B** satisfy TGI growth conditions in the top-side F-region even before irregularities are observed;
  - Irregularities start forming shortly after the sun sets on the ionosphere, suggesting that E-region conductivity may be shorting-out electrostatic waves generated in the F-region from the TGI;
  - Electric potential attenuation between the F- and E-region suggest the irregularities may develop at kilometer scale lengths and cascade down to the observed decameter scale.

6.2 Publications and presentations

Results from this research have been presented at the URSI National Radio Science Meeting [2011], the CEDAR workshop [2011,2012,2013], and the SuperDARN workshop [2011,2012,2013]. Two articles have been published in the Journal of Geophysical Research [*de Larquier et al.*, 2011, 2013a], two manuscript on the Temperature Gradient Instability has recently been submitted as companion papers [*de Larquier et al.*, 2013b; *Eltrass et al.*, 2013]. Finally, four co-authored papers has been published [*Ribeiro et al.*, 2011, 2013a, b; *Milan et al.*, 2013; *McDonald et al.*, 2013] on topics related to this research.

6.3 Suggestions for Future Research

In any research endeavor, new results and discoveries generally bring new questions. The research presented in this dissertation does not escape this age-old rule. The three main topics investigated here, HF propagation, summer evening electron

density enhancements, and quiet-time mid-latitude ionospheric irregularities each brought to light a new set of unknowns.

The ray-tracing model presented in Chapter 2 has been shown to provide accurate comparisons with quiet-time SuperDARN data. However, due to simplifications made in its development, it would quickly fail during disturbed periods. A very useful enhancement would be to add off-great-circle propagation paths to the model. This effort would require re-deriving part of the governing equations, but should not require much modifications in the numerical integration or the codebase in general. Another, more ambitious, research direction would be to integrate the SuperDARN observations with teh modeling in order to derive information about the ionosphere by adjusting the ionospheric model to match ray-tracing with the measurements. This could be a first step in the direction of integrating SuperDARN data in empirical ionospheric model such as IRI.

The SEA discussed in Chapter 3 observed by SuperDARN has been shown to be part of a global phenomena. However, while we showed how thermospheric neutral winds may be responsible for the formation of the SEA, it has yet to be verified. Developing a physics-based model including the role of neutral winds, the geomagnetic field configuration, and inter-hemispheric conjugacy would greatly help finalize the mechanism of SEA.

Chapter 4 has clearly established the influence of HF propagation on the observation of SAIS. As a follow-up into the physics of the irregularities behind it, Chapter 5 has demonstrated that the TGI is a very likely driver. However, our results indicate that the irregularities, while observed at decameter-scale, may be grown at larger (kilometer) scales. This needs to be further verified either by observing these larger scale sizes, or by conducting a statistical analysis of SAIS to verify that the indicators that lead to suggesting the existence of larger scale irregularities are significant. Finally, in-situ measurements of electric fields, densities and temperatures in the bottom- and top-side F-region would provide valuable if not final insight into the formation of these irregularities and the validity of the TGI as a driver.

Appendix A

Ray-tracing: implementation

This appendix provides a detailed visual description of the ray-tracing code used to implement the model described in Chapter 2. The code is mainly written in Fortran in order to interface with various ionospheric models, most of them also Fortran-based. However, wrappers exist in both IDL (deprecated) and Python (still under active development).

In the following Figures A.1 and A.2, each block is color coded accorded to its depth in the time, azimuth and elevation loops required to reproduce most SuperDARN observations. Figure A.1 describes the logic of the general algorithm, including the location of the ionospheric model plugin. Figure A.2 describes the structure of the numerical integration code used to compute each single ray path. Note that the ray-tracing is also fully integrated in our Space Science Toolkit (DaViTpy) described in Appendix C.

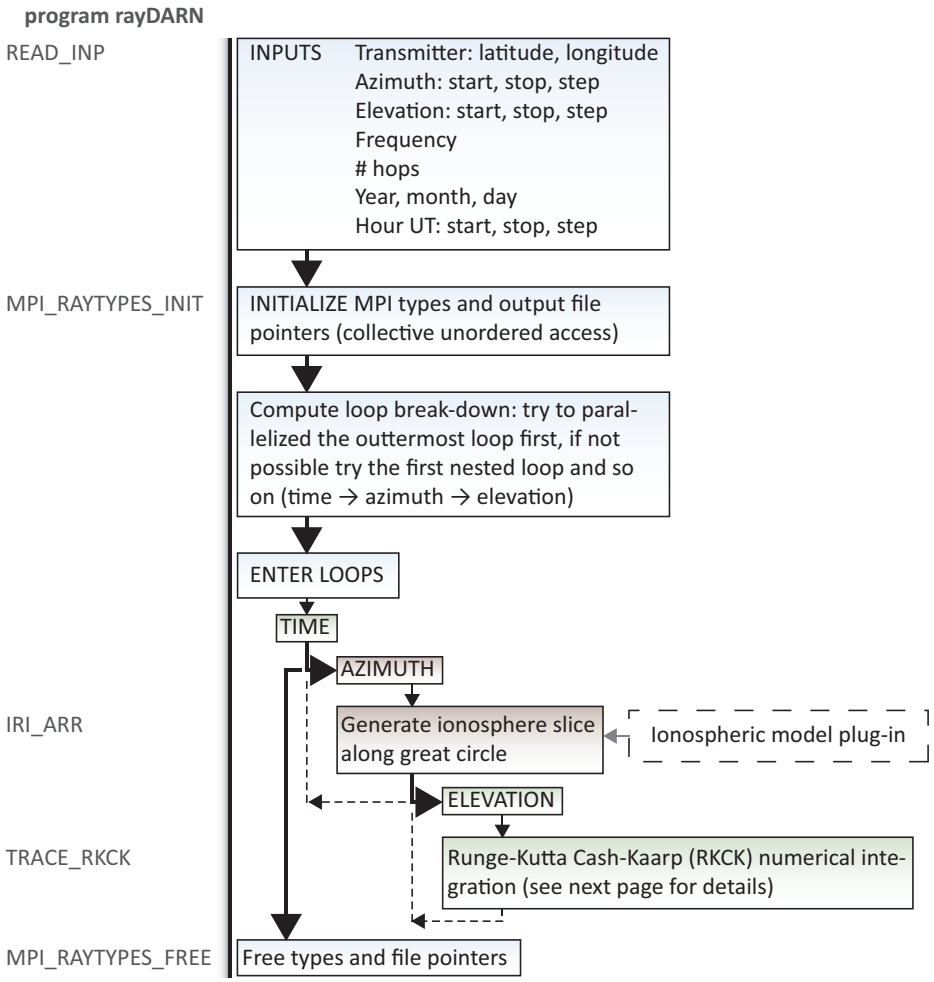

Figure A.1. Ray-tracing algorithm. The left-hand-side shows the fortran subroutines involved in each step; steps without an associated function name are embedded into the main program.

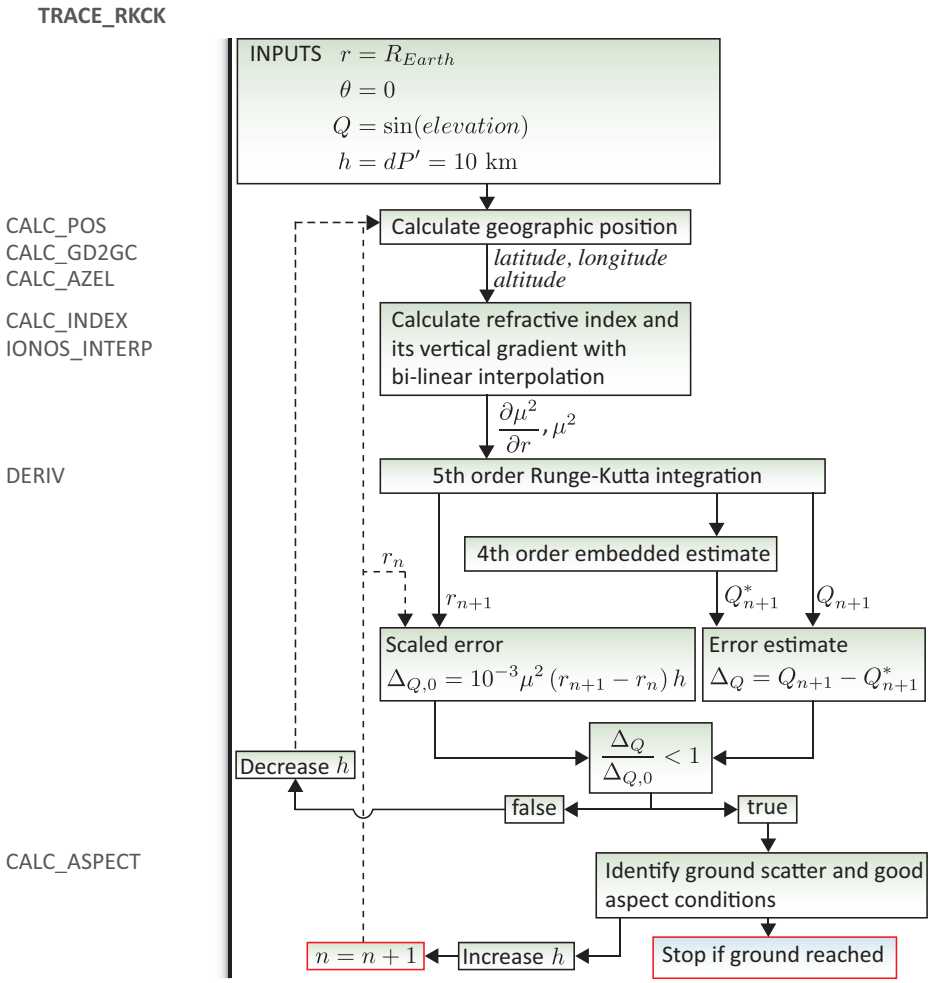

Figure A.2. Single ray path algorithm. The left-hand-side shows the fortran subroutines involved in each step; steps without an associated function name are embedded into the main subroutine. See Chapter 2 for equations and notations.

Appendix B

Elevation angle measurements: method and limitations

B.1 Concept

Most SuperDARN radars are composed of a main antenna array responsible for transmitting and receiving, and a secondary smaller interferometer array, either in front or behind the main array, designed to provide elevation angle measurements of received signals. Note that the first interferometer array in Goose Bay had as many antennas as the main array, but 12 antennas were later removed to be used for the Kapuskasing radar. Since then, all interferometer arrays are composed of 4 antennas, providing sufficient sensitivity for elevation angle measurements.

The elevation angle is the angle between the local horizon and the direction of highest Signal to Noise Ratio (SNR) of a backscatter echo. SuperDARN antenna patterns have a broad elevation profile [e.g., *Sterne et al.*, 2011], but backscattered signals are typically returned within a small range of directions whose position in the vertical plane along the beam pointing direction is measured by the elevation angle.

Elevation angle contains information about backscatter altitude and direction

[e.g., *André et al.*, 1998]. It has previously been used to assess backscatter contamination with echoes from the backward lobes of the antenna *Milan et al.* [1997a], to estimate refractive index in the scattering volume in order to correct Doppler velocity measurements [e.g., *Gillies et al.*, 2009] and to monitor the F region peak electron density [*Ponomarenko et al.*, 2011].

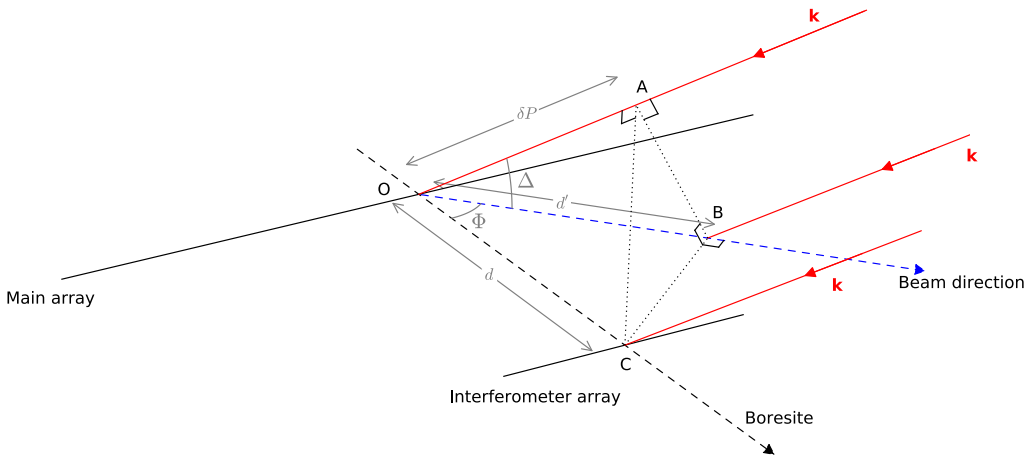

Figure B.1. Geometry of interferometric measurements of elevation angle [*Milan et al.*, 1997b].

B.2 Method

Figure B.1 illustrates the geometry for measuring elevation angle. Here the interferometer array is depicted in front of the main array. The boresight direction is perpendicular to the line of both arrays and it is assumed that the arrays are centered, such that the antennas of the smaller array lie directly in front of the middle antennas of the main array. The separation between the arrays is the distance d. The main array is phased to transmit and receive along the azimuth Φ, corresponding to the indicated beam direction; the interferometer array is phased to receive in the same direction. The backscatter returns are indicated by the $\mathbf{k}$ vectors of elevation angle Δ. The triangle ABC lies in the plane perpendicular to $\mathbf{k}$, marking a phase front; the additional distance travelled by the backscatter signal to reach the main array is indicated by the distance δP.

Note that for a linear phased array, the imposed phase variation from element to element corresponds to steering in terms of an angle α that defines the surface of a cone that has its axis aligned with the array. At the intersection of the cone and the plane of the horizon, the elevation angle is zero, and α is equal to the beam azimuth; for other directions along the surface of the cone, azimuth is a function of elevation angle [*Milan et al.*, 1997a]. This describes the situation for beam steering on the main array for both transmit and receive. With the addition of an interferometer array, we have a second axis for measuring phase variation on receive only. Let the cone angle associated with the axis of the interferometer array be β. Then the intersection of the two cones defined by α and β determines the pointing direction on receive. In practice, a phase difference is measured between the main and interferometer arrays and is combined with the phase variation imposed on the main array to solve for α and β and hence elevation, while the azimuth is simply assigned based on the main array specification and an assumption of zero elevation angle. In principle, the determination of azimuth can be improved by consideration of α and β. The full working up of elevation and azimuth from radar measurements, including adjustments for offset and non-level arrays was originally carried out by Kile Baker.

Elevation angle data is obtained by measuring the phase difference between the signal received by the main and interferometer arrays. Phase is calculated by cross-correlating the signals from the main and interferometer receiving channels. Subtracting transmission line and electrical effects from the measured phase difference, the elevation angle can be obtained according to the equation (see Figure B.1 for a description of various parameters):

$$\sin \Delta = \left(\cos^2 \Phi_0 - \frac{\Psi^2}{|\mathbf{k}|^2 d^2} \right)^{\frac{1}{2}} \tag{B.1}$$

where Φ_0 is the azimuthal pointing direction at $\Delta = 0^\circ$ and Ψ is the phase difference measured between the main and interferometer arrays. This equation accounts for

the fact that the azimuthal pointing direction varies as a function of elevation angle ($\cos^2\Delta\cos^2\Phi + \sin^2\Delta = \cos^2\Phi_0$).

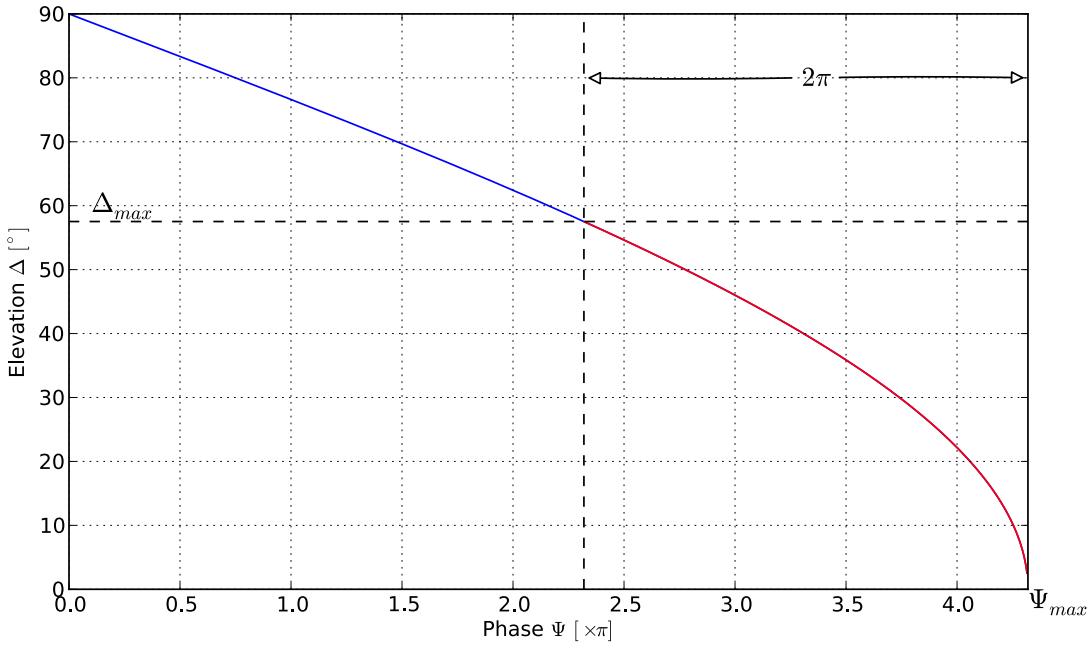

Figure B.2. Calculated elevation as a function of measured phase difference between main and interferometer arrays for the Blackstone radar, as described in equation B.1. The red portion of the curve marks the range of unambiguous elevation angles which can be measured by the Blackstone radar. Elevation angles larger than Δ_{max} will be aliased.

Figure B.2 illustrates the relation between elevation angle and phase, as represented by Equation B.1. When backscatter signals originate from straight above the radar ($\Delta = 90°$) they arrive simultaneously at both the main and interferometer arrays, resulting in no phase difference Ψ. At the other extreme, when backscatter returns originate on the horizon ($\Delta = 0°$), the distance δP in Figure B.1 is at its maximum, so the phase difference Ψ is also maximized. The total phase difference in the example shown in Figure B.2 maximizes at 4.3π, which implies that the measured phase will incorporate multiple 2π foldings. Part of the curve in Figure B.2 is highlighted in red to illustrate the range of elevation covered by one 2π-folding with the Blackstone radar configuration.

Figure B.2 demonstrates one important limitation which needs to be considered when calculating elevation angles from equation B.1. The radar measures a phase difference between $\pm\pi$. However, the distance between interferometer and main array d is typically larger than the radar wavelength λ. Consequently, the true phase shift Ψ between interferometer and main array is larger than 2π, causing what has been dubbed a 2π ambiguity. This ambiguity is removed by assuming that the true phase lag lies between the maximum possible phase lag Ψ_{max} (corresponding to zero elevation) and the first 2π-folding. The maximum possible phase lag Ψ_{max} is calculated as the time delay through the cables and electronics in each array receive-paths. This limitation imposes an important constraint on elevation angle measurements: the unambiguous elevation range. Depending on the distance d between interferometer and main array, there exists a maximum unambiguous elevation Δ_{max} after which elevation is aliased.

This limitation to calculating SuperDARN elevation can be summarized as follows (see Figure B.2 for an illustration):

- $\lambda < d$, which implies $\Psi > 2\pi$, but the radar measures $-\pi < \Psi_0 < \pi$, leading to 2π ambiguities in the phase lag. This is typically resolved assuming that the true phase lag lies between the maximum possible phase lag $\Psi_{max} = |k|d\cos\Phi_0$ and the first 2π ambiguity, i.e. $\Psi_{max} - 2\pi < \Psi < \Psi_{max}$.
- the range of unambiguous elevation angle is limited by the distance between the main and interferometer arrays:

$$\cos\Delta_{max} = 1 - \frac{2\pi}{|k|d\cos\Phi_0}$$

In routine observations, we are at risk of obtaining scatter from higher elevation angles and assigning it to lower angles. Figure B.3 shows the elevation ambiguity for the Blackstone radar. In this example, signal from an elevation of 68° would be attributed to scattering at and elevation of 10° elevation. Though higher elevation angles do not dominate typical SuperDARN backscatter, this is an important

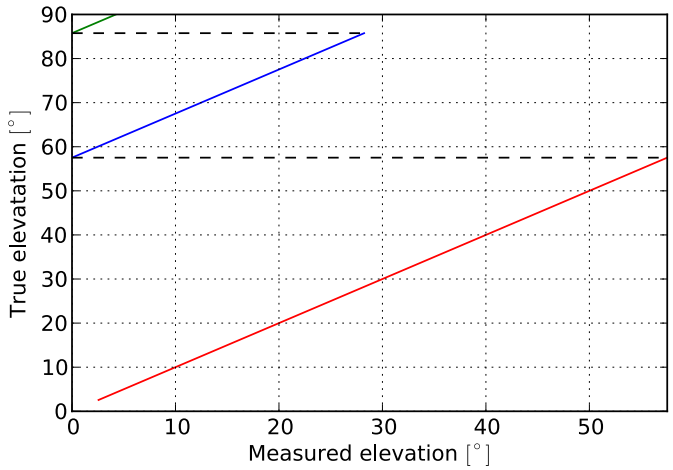

Figure B.3. True elevation as a function of measured elevation for the Blackstone radar. Each time the phase difference between main and interferometer array folds by 2π, the measured elevation is aliased. The red curve shows the range of unambiguous elevation, the blue curve the range of elevation aliased once, and the green curve the range of elevation aliased twice.

limitation to be considered when interpreting elevation angle data.

Historically, the distance d between interferometer and main arrays was set at 100m, leading to ambiguities at elevations greater than 44°. Beginning with the Wallops Island radar, d was reduced. The Blackstone radar for instance has $d = 60$m, corresponding to aliasing at elevation angles greater than 57°.

B.3 Phase calculation errors

It has been noticed that significant errors in the phase difference Φ_0 between the main array and the interferometer array were common. These erroneous phases usually result in high elevation angles contaminating SuperDARN elevation data. This error is shown in the top panels of Figure B.4, mostly in beam 7. The error is prominent when the resolved phase difference lies near the $\pm\pi$ transition.

The data presented in Figure B.4 have been median filtered so that random noise is largely removed. Upon analysis of the code that calculated the phase difference Φ_0, it appears that the error may be due to bad points in the cross-correlation results: these outlying points are taken into account when estimating the mean phase of the interferometer array. Then, Φ_0 is calculated as the difference between

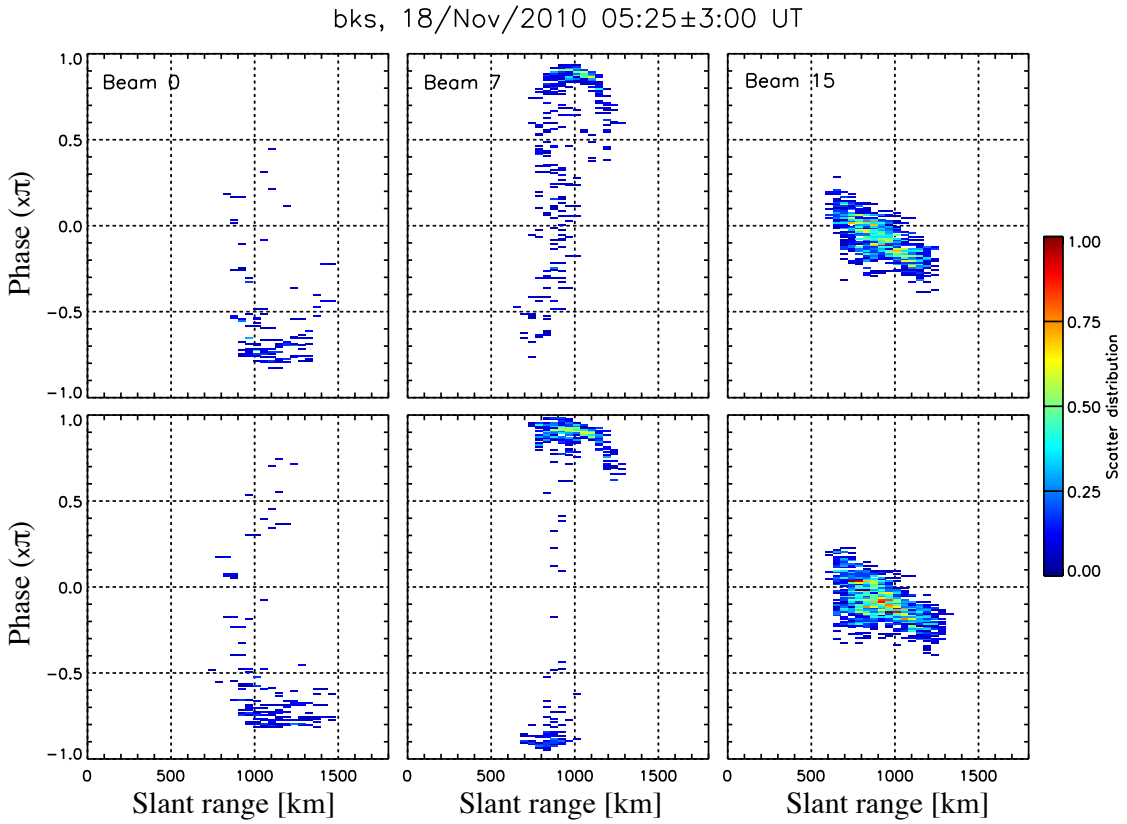

Figure B.4. Phase difference Φ_0 between the main array and the interferometer for beams 0, 7 and 15 of the Blackstone SuperDARN radar, on November 18^{th}, 2010, for 3 hours before and after local midnight. Beam 7 is the central beam, beams 0 and 15 are the westernmost and easternmost beams, respectively. (top panels) Phase calculated before correction. (bottom panels) Phase calculated after correction.

the mean phase of the interferometer array, and the mean of the fitted phase of the main array. Outliers in the interferometer array phase are likely responsible for offsetting this calculated difference considerably.

A temporary solution has been implemented to take the median of the interferometer phase instead of the mean: results are then plotted on the lower panels of Figure B.4. Phase results are considerably improved, with only a small amount of deviation from the expected distribution.

It should be noted that the azimuthal distribution of this error (lowest in the most meridional beams, i.e., beams 10 and above) seems correlated with the azimuthal distribution of aspect conditions: propagation conditions for the most meridional beams are more favorable for reaching orthogonality with the back-

ground magnetic field, thus resulting in higher likelihood of ionospheric scatter, hence a higher received power.

Appendix C

DaViTpy: An Open-Source Collaborative Space Science Toolkit

A collaborative endeavor by: A.J. Ribeiro, S. de Larquier, N. A. Frissell, B. S. R. Kunduri, E. G. Thomas, J. M. Ruohoniemi, J. B. H. Baker, J. Spaleta

C.1 Introduction

Science marches forward by combining theoretical and experimental insights into reproducible and/or demonstrable concepts. Since the early days of punch-cards, computers have increasingly contributed to the scientific method. Not only have computer programs simplified complex calculations, they have opened the doors to much larger scale endeavors, from multi-scale coupled physical models to multi-instrument space-borne experiments.

As a subset of this adventure, space science is intensely data driven. To understand the ionosphere, magnetosphere and interplanetary environment, data are used to validate complex physics-based models, to build empirical models, and to drive new discoveries. Most published space science results during the past 20 or 30 years have relied on some form of computer program to record, visualize, analyze and synthesize data into meaningful insights. Some of the software developed in this process and used in published results is propagated to the community, but most never spreads further than a handful of computers in a single institution.

Due to the incremental nature of science in general, this process is demonstrably inefficient. However, it can be easily improved, without having to rely on unproven cutting edge technologies, by simply adopting some of the well tested practices of software engineering. Interestingly, one of the fundamental aspects of such practices is also key to all scientific results, reproducibility. By sharing and combining code built by experts in each domain, it is possible to build robust foundations to enable further discoveries.

Scientific software tools, like scientific results, should be free and open to all, easily accessible, with a transparent history. Experts should contribute their knowledge and skills to the codebase, and the community should be responsible for its maintenance and validation. Code should be generously documented and flexible, with revision and enhancement integrated in existing software rather than published as independent packages. All these criteria are fundamental, and easily enabled by existing tools and processes, such as open-source and free-software practices like distrtibuted version control.

The astronomy community has understood the value of such an effort, and has released multiple community developed software packages which continue to grow [e.g., *Hanisch and Jacoby*, 2001; *Robitaille et al.*, 2013]. In space science, institutions have brought together modeling efforts, and to some extent data warehouses, but community driven software tools are very rare.

In the past year, we have been working with members of the international SuperDARN community to develop a new Data Visualization Toolkit (DaViTpy) for the space sciences. It leverage the power of the Python programming language and robust numerical packages such as Numpy [*Oliphant*, 2006] and SciPy [*Jones et al.*, 2001]. While it started as a SuperDARN toolkit, its mission has been extended to more general space science applications. It includes modules to access data from multiple instruments (e.g., SuperDARN, POES, OMNI) and multiple indexes (e.g., Kp, AE, Dst). It also includes several fundamental models (e.g., IRI, MSIS, HWM) kept in their original FORTRAN or C native language, but wrapped in Python to enable their use with data and other models. Finally, access to data

and models would not mean as much without the visualization tools included in DaViTpy. The development is version-controlled using git and github, providing the framework for clear history, contribution and feedback tracking.

The goal of this paper is to present the different aspects of DaViTpy and demonstrate the potential benefits of such projects for the space sciences. In the following sections, we provide details on the data access (Section C.2), model integration (Section C.3) and visualization tools (Section C.4) included in DaViTpy. For each one of these three aspects, we demonstrate use cases and discuss the potential benefits and caveats of our approach. Finally, we provide an overview of the development approach (Section C.5), a key component of DaViTpy and its potential future.

C.2 Data Integration

Obtaining data is one of the first steps in doing science. Often, just obtaining the data is a problem. Sometimes one must email a PI, specifically ask for a time period, and then wait for it to be delivered. Other times, the data is hosted on a remote FTP server, often with no documentation. Although in this paradigm access is easy, the scientist must decipher what the file actually contains. Yet another paradigm which exists is requesting data through a web form. This can be easy to use, and well documented, but there are often limits on the amount of data which can be requested at once doing this. This means that the form often has to be submitted several times, which is a nuisance. In all of these cases even after getting the data, the scientist must then write routines to read the data, which is tedious and time-consuming, especially since there is not a consistent file format across space science.

DaViTPy represents a paradigm shift in the way in which data is obtained. Instead of going and looking for data somewhere, the user simply executes a command, the the data is downloaded and read into coherent, useable objects in the environment. Take, for example, reading a period of Dst data:

```
gme.ind.dst.readDst(datetime(2011,1,1,0,0),eTime=datetime(2011,1,2,0,0))
Out[1]:
[Dst record FROM: 2011-01-01 00:00:00
info = These data were downloaded from WDC For Geomagnetism, Kyoto.
*Please be courteous and give credit to data providers
when credit is due.*
dst = -11.0
time = 2011-01-01 00:00:00
dataSet = Dst
, ...
 Dst record FROM: 2011-01-02 00:00:00
info = These data were downloaded from WDC For Geomagnetism, Kyoto.
*Please be courteous and give credit to data providers
when credit is due.*
dst = -1.0
time = 2011-01-02 00:00:00
dataSet = Dst
]
```

Using a single read command, we have queried the server for a day of data, located the data, and read it into a list of Dst objects. All data access within DaViTPy is handled in this manner.

Additionally, several of the datasets available within DaViTPy are stored in a NoSQL database, allowing for query operations. For example, one can read all Omni data from January of 2011 with IMF Bz values between -100 and 0 and By values between 10 and 20 with a command like so:

```
omniList = gme.ind.readOmni(sTime=datetime(2011,1,1,0,0),
                            eTime=datetime(2011,2,1,0,0),
                            bz=[-100,0],bye=[10,20])
```

Currently, the datasets which are available from the NoSQL database are SYM/ASY,

AU/AL/AO/AE, Kp, OMNI, Dst, and POES. Additionally, SuperDARN data is available, but this data is hosted on an FTP server. Note that even though the data is hosten on an FTP server, the downloading, reading, and parsing of data into objects is still done in the backend, and is no harder than reading data from the NoSQL database.

In the future, we plan to make more datasets available within DaViTPy. The beauty of the design is that data does not have to be moved to a central location, routines simply have to be written to automatically fetch the data from wherever it resides and parse it. Once those routines are incorporated into DaViTPy, any user has access to it.

C.3 Model Integration

Most space science data is eventually compared to or assimilated into numerical models, whether to directly simulate the environment [e.g., *Bilitza et al.*, 2011b], or as support to study other physical processes such as neutral or plasma waves. However, to the authors knowledge, there is no software package which enables easy interfacing between data and models.

For this reason, DaViTpy includes several key models such as the International Reference Ionosphere (IRI), International Geomagnetic Reference Field (IGRF), Horizontal Wind Model (HWM07), Tsyganenko (T96), and more. The common approach for each model is to leave the original code almost untouched, and design a Python wrapper for each using either F2PY [*Peterson*, 2009] for FORTRAN-based models or the Python/C API for C/C++-based models.

This provides a single and convenient environment for data and model exploration. One could read and plot an electron density profile from the Millstone Hill Incoherent Scatter Radar, and in the next line, query IRI for the same profile. In the following code, we illustrate another example, running the Tsyganenko model to obtain conjugate locations.

```
lats = range(10, 80, 10) # latitudes: 10, 20, 30, 40, 50, 60, 70
```

```
lons = zeros(len(lats)) # longitude: 0
rhos = 6672.*ones(len(lats)) # 300 km altitude
# trace field lines and find conjugate points
trace = tsyganenko.tsygTrace(lats, lons, rhos)
print trace # print results
ax = trace.plot() # plot traced field lines
```

In the case of the Tsyganenko model illustrated in the above code, we are working on integrating more recent versions of the model, but the interface will remain the same, providing a high level of abstraction, while preserving the possibility to dive down to the low-level FORTRAN subroutines, while remaining in the Python environment. It is worth highlighting that this model integration approach comes at no additional cost to the model developers while bringing great benefits to the model users.

C.4 Visualization

Data visualization is often a critical part of scientific analysis. Because of this, we have incorporated it into DaViTPy, heavily utilizing the python library Matplotlib [*Hunter*, 2007]. Our goal when developing the visualization routines was to keep it as simple as possible while simultaneously remaining incredibly flexible. We achieve this goal by modularizing all of the routines. Consider, for example, the plot shown in Figure C.1. This figure shows data from two SuperDARN radars, as well as POES total energy detector data overlaid [*Rodger et al.*, 2010]. This plot is generated with a single command:

```
pydarn.plotting.fan.plotFan(datetime(2012,5,13,8,0),['bks','fhw'],
                            overlayPoes=True)
```

Several routines are utilized in the creation Figure C.1, hidden behind the above simple code. First, a single routine is called in order to draw the map. Another routine is then called to overlay the SuperDARN data. A third routine is called to overlay the POES satellite data.

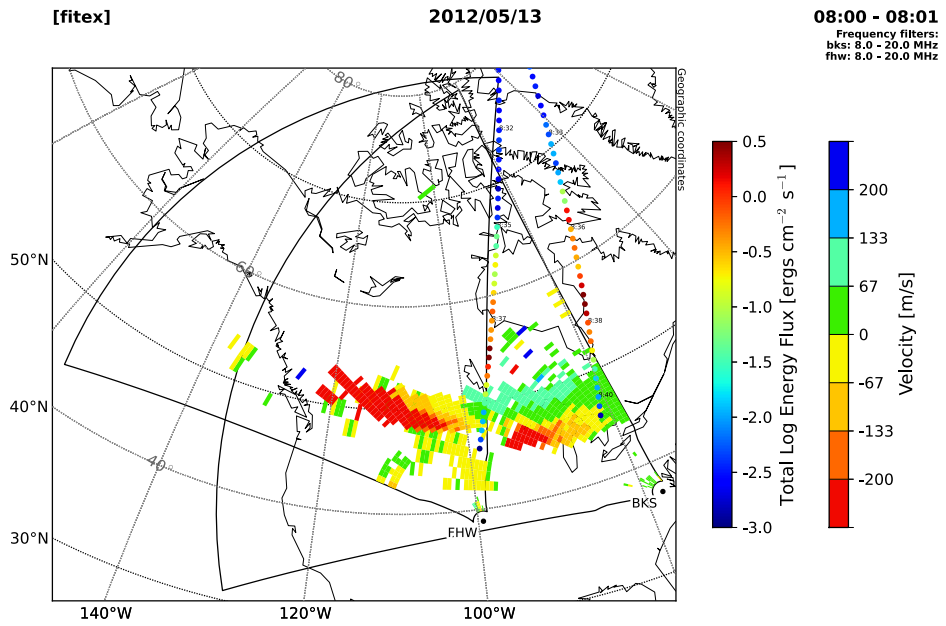

Figure C.1. An example of a plot generated using DaViTPy. The colored rectangles show SuperDARN Doppler velocity, and the colored circles are POES TED measurements.

There are several advantages to this type of design. First, a fairly generic, but nevertheless robust, plot can be generated with a single command. Second, it provides a framework for the incorporation of new datasets. For example, if a new satellite dataset were to be incorporated, an overlay routine could be written, and this routine could just be woven into the overarching single plot command. Third, it allows for a lot of flexibility when one is developing figures for publication. When preparing these types of figures, the ability to fully customize plots is often desirable. In the DaViTPy paradigm, the scientist would have this ability because instead of calling a single, overarching routine with options, they could call the background routines one by one in order to pick and choose what gets plotted and how.

Another example of SuperDARN data visualization is shown in Figure C.2. This is a SuperDARN Range-Time Intensity (RTI) plot, which shows Doppler velocity in the top colored panel, backscatter power in the middle panel, and spectral width

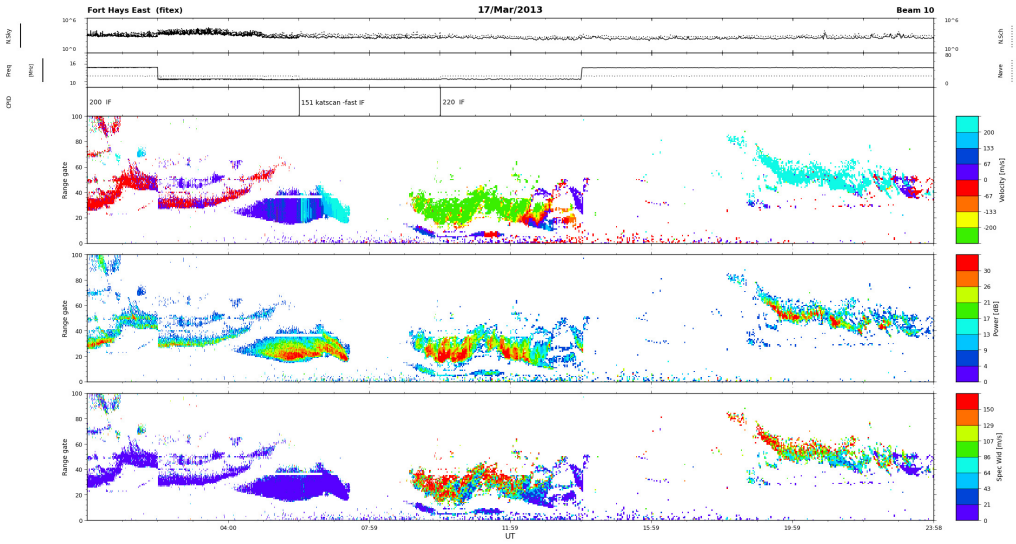

Figure C.2. An example of a SuperDARN RTI plot generated using DaViTPy. The top colored panel shows Doppler velocity, the middle panel shows backscatter power, and the bottom panel shows spectral width.

in the bottom panel. This again was generated using a single command, which makes use of several plotting subroutines. there are a few other types of plots which can be generated using DaViTPy, but we will not show examples of all of them. In general, if a type of plot can be done very simply using the routines in matplotlib, we have not implemented separate routines for plotting. In the future, we would like to be able to include and visualize more datasets alongside whose which are already present.

C.5 Development approach

The most essential aspect of DaViTpy's development is that it is developed by space scientists for the space science community. Every component is the product of conscientious development, peer testing and thorough documentation. It is to remain free and open-source at all times, with clear acknowledgement of all its contributors.

To enable these requirements, we rely on well-tested software engineering prac-

tices. Git and GitHub[1] are used to facilitate the distributed version control, contribution tracking and management (*a.k.a.*, pull requests), and bug reporting. The documentation is auto-generated directly from inline code docstrings, then hosted online [2]. Any new contribution to the codebase is evaluated based on its technical details as much as its documentation.

This workflow is in no way innovative, it has worked successfully for many other projects. Bug reports and pull requests are handled by the most qualified and available contributors for each specific request. This removes the need for a single code guru stretching his time and knowledge to their thinnest, thus increasing development pace and quality.

C.6 Conclusions

We have presented the first community developed space science software package, and described its mail functionalities, which include:

- data access: SYM/ASY, AU/AL/AO/AE, Kp, OMNI, Dst, POES and SuperDARN
- model access: IGRF, IRI, MSIS, HWM, T96 and AACGM
- visualization: each data source, model and coordinate system includes an associated set of plotting tools

While DaViTpy provides all these very useful tools, its most important strength relies on its development model. DaViTpy has relied on an international collaboration to develop and test these tools. Future plans are currently being discussed to involve other institutional software packages in this community driven development effort.

We invite members of the community to join the effort by adopting the DaViTpy package for their own projects, reporting any issues, and whenever possible, developing new functionality.

[1] http://github.com
[2] http://davit.ece.vt.edu/davitpy/

References

André, D., G. J. Sofko, K. Baker, and J. MacDougall (1998), SuperDARN interferometry: Meteor echoes and electron densities from groundscatter, *J. Geophys. Res.*, *103*(A4), 7003–7015.

Baker, J. B. H., R. A. Greenwald, J. M. Ruohoniemi, K. Oksavik, J. W. Gjerloev, L. J. Paxton, and M. R. Hairston (2007), Observations of ionospheric convection from the Wallops SuperDARN radar at middle latitudes, *J. Geophys. Res.*, *112*(A1).

Baker, K., and S. Wing (1989), A new magnetic coordinate system for conjugate studies at high latitudes, *J. Geophys. Res.*, *94*(A7), 9139–9143, doi:10.1029/JA094iA07p09139.

Baker, K., R. Greenwald, A. Walker, P. Bythrow, L. Zanetti, T. Potemra, D. Hardy, F. Rich, and C. Rino (1986), A case study of plasma processes in the dayside cleft, *J. Geophys. Res.*, *91*(A3), 3130–3144.

Bates, H. F. (1971), The aspect sensitivity of spread-F irregularities, *J. Atmos. Sol.-Terr. Phys.*, *33*(1), 111–115.

Bates, H. F., and P. R. Albee (1969), Aspect sensitivity of HF auroral echoes, *J. Geophys. Res.*, *74*(5), 1164–1168.

Bates, H. F., and P. R. Albee (1970), Aspect sensitivity of F-layer HF backscatter echoes, *J. Geophys. Res.*, *75*(1), 165–170.

Bellaire, P. (2006), Community Coordinated Modeling Center 2005 Workshop Report, *Space Weather*, *4*(2), doi:10.1029/2005SW000206.

Bilitza, D. (2001), International Reference Ionosphere 2000, *Radio Sci.*, *36*(2), 261–275.

Bilitza, D., and B. Reinisch (2008), International Reference Ionosphere 2007: Improvements and new parameters, *J. Adv. Space Res.*, *42*(4), 599–609.

Bilitza, D., L. McKinnell, B. Reinisch, and T. Fuller-Rowell (2011a), The international reference ionosphere today and in the future, *Journal of Geodesy*, *85*(12), 909–920.

Bilitza, D., L.-A. McKinnell, B. Reinisch, and T. Fuller-Rowell (2011b), The international reference ionosphere today and in the future, *Journal of Geodesy*, *85*(12), 909–920, doi: 10.1007/s00190-010-0427-x.

Blanchard, G. T., S. Sundeen, and K. B. Baker (2009), Probabilistic identification of high-frequency radar backscatter from the ground and ionosphere based on spectral characteristics, *Radio Sci.*, *44*, doi:{10.1029/2009RS004141}.

Breit, G., and M. A. Tuve (1926), A test of the existence of the conducting layer, *Physical Review*, *28*, 554–575.

Bristow, W. A., R. A. Greenwald, and J. P. Villain (1996), On the seasonal dependence of medium-scale atmospheric gravity waves in the upper atmosphere at high latitudes, *J. Geophys. Res.*, *101*(A7), 15,685–15,699.

Budden, K. G. (1966), *Radio waves in the ionosphere*, Cambridge [Eng.] University Press.

Buonsanto, M. J., and O. G. Witasse (1999), An updated climatology of thermospheric neutral winds and *F region ion drifts above Millstone Hill*, *J. Geophys. Res.*, *104*, 24,675–24,687.

Burns, A. G., S. C. Solomon, W. Wang, G. Jee, C. H. Lin, C. Rocken, and Y. H. Kuo (2011), The summer evening anomaly and conjugate effects, *J. Geophys. Res.*, *116*.

Chen, F. F. (1984), *Introduction to plasma physics and controlled fusion*, vol. 1, 2nd ed., Elsevier, New York.

Chisham, G., T. Yeoman, and G. Sofko (2008), Mapping ionospheric backscatter measured by the SuperDARN HF radars–Part 1: A new empirical virtual height model, *Ann. Geophys.*, *26*, 823–841.

Chisham, G., M. Lester, S. E. Milan, M. P. Freeman, W. A. Bristow, A. Grocott, K. A. McWilliams, J. M. Ruohoniemi, T. K. Yeoman, P. L. Dyson, R. A. Greenwald, T. Kikuchi, M. Pinnock, J. P. S. Rash, N. Sato, G. J. Sofko, J.-P. Villain, and A. D. M. Walker (2007), A decade of the Super Dual Auroral Radar Network (SuperDARN): scientific achievements, new techniques and future directions, *Surv. Geophys.*, *28*, 33–109.

Clausen, L. B. N., J. B. H. Baker, J. M. Ruohoniemi, R. A. Greenwald, E. G. Thomas, S. G. Shepherd, E. R. Talaat, W. A. Bristow, Y. Zheng, A. J. Coster, and S. Sazykin (2012), Large-scale observations of a subauroral polarization stream by midlatitude SuperDARN radars: Instantaneous longitudinal velocity variations, *J. Geophys. Res.*, *117*.

Coleman, C. J. (1998), A ray-tracing formulation and its application to some problems in over-the-horizon radar, *Radio Sci.*, *33*(4), 1187–1197.

Davies, K. (1990), *Ionospheric Radio*, The Institution of Engineering and Technology, London, U.K.

de Larquier, S., P. Ponomarenko, A. J. Ribeiro, J. M. Ruohoniemi, J. B. H. Baker, K. T. Sterne, and M. Lester (2013a), On the spatial distribution of decameter-scale sub-auroral ionospheric irregularities observed by SuperDARN radars, *J. Geophys. Res.*, *118*, doi:10.1002/jgra.50475.

de Larquier, S., A. Eltrass, A. Mahmoudian, J. M. Ruohoniemi, J. B. H. Baker, W. A. Scales, P. J. Erickson, and R. A. Greenwald (2013b), Investigation of the Temperature Gradient Instability as the Source of Mid-Latitude Quiet-Time Decameter-Scale Ionospheric Irregularities: Part 1, Observations, submitted to J. Geophys. Res.

de Larquier, S., J. M. Ruohoniemi, J. B. H. Baker, N. R. Varrier, and M. Lester (2011), First observations of the midlatitude evening anomaly using Super Dual Auroral Radar Network (SuperDARN) radars, *J. Geophys. Res.*, *116*.

Drob, D. P., J. T. Emmert, G. Crowley, J. M. Picone, G. G. Shepherd, W. Skinner, P. Hays, R. J. Niciejewski, M. Larsen, C. Y. She, J. W. Meriwether, G. Hernandez, M. J. Jarvis, D. P. Sipler, C. A. Tepley, M. S. O'Brien, J. R. Bowman, Q. Wu, Y. Murayama, S. Kawamura, I. M. Reid, and R. A. Vincent (2008), An empirical model of the Earth's horizontal wind fields: HWM07, *J. Geophys. Res.*, *113*(A12).

Dyson, P. L., R. J. Norman, M. L. Parkinson, et al. (2002), Ionospheric propagation modes identified using the TIGER HF radar, in *Proceedings of the Workshop on the Applications of Radio Science*.

Eccles, D., and J. D. Burge (1973), The behaviour of the upper ionosphere over North America at sunset, *J. Atmos. Sol.-Terr. Phys.*, *35*, 1927–1934.

Eltrass, A., A. Mahmoudian, W. A. Scales, S. de Larquier, J. M. Ruohoniemi, J. B. H. Baker, R. A. Greenwald, and P. J. Erickson (2013), Investigation of the Temperature Gradient Instability as the Source of Mid-Latitude Quiet-Time Decameter-Scale Ionospheric Irregularities: Part 2, Linear Analysis, submitted to J. Geophys. Res.

Evans, J. V. (1965), Cause of the mid-latitude evening increase in f_0F_2, *J. Geophys. Res.*, *70*, 1175–1185.

Evans, J. V. (1965b), Cause of the Midlatitude Winter Night Increase in f_0F_2, *J. Geophys. Res.*, *70*, 4331–4345.

Farley, D. T. (1959), A Theory of Electrostatic Fields in a Horizontally Stratified Ionosphere Subject to a Vertical Magnetic Field, *J. Geophys. Res.*, *64*(9), 1225–1233.

Fejer, B., and M. C. Kelley (1980), Ionospheric irregularities, *Reviews of Geophysics*, *18*(2), 401–454.

Foster, J., D. Tetenbaum, C. Del Pozo, J.-P. St-Maurice, and D. Moorcroft (1992), Aspect angle variations in intensity, phase velocity, and altitude for high-latitude 34-cm E region irregularities, *J. Geophys. Res.*, *97*(A6), 8601–8617.

Fremouw, E., C. Rino, R. Livingston, and M. Cousins (1977), A persistent subauroral scintillation enhancement observed in Alaska, *Geophys. Res. Lett.*, *4*(11), 539–542.

Frissell, N. A., J. B. H. Baker, J. M. Ruohoniemi, L. B. N. Clausen, Z. C. Kale, I. J. Rae, L. Kepko, K. Oksavik, R. A. Greenwald, and M. L. West (2011), First radar observations in the vicinity of the plasmapause of pulsed ionospheric flows generated by bursty bulk flows, *Geophysical Research Letters*, *38*(1), doi:10.1029/2010GL045857.

Fukao, S., and M. C. Kelley (1991), Turbulent upwelling of the mid-latitude ionosphere: 1. Observational results by the MU radar, *J. Geophys. Res.*, *96*(A3), 3725–3746.

Gillies, R., G. Hussey, G. Sofko, K. McWilliams, R. Fiori, P. Ponomarenko, and J.-P. S. Maurice (2009), Improvement of SuperDARN velocity measurements by estimating the index of refraction in the scattering region using interferometry, *J. Geophys. Res.*, *114*(A7), A07,305.

Greenwald, R., K. Baker, J. Dudeney, M. Pinnock, T. Jones, E. Thomas, J.-P. Villain, J.-C. Cerisier, C. Senior, C. Hanuise, et al. (1995), DARN/SuperDARN, *Space Science Reviews*, *71*(1), 761–796.

Greenwald, R. A., K. Oksavik, P. J. Erickson, F. D. Lind, J. M. Ruohoniemi, J. B. H. Baker, and J. W. Gjerloev (2006), Identification of the temperature gradient instability as the source of decameter-scale ionospheric irregularities on plasmapause field lines, *Geophys. Res. Lett.*, *33*, L18105.

Greenwald, R. A., K. B. Baker, R. A. Hutchins, and C. Hanuise (1985), An HF phased-array radar for studying small-scale structure in the high-latitude ionosphere, *Radio Sci.*, *20*(1), 63–79.

Grocott, A., S. Milan, J. Baker, M. Freeman, M. Lester, and T. Yeoman (2011), Dynamic subauroral ionospheric electric fields observed by the Falkland Islands radar during the course of a geomagnetic storm, *J. Geophys. Res.*, *116*(A11), A11,202.

Gropp, W., E. Lusk, and A. Skjellum (1999), *Using MPI : Portable parallel programming with the Message-Passing Interface*, MIT Press.

Hall, G. E., J. W. MacDougall, J. F. Cecile, D. R. Moorcroft, and J. P. St-Maurice (1999), Finding gravity wave source positions using the Super Dual Auroral Radar Network, *J. Geophys. Res.*, *104*(A1), 67–78.

Hanisch, R. J., and G. H. Jacoby (2001), Astronomical Data Analysis Software and Systems X, *Publications of the Astronomical Society of the Pacific*, *113*(784), 772–773, doi:10.1086/320803.

Hedin, A. E., E. L. Fleming, A. H. Manson, F. J. Schmidlin, S. K. Avery, R. R. Clark, S. J. Franke, G. J. Fraser, T. Tsuda, F. Vial, and R. A. Vincent (1996), Empirical wind model for the upper, middle and lower atmosphere, *J. Atmos. Sol.-Terr. Phys.*, *58(13)*, 1421–144.

Heelis, R. (2004), Electrodynamics in the low and middle latitude ionosphere: A tutorial, *J. Atmos. Sol.-Terr. Phys.*, *66*(10), 825–838.

Heelis, R., J. Vickrey, and N. Walker (1985), Electrical coupling effects on the temporal evolution of F layer plasma structure, *J. Geophys. Res.*, *90*(A1), 437–445.

Holt, J. M., S.-R. Zhang, and M. J. Buonsanto (2002), Regional and local ionospheric models based on millstone hill incoherent scatter radar data, *Geophys. Res. Lett.*, *29*(8), 48–1.

Hosokawa, K., T. Iyemori, A. Yukimatu, and N. Sato (2000), Spatial distribution of irregularity occurrence rate in the subauroral F-region as observed by the SuperDARN radars, in *Proc. SuperDARN 2000 Workshop, Beechworth, Australia*.

Hosokawa, K., T. Iyemori, A. S. Yukimatu, and N. Sato (2001), Source of field-aligned irregularities in the subauroral F region as observed by the SuperDARN radars, *J. Geophys. Res.*, *106*(A11), 24,713–24.

Hosokawa, K., M. Sugino, M. Lester, N. Sato, A. Yukimatu, and T. Iyemori (2002), Simultaneous measurement of duskside subauroral irregularities from the CUTLASS Finland radar and EISCAT UHF system, *J. Geophys. Res.*, *107*(A12), 1457.

Huba, J., G. Joyce, and J. Fedder (2000), Sami2 is Another Model of the Ionosphere (SAMI2): A new low-latitude ionosphere model, *J. Geophys. Res.*, *105*(A10), 23,035–23,053.

Huba, J., G. Joyce, S. Sazykin, R. Wolf, and R. Spiro (2005), Simulation study of penetration electric field effects on the low-to mid-latitude ionosphere, *Geophys. Res. Lett.*, *32*(23), L23,101.

Hudson, M. K., and M. C. Kelley (1976), The Temperature Gradient Drift Instability at the Equatorward Edge of the Ionospheric Plasma Trough, *J. Geophys. Res.*, *81(22)*, 3813–3918.

Hughes, J. M., W. A. Bristow, R. A. Greenwald, and R. J. Barnes (2002), Determining characteristics of HF communications links using SuperDARN, *Ann. Geophys.*, *20*(7), 1023–1030.

Hunter, J. D. (2007), Matplotlib: A 2D graphics environment, *Computing In Science & Engineering*, *9*(3), 90–95.

Hysell, D., M. Kelley, Y. M. Yampolski, V. Beley, A. Koloskov, P. Ponomarenko, and O. Tyrnov (1996), HF radar observations of decaying artificial field-aligned irregularities, *J. Geophys. Res.*, *101*(A12), 26,981–26.

Jones, E., T. Oliphant, P. Peterson, et al. (2001), SciPy: Open source scientific tools for Python.

Jones, R. M., and J. J. Stephenson (1975), A versatile three-dimensional ray tracing computer program for radio waves in the ionosphere, *OT report 75-76.PB2488567*.

Kane, T. A., R. A. Makarevich, and J. C. Devlin (2012), HF radar observations of ionospheric backscatter during geomagnetically quiet periods, *Ann. Geophys.*, *30*(1), 221–233, doi:{10.5194/angeo-30-221-2012}.

Kelley, M., B. Fejer, and C. Gonzales (1979), An explanation for anomalous equatorial ionospheric electric fields associated with a northward turning of the interplanetary magnetic field, *Geophys. Res. Lett.*, *6*(4), 301–304.

Kelley, M. C. (2009), *The Earth's ionosphere, plasma physics and electrodynamics*, International Geophysics Series, 2nd ed., Elsevier.

Kelley, M. C., and S. Fukao (1991), Turbulent upwelling of the mid-latitude ionosphere: 2. Theoretical framework, *J. Geophys. Res.*, *96*(A3), 3747–3753.

Kunduri, B., J. Baker, J. Ruohoniemi, L. Clausen, A. Grocott, E. Thomas, M. Freeman, and E. Talaat (2012), An examination of inter-hemispheric conjugacy in a subauroral polarization stream, *J. Geophys. Res.*, *117*(A8), A08,225.

Lei, J., L. Liu, W. Wan, , and S.-R. Zhang (2005), Variations of electron density based on long-term incoherent scatter radar and ionosonde measurements over Millstone Hill, *Radio Sci.*, *40*, RS2008.

Lin, C. H., C. H. Liu, J. Y. Liu, C. H. Chen, A. G. Burns, and W. Wang (2010), Mid-latitude summer nighttime anomaly of the ionospheric electron density observed by FORMOSAT3/COSMIC, *J. Geophys. Res.*, *115*, A03308.

Liu, E., H. Hu, R. Liu, Z. Wu, and M. Lester (2012), An adjusted location model for SuperDARN backscatter echoes, *Ann. Geophys.*, *30*(12), 1769.

Liu, H., S. V. Thampi, and M. Yamamoto (2010), Phase reversal of the diurnal cycle in the midlatitude ionosphere, *J. Geophys. Res.*, *115*.

McDonald, A., J. Whittington, S. de Larquier, E. Custovic, T. Kane, and J. Devlin (2013), Elevation Angle-of-Arrival Determination for a Standard and a Modified SuperDARN HF Radar Layout, *Radio Sci.*, doi:10.1002/2013RS005157.

Milan, S., T. Jones, T. Robinson, E. Thomas, and T. Yeoman (1997b), Interferometric evidence for the observation of ground backscatter originating behind the CUTLASS coherent HF radars, in *Ann. geophys.*, vol. 15, pp. 29–39, Springer.

Milan, S. E., T. K. Yeoman, M. Lester, E. C. Thomas, and T. B. Jones (1997a), Initial backscatter occurrence statistics from the CUTLASS HF radars, *Ann. Geophys.*, *15*, 703–718.

Milan, S. E., A. Grocott, S. de Larquier, M. Lester, T. K. Yeoman, M. P. Freeman, and G. Chisham (2013), Perturbations of the Weddell Sea ionospheric anomaly associated with geomagnetic activity, *J. Geophys. Res.*, *118*, 6608–6617, doi:http://dx.doi.org/10.1002/jgra.50566.

National Academy of Sciences (2013), Solar and Space Physics: A Science for a Technological Society, 2013-2022 Decadal Survey.

Nishitani, N., and T. Ogawa (2005), Model calculations of possible ionospheric backscatter echo area for a mid-latitude HF radar, *Adv. Polar Upper Atmos. Res.*, *19*, 55–62.

Norman, R., and P. Dyson (2006), HF radar backscatter inversion technique, *Radio Sci.*, *41*(4), RS4010.

Oksavik, K., R. Greenwald, J. Ruohoniemi, M. Hairston, L. Paxton, J. Baker, J. Gjerloev, and R. Barnes (2006), First observations of the temporal/spatial variation of the sub-auroral polarization stream from the SuperDARN Wallops HF radar, *Geophys. Res. Lett.*, *33*, L12,104.

Oksman, J., H. Möller, and R. Greenwald (1979), Comparisons between strong HF backscatter and VHF radar aurora, *Radio Science*, *14*(6), 1121–1133.

Oliphant, T. E. (2006), *Guide to NumPy*, Provo, UT.

Ott, E., and D. Farley (1974), The k spectrum of ionospheric irregularities, *J. Geophys. Res.*, *79*(16), 2469–2472.

Oyeyemi, E., and L. McKinnell (2008), A new global {F2} peak electron density model for the International Reference Ionosphere (IRI), *Advances in Space Research*, *42*(4), 645 – 658, doi:10.1016/j.asr.2007.10.031.

Pacheco, P. (1996), *Parallel Programming with MPI*, Morgan Kaufmann.

Parkinson, M., J. Devlin, P. L. Dyson, M. Pinnock, H. Ye, R. Morris, and C. Waters (2002), Diurnal, seasonal, and geomagnetic activity variations in the occurrence of decametre-scale irregularities in the auroral and subauroral ionosphere, in *Proceedings of the Workshop on the Applications of Radio Science, Refereed Paper G*, vol. 9.

Parkinson, M., J. Devlin, H. Ye, C. Waters, P. Dyson, A. Breed, R. Morris, et al. (2003), On the occurrence and motion of decametre-scale irregularities in the sub-auroral, auroral, and polar cap ionosphere, in *Ann. Geophys.*, vol. 21, pp. 1847–1868.

Peterson, P. (2009), F2PY: a tool for connecting Fortran and Python programs, *International Journal of Computational Science and Engineering*, *4*(4), 296, doi:10.1504/IJCSE.2009.029165.

Ponomarenko, P., A. Koustov, J.-P. S. Maurice, and J. Wiid (2011), Monitoring the F-region peak electron density using HF backscatter interferometry, *Geophys. Res. Lett.*, *38*(21), L21,102.

Ponomarenko, P., F. Menk, C. Waters, and M. Sciffer (2005), Pc3-4 ULF waves observed by the SuperDARN TIGER radar, *Ann. Geophys.*, *23*(4), 1271–1280.

Ponomarenko, P. V., J.-P. St-Maurice, C. L. Waters, R. G. Gillies, and A. V. Koustov (2009), Refractive index effects on the scatter volume location and Doppler velocity estimates of ionospheric HF backscatter echoes, *Ann. Geophys.*, *27*, 4207–4219.

Ponomarenko, P. V., J. P. S. Maurice, G. C. Hussey, and A. V. Koustov (2010), HF ground scatter from the polar cap: Ionospheric propagation and ground surface effects, *J. Geophys. Res.*, *115*.

Potter, D. (1973), *Computational Physics*, Wiley.

Press, W. H., S. A. Teukolsky, W. T. Vetterling, and B. P. Flannery (2002), *Numerical Recipes in C: the art of scientific computing*, 2nd ed., Cambridge University Press, New York.

Ravindran-Varrier, N. (2010), Ray Tracing analysis for the mid-latitude SuperDARN HF radar at Blackstone incorporating the IRI-2007 model, Master's thesis, Virginia Tech, Blackbsurg, Virginia, USA.

Ribeiro, A., J. Ruohoniemi, P. Ponomarenko, L. Clausen, J. Baker, R. Greenwald, K. Oksavik, and S. Larquier (2013a), A comparison of SuperDARN ACF fitting methods, *Radio Sci.*, *48*, 274–282, doi:10.1002/rds.20031.

Ribeiro, A., P. Ponomarenko, J. Ruohoniemi, J. Baker, L. Clausen, R. Greenwald, and S. Larquier (2013b), A realistic radar data simulator for the Super Dual Auroral Radar Network, *Radio Sci.*, *48*, 283–288, doi:10.1002/rds.20032.

Ribeiro, A. J., J. M. Ruohoniemi, J. B. H. Baker, L. B. N. Clausen, and S. de Larquier (2011), A new approach for identifying ionospheric backscatter in mid-latitude SuperDARN data, *Radio Sci.*, *46*, RS4011, doi:10.1029/2011RS004676.

Ribeiro, A. J., J. M. Ruohoniemi, J. B. H. Baker, L. B. N. Clausen, R. A. Greenwald, and M. Lester (2012), A survey of plasma irregularities as seen by the mid-latitude Blackstone SuperDARN radar, *J. Geophys. Res.*, *117*, A02311.

Rishbeth, H. (1997), The ionospheric E-layer and F-layer dynamos—a tutorial review, *J. Atmos. Sol.-Terr. Phys.*, *59*(15), 1873–1880.

Rishbeth, H., and O. K. Garriott (1969), *Introduction to ionospheric physics*, International Geophysics Series, Academic Press.

Robitaille, T. P., E. J. Tollerud, P. Greenfield, M. Droettboom, E. Bray, T. Aldcroft, M. Davis, A. Ginsburg, A. M. Price-Whelan, W. E. Kerzendorf, and et al. (2013), Astropy: A community Python package for astronomy, *Astronomy & Astrophysics*, *558*, A33, doi:10.1051/0004-6361/201322068.

Rodger, C. J., M. A. Clilverd, J. C. Green, and M. M. Lam (2010), Use of POES SEM-2 observations to examine radiation belt dynamics and energetic electron precipitation into the atmosphere, *Journal of Geophysical Research*, *115*(A4), A04,202, doi:10.1029/2008JA014023.

Ruohoniemi, J. M., and K. B. Baker (1998), Large-scale imaging of high-latitude convection with Super Dual Auroral Radar Network HF radar observations, *J. Geophys. Res.*, *103*(A9), 20,797–20,811.

Ruohoniemi, J. M., R. A. Greenwald, K. B. Baker, J.-P. Villain, C. Hanuise, and J. Kelly (1989), Mapping high-latitude plasma convection with coherent HF radars, *J. Geophys. Res.*, *94*(A10), 13,463–13.

Ruohoniemi, J. M., R. A. Greenwald, J. P. Villain, K. B. Baker, P. T. Newell, and C. Meng (1988), Coherent HF radar backscatter from small-scale irregularities in the dusk sector of the subauroral ionosphere, *J. Geophys. Res.*, *93*(A11), 12,871–12,882.

Ruohoniemi, J. M., R. J. Barnes, R. A. Greenwald, and S. G. Shepherd (2001), The response of the high-latitude ionosphere to the coronal mass ejection event of April 6, 2000: A practical demonstration of space weather nowcasting with the Super Dual Auroral Radar Network HF radars, *J. Geophys. Res.*, *106*(A12), 30,085–30,097.

Samson, J. C., R. A. Greenwald, J. M. Ruohoniemi, and K. B. Baker (1989), High-frequency radar observations of atmospheric gravity-waves in the high-latitude ionosphere, *Geophys. Res. Lett.*, *16*(8), 875–878.

Schunk, R., L. Scherliess, J. Sojka, D. Thompson, D. Anderson, M. Codrescu, C. Minter, T. Fuller-Rowell, R. Heelis, M. Hairston, et al. (2004), Global assimilation of ionospheric measurements (GAIM), *Radio Sci.*, *39*(1).

Schunk, R. W., and A. F. Nagy (2009), *Ionospheres: physics, plasma physics, and chemistry*, Atmospheric and Space Science Series, 2nd ed., Cambridge University Press.

Sterne, K., R. Greenwald, J. Baker, and J. Ruohoniemi (2011), Modeling of a twin terminated folded dipole antenna for the Super Dual Auroral Radar Network (SuperDARN), in *Radar Conference (RADAR), 2011 IEEE*, pp. 934–938, IEEE.

Su, S.-Y., C. Liu, H. Ho, and C. Chao (2006), Distribution characteristics of topside ionospheric density irregularities: Equatorial versus midlatitude regions, *J. Geophys. Res.*, *111*, A06305.

Taflove, A., and S. C. Hagness (2000), *Computational electrodynamics: the finite-difference time-domain method*, Artech House, second ed., Artech House, Boston, MA.

Thampi, S. V., C. Lin, H. Liu, and M. Yamamoto (2009), First tomographic observations of the Midlatitude Summer Nighttime Anomaly over Japan, *J. Geophys. Res.*, *114*, A10318.

Thomas, E., J. Baker, J. Ruohoniemi, L. Clausen, A. Coster, J. Foster, and P. Erickson (2013), Direct observations of the role of convection electric field in the formation of a polar tongue of ionization from storm enhanced density, *J. Geophys. Res.*, *118*, 1180–1189, doi:10.1002/jgra.50116.

Titheridge, J. E. (1995), Winds in the ionoosphere - a review, *J. Atmos. Sol.-Terr. Phys.*, *57*(14), 1681–1714.

Tsugawa, T., Y. Otsuka, A. Coster, and A. Saito (2007), Medium-scale traveling ionospheric disturbances detected with dense and wide TEC maps over North America, *Geophys. Res. Lett.*, *34*(22), L22,101.

Tsunoda, R. (1988), High-latitude F region irregularities: A review and synthesis, *Reviews of Geophysics*, *26*(4), 719–760.

Yeoman, T., G. Chisham, L. Baddeley, R. Dhillion, T. Karhunen, T. Robinson, A. Senior, and D. Wright (2008), Mapping ionospheric backscatter measured by the SuperDARN HF radars-part 2: Assessing SuperDARN virtual height models, *Ann. Geophys.*, *26*(4), 843–852.

Zhang, S.-R., and J. Holt (2007), Ionospheric climatology and variability from long-term and multiple incoherent scatter radar observations: Climatology in eastern American sector, *J. Geophys. Res.*, *112*(A6), A06,328.